

# A Study of The Spectral Signatures of Lithium Minerals of Fregeneda- Almendra Aplite- Pegmatite Field

João Pedro Campos da Silva

Mestrado em Geologia

Departamento de Geociências, Ambiente e Ordenamento do Território

2020

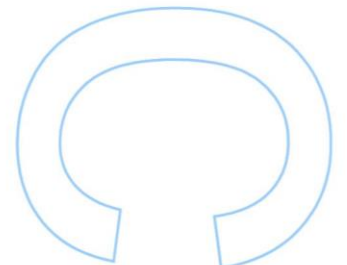
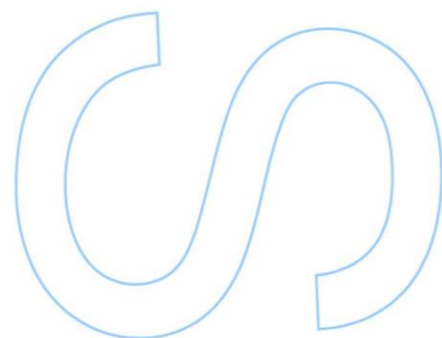
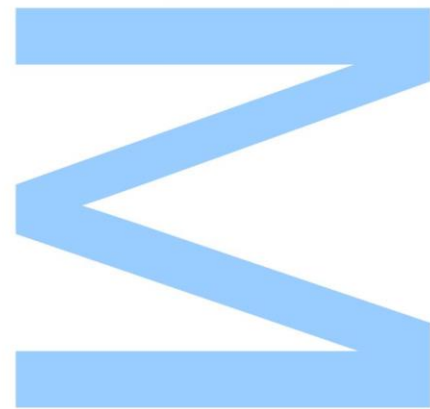
## **Orientador**

Ana Cláudia Moreira Teodoro, Professor Auxiliar, Faculdade de Ciências da Universidade do Porto

## **Coorientador**

Alexandre Martins Campos de Lima, Professor Auxiliar, Faculdade de Ciências da Universidade do Porto

Jean Cauzid, Professor Auxiliar, Faculté des Sciences et Technologies de Université de Lorraine



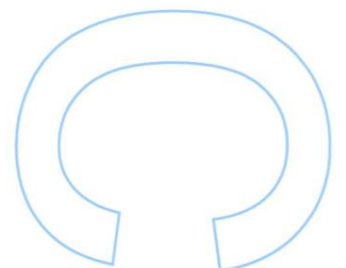
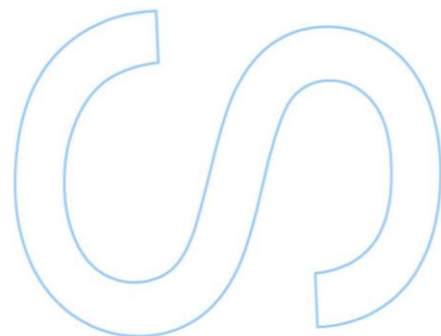
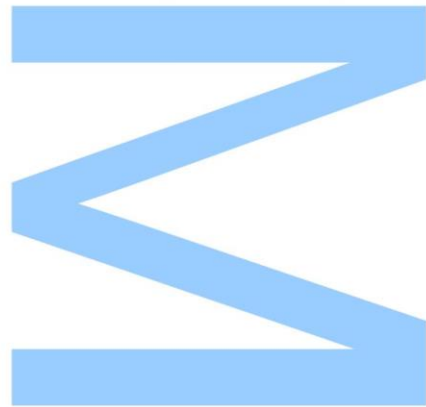




Todas as correções determinadas pelo júri, e só essas, foram efetuadas.

O Presidente do Júri,

Porto, \_\_\_\_/\_\_\_\_/\_\_\_\_





# Acknowledgments

I would like to thank Professor Doctor Ana Claudia Teodoro and Professor Doctor Alexandre Lima for the invitation to this project, and for all the guidance throughout the project.

My sincere thanks to Professor Doctor Jean Cauzid and Professor Doctor Antoine Petrelli, from Université de Lorraine, for so well having received me in the GeoRessources Laboratory and as well, for all the availability and guidance throughout my stay in Nancy, France.

I would like to thank Joana Fernandes for all the help with the sample selection, continuum removal of the spectra, and data analysis.

I would like to thank my friends and colleagues, Rafael Marques, Ricardo Lagoela, and Vânia Oliveira, for all the help and fruitful discussions.

And lastly, my most sincere thanks to my parents, for making this possible and for all effort, guidance, advises, support, and patience.



## Abstract

During the last decade, the demand for new environmentally friendly technologies and energies has led to an increase in the exploration of Lithium (Li). For that reason, remote sensing techniques have been used in the identification of new lithiumiferous deposits. With this, for easier identification of these deposits, arises the necessity for the search of greater knowledge of the spectral signatures of Li minerals.

Fregeneda (Spain)-Almendra (Portugal) aplite-pegmatite field is a region where several Li minerals occur (petalite, spodumene, lepidolite, zinnwaldite, and montebrasite) associated to four different types of Li enriched aplite-pegmatite veins. This region constitutes the study area, being integrated into the Central Iberian Zone, is characterized by the presence of autochthonous metasedimentary formations, of pre-Mesozoic, intruded by Variscan granites.

A total of 68 samples were studied, resulting in 399 measured spectra. All measurements were accomplished under a controlled lighting environment using a halogen bulb (4.25 V, 1.06 A). The SR-6500 (Spectral Evolution, Inc.) was the spectroradiometer used for this study. It is a device with a spectral range from 350 nm to 2500 nm (VIS-NIR-SWIR) of ultra-high-resolution. For the calibration of the equipment, a Spectralon (from Labsphere) was utilized.

The results obtained, demonstrate great similarities on the spectra of petalite and spodumene, presenting identical absorption features (~1412 nm, ~1910 nm, ~2206 nm). A more precise analysis showed that these absorption features are probably related to alteration minerals, such as montmorillonite and illite, where montmorillonite seems to be dominant. Lepidolite has also presented identical features to these minerals, however, the association with characteristic features of secondary Al-OH, allows different interpretations, placing them as diagnostic for white mica. These diagnostic features of white mica are as well present in the zinnwaldite spectral signature. The spectral signature of montebrasite, from 1300 nm to 2500 nm (SWIR), is characterized by an intense presence of absorption features.

The aplite-pegmatite veins, the Complexo Xisto-Grauváquico, and the granite lithologies have demonstrated the same main absorptions characteristic of the Li minerals studied, with absorption peaks at ~1412 nm, ~1910 nm, and ~2206 nm. However, the intense presence of iron oxides and Fe-OH bond features seems to be the principal differentiators of these lithologies.

**Keywords:** Lithium, Petalite, Spodumene, Lepidolite, Spectral Signature, Fregeneda-Almendra, Reflectance, Absorption.

## Resumo

No decorrer da última década, a procura por tecnologias e energias ambientalmente mais amigáveis, levou ao aumento da procura por Lítio (Li). Assim, técnicas de deteção remota têm vindo a ser aplicadas na identificação de novos depósitos litiníferos. Para uma identificação mais fácil destes depósitos, existe a necessidade de se obter um maior conhecimento sobre as assinaturas espectrais dos minerais de Li.

O campo aplito-pegmatítico de Fregeneda (Espanha)-Almendra (Portugal) é uma região onde se conhece a ocorrência de diversos minerais de Li (petalite, espodumena, lepidolite, zinnwaldite e montebrasite), associados a quatro diferentes tipos de filões aplito-pegmatíticos enriquecidos em Li. Esta região constitui a área de estudo deste trabalho, encontrando-se integrada na Zona Centro Ibérica e tendo como principais características a presença de formações metassedimentares autóctones, do pré-Mesozoico, intruídas por granitos Variscos.

Um total de 68 amostras foram estudadas, resultando em 399 espectros medidos. Todas estas medições foram realizadas em um ambiente de luz controlada, através de uma lâmpada de halogénio (4.25 V, 1.06 A). O SR-6500 (Spectral Evolution, Inc.) foi o espectrorradiómetro utilizado para o estudo, sendo este um aparelho com um alcance espectral dos 350 nm aos 2500 nm (VIS-NIR-SWIR) de alta resolução. Para a calibração do equipamento, um Spectralon (da Labsphere) foi utilizado.

Os resultados obtidos, demonstraram grandes similaridades nas assinaturas espectrais da petalite e da espodumena, apresentando feições de absorção idênticas (~1412 nm, ~1910 nm, ~2206 nm). Um estudo mais minucioso mostrou que estas feições de absorção estão provavelmente relacionadas com a presença de minerais de alteração, como a montmorilonite e a illite, onde a montmorilonite parece ser dominante. A lepidolite também apresentou feições idênticas a estes minerais, contudo, a associação a feições características de Al-OH secundário, permite diferentes interpretações, colocando-as como diagnósticas para micas brancas. Estas mesmas feições diagnósticas de micas brancas são visíveis na assinatura espectral da zinnwaldite. A assinatura espectral da montebrasite, dos 1300 nm aos 2500 nm (SWIR), é caracterizada pela intensa presença de feições de absorção.

As litologias do Complexo Xisto-Grauváquico, dos granitos e os filões aplito-pegmatíticos apresentaram as mesmas principais características de absorção dos minerais de Li estudados, com picos de absorção aos ~1412 nm, ~1910 nm e ~2206

nm. Assim, a intensa presença de feições relacionadas com óxidos de ferro e com a ligação Fe-OH, parecem ser os principais diferenciadores destas litologias.

**Palavras-Chave:** Lítio, Petalite, Espodumena, Lepidolite, Assinatura Espectral, Fregeneda-Almendra, Refletância, Absorção.

# Table of Contents

Acknowledgments.....	I
Abstract .....	III
Resumo .....	V
List of Tables .....	IX
List of Figures .....	XI
1. Introduction.....	1
1.1 Remote Sensing.....	2
1.2 Previous Works .....	4
2. Geographical and Geological Setting.....	7
2.1 Geographical Setting.....	7
2.2 Geological Setting .....	8
2.2.1 General Geology of The Pegmatite .....	13
2.2.2 Mineralogy .....	17
3. Sampling and Methodology.....	19
3.1 SR-6500 Spectroradiometer .....	23
3.1.1 Operating Mode .....	25
4. Results.....	27
4.1 Lithium Minerals .....	27
4.1.1 Petalite.....	27
4.1.2 Lepidolite .....	36
4.1.3 Spodumene .....	43
4.1.4 Zinnwaldite.....	52
4.1.5 Montebbrasite .....	58
4.2 Comparison Between Lithium Minerals .....	64
4.2.1 Petalite VS Spodumene.....	64
4.2.2 (Petalite and Spodumene) VS Lepidolite.....	65
4.2.3 Lepidolite VS Zinnwaldite.....	65

4.2.4 Montebrazite VS (Petalite, Spodumene, Lepidolite, and Zinnwaldite).....	66
4.3 Spectral Signatures of the Host Lithologies .....	72
4.3.1 T7 Aplite-Pegmatite and T5 Aplite-Pegmatite.....	72
4.3.2 Complexo Xisto-Grauváquico.....	75
4.3.3 Granite.....	79
4.4 Comparison with Spectral Libraries .....	82
4.4.1 USGS Spectral Library.....	82
4.4.2 ECOSTRESS Spectral Library .....	87
4.4.3 Discussion .....	92
4.4.4 CPRM Spectral Library .....	93
5. Conclusions .....	95
5.1 Further Work .....	97
6. References .....	99

## List of Tables

Table 1 - Description of the samples collected during the field trip, of 6 <sup>th</sup> and 7 <sup>th</sup> of February 2020, to the Fregeneda-Almendra aplite-pegmatite field.....	20
Table 2 - Description of the studied samples, made available by the Department of Geosciences, Environment and Spatial Planning, Faculty of Sciences, University of Porto.....	21
Table 3 – Identification of the measurement points used in the elaboration of the spectral signature of petalite. Description of the sampling location, vein type and measurement point.....	28
Table 4 - Identification of the measurement points, used in the elaboration of the spectral signature of lepidolite. Description of the sample and vein type to which measurement point belong. ....	36
Table 5 - Identification of the measurement points, used in the elaboration of the spectral signature of spodumene. Description of the sample location and vein type. Study of spodumene without quartz association. ....	43
Table 6 - Identification of the measurement points, used in the elaboration of the spectral signature of the SQUI structure (spodumene + quartz). Description of the sample location and vein type. ....	44
Table 7 - Identification of the measurement points, used in the elaboration of the spectral signature of zinnwaldite. ....	53



## List of Figures

- Figure 1 - Location of the study area. The study area represented is coincident with the geographical expression of the aplite-pegmatite field of Fregeneda-Almendra. Image source: Google Earth (Google Earth Pro, 2020)..... 7
- Figure 2 - Synthesis of the geotectonic zones present in the Iberian Massif (adapted from Gourvennec et al., 2010; Julivert et al., 1974; Dallmeyer & Garcia, 1990; Farias et al., 1987). Location of the study area in the geotectonic zones. Legend: CZ - Cantabrian Zone; WALZ - West Asturian-Leonese Zone; GTMZ - Galica Trás-os Montes Zone; CIZ - Central Iberian Zone; OMZ - Ossa-Morena Zone; SPZ - Sul-Portuguesa Zone. .... 9
- Figure 3 - Simplified geological map of the Fregeneda-Almendra aplite-pegmatitic field (Viera, 2010). Vein types : intra-granitic - T1 (1); quartz-andalusite - T2 (2); apophyses - T3 (3); simple concordant - T4 (4); potassium feldspar - T5 (5); simple discordant - T6 (6); petalite - T7 (7); spodumene - T8 (8); lepidolite and spodumene - T9 (9); lepidolite - T10 (10); quartz with cassiterite - T11 (11). Late-D3 granites (12); Complexo xisto-grauváquico (13); Formations of the Ordovician (14); Quartz veins (15); Granitic / rhyolitic porphyry and faults (16). Isograds: silimanite (17); andalusite (18); biotite (19)..... 12
- Figure 4 - Traditional model of the formation of a pegmatite field, based on an S-type granitic peraluminous pluton-related (Selway et al., 2005). LCT family pegmatites regional zoning. .... 14
- Figure 5 - Schematic crustal profile of the formation of pegmatites in a pluton-unrelated scenario. Formation based on partial melting of the crust. Simplified model of the zoning and enrichment of the pegmatitic field. Rare-metal pegmatites formed in this type of scenario may be lacking Li (therefore “CT” instead of “LCT”) or F (therefore “NY” instead of “NYF”) (adapted from Müller et al., 2017)..... 14
- Figure 6 - Location of the sampling sites, performed during the field trip of 6<sup>th</sup> and 7<sup>th</sup> of February 2020, to the Fregeneda-Almendra aplite-pegmatite field. In orange are represented the limits of the study area. Image source: Google Earth (Google Earth Pro, 2020). .... 20
- Figure 7 – High-resolution SR-6500 spectroradiometer (Spectral Evolution, Inc.). Optical fiber cable of 1.5 m of length. Image source: [https://www.alphaomega-electronics.com/5506-cart\\_default/sr-6500-espectrofotometro-de-alta-resolucao.jpg](https://www.alphaomega-electronics.com/5506-cart_default/sr-6500-espectrofotometro-de-alta-resolucao.jpg).. 23
- Figure 8 - Handheld Contact Probe, optical instrument. Image source: SR-6500 Operator’s Manual. .... 25

Figure 9 - Assembly scheme for the SR-6500 spectroradiometer. From left to right is possible to observe the spectroradiometer (on the left) connected to the Handheld Contact Probe (in the center) and (on the right) the computer to which the device is also connected, where a scene of DARWin SP is observed. .... 26

Figure 10 - Graphic representation of the twelve electromagnetic spectra obtained from the study of petalite minerals. The spectra shown with dashed line were removed from the elaboration of the spectral signature of petalite. .... 31

Figure 11 - Sample of the aplite-pegmatite vein of Bajoca mine T7 (448). The red circles represent the location where the measurement points were taken. In the left is find the point 13\_03\_00072 and in the right is find the point 13\_03\_00073. In both images inside the circle is observed a petalite mineral with visible alteration, marked by the dark to greenish tones. .... 32

Figure 12 - Small samples of petalite (449), collected in the aplite-pegmatite vein of Bajoca mine T7. In the left is represented the sample and face where measurement point 13\_03\_00127 was taken and in the right is represented the sample and face where measurement point 13\_03\_00131 was taken. .... 32

Figure 13 - Spectral signature of petalite. Obtained from the average of the spectra measure in the several petalite minerals studied. .... 33

Figure 14 - Spectral signature of petalite with the continuum removed. .... 34

Figure 15 - Portions of wavelength, where is observed the absorption of energy. (A, B, C, D) portions obtained from the slicing of the spectrum of petalite with the continuum removed. The red vertical lines correspond to the maximum absorption, in a determine peak of absorption. .... 35

Figure 16 - Fel-Lep sample. Aplite-pegmatite vein T9 from Feli mine. Lepidolite is represented by the crystals in purple tones. .... 38

Figure 17 - Bajoca-L sample. Sample of aplite-pegmatite vein with lepidolite, represented by the purple hued minerals. .... 38

Figure 18 - Graphic representation of the nine electromagnetic spectra obtained from the study of lepidolite minerals. .... 39

Figure 19 - Spectral signature of lepidolite. Obtained from the average of the spectra measure in the several lepidolite minerals studied. .... 40

Figure 20 - Spectral signature of lepidolite with the continuum removed. .... 41

Figure 21 - The four portions of wavelength used for the study of absorption zones in the spectral signature of lepidolite. The spectrum presented has the continuum removed. The red vertical lines represent the depth caused by the effect of absorption. The length of the red line is the percentage of absorption..... 42

Figure 22 - Sample from Alberto-3. Aplite-pegmatite vein T8 from Alberto mine. Inside the red circle is observed a mineral of spodumene, where the measurement point ALB3\_00004 was taken. .... 46

Figure 23 - Sample from Alberto-3. Aplite-pegmatite vein T8 from Alberto mine. Sample with SQUI, where is the presence of spodumene, in a with color, and quartz, in a more translucent tone. .... 46

Figure 24 - Graphic representation of the eight electromagnetic spectra obtained from the study of spodumene minerals, without quartz association..... 47

Figure 25 - Spectral Signature of spodumene. Obtained from the average of the spectra measure in the several spodumene minerals studied, without quartz association. .... 48

Figure 26 - Spectral signature of spodumene with the continuum removed. .... 49

Figure 27 - The four portions of wavelength (A, B, C, D) used for the study of absorption zones in the spectral signature of spodumene. The spectrum is presented with the continuum removed. The red vertical lines represent the depth caused by the effect of absorption. The length of the red line is the percentage of absorption. .... 50

Figure 28 - Spectral signature of spodumene VS Spectral signature of SQUI..... 51

Figure 29 - Aplite-pegmatite vein sample with zinnwaldite (observed in brownish colors). .... 52

Figure 30 - Graphic representation of the seven electromagnetic spectra obtained from the study of zinnwaldite minerals. .... 54

Figure 31 - Spectral signature of zinnwaldite. .... 55

Figure 32 - Spectral signature of zinnwaldite with the continuum removed. .... 56

Figure 33 - The four portions (A, B, C, D) sliced from the spectral signature of zinnwaldite spectrum with continuum removed. The red vertical lines represent the depth caused by the effect of absorption. The length of the red line is the percentage of absorption. .... 57

Figure 34 - Sample with a mineral of montebrasite, identified inside the red circle, from Massueime mine..... 59

Figure 35 - Graphic representation of the three electromagnetic spectra obtained from the study of a montebrasite mineral. .... 60

Figure 36 - Spectral signature of montebrasite..... 61

Figure 37 - Spectral signature of montebrasite with the continuum removed. .... 62

Figure 38 - The four portions (A, B, C, D) sliced from the spectral signature of montebrasite spectrum with continuum removed. The red vertical lines represent the depth caused by the effect of absorption. The length of the red line is the percentage of absorption..... 63

Figure 39 - Petalite VS Spodumene..... 67

Figure 40 - Petalite and spodumene spectral signatures with the continuum removed. .... 68

Figure 41 - Petalite VS Spodumene VS Lepidolite. Comparison between the three main lithium minerals from the Fregeneda-Almendra aplite-pegmatite field. .... 69

Figure 42 - Petalite VS Spodumene VS Lepidolite. Comparison with the continuum removed spectra. .... 70

Figure 43 - Lepidolite VS Zinnwaldite. Comparison with the continuum removed spectra. .... 71

Figure 44 - Sample of a T7 pegmatite, collected in Bajoca mine, at 448 location. Orangish-to-reddish tones, indicative of the presence of iron oxides..... 73

Figure 45 - Sample of a T7 pegmatite, from the stockpile of Bajoca mine. Presence of iron oxides. .... 73

Figure 46 - Sample of a T5 pegmatite, where is noticeable the intense presence of iron oxides. .... 74

Figure 47 - Graphic comparison of the spectra presented by the T5 pegmatite, T7 pegmatite and petalite..... 74

Figure 48 - Graphic comparison of the spectra with the continuum removed presented by the T5 pegmatite, T7 pegmatite and petalite. .... 75

Figure 49 - Metasedimentary sample from CXG, Desejosa formation (445)..... 77

Figure 50 - Metasedimentary sample from CXG, collected near a T5 aplite-pegmatite vein (T5-19). .... 77

Figure 51 - Metasedimentary sample from CXG, collected near a T6 aplite-pegmatite vein (TC-19)..... 77

Figure 52 - Metasedimentary sample from CXG, collected near a T7 aplite-pegmatite vein (T7-19). .... 77

Figure 53 - Metasedimentary sample from CXG, collected near a T8 aplite-pegmatite vein (ALB-19).....	78
Figure 54 - Graphic comparison of the CXG spectra.....	78
Figure 55 - CXG spectra with continuum removed.....	79
Figure 56 - Fresh granite sample from the Mêda-Penedono-Lumbrales Granitic Complex (452).....	80
Figure 57 - Altered granite sample from the Mêda-Penedono-Lumbrales Granitic Complex (453).....	80
Figure 58 - Altered and fresh granite spectral signatures.....	81
Figure 59 - Altered and fresh granite spectral signatures with the continuum removed.....	81
Figure 60 - Graphic comparison between petalite spectral signature and the highest rated matched reference spectrum with 97% of correlation (Montmorillonite_STx-1_NIC4bb_RREF (USGS Spectral Library (Kokaly et al., 2017)).....	83
Figure 61 - Graphic comparison between spodumene spectral signature and the highest rated matched reference spectrum with 98.4% of correlation (Montmorillonite_CM27_BECKb_AREF (USGS Spectral Library (Kokaly et al., 2017)).....	83
Figure 62 - Graphic comparison between SQUI spectral signature and the highest rated matched reference spectrum with 98.9% of correlation (Montmorillonite_STx-1_BECKb_AREF (USGS Spectral Library (Kokaly et al., 2017)).....	84
Figure 63 - Graphic comparison between lepidolite spectral signature and the highest rated matched reference spectrum with 96.6% of correlation (Endellite_GDS16_BECKb_AREF (USGS Spectral Library (Kokaly et al., 2017)).....	85
Figure 64 - Graphic comparison between zinnwaldite spectral signature and the highest rated matched reference spectrum with 97.7% of correlation (Muscovite_GDS119_Mt_Alamo_NIC4aa_RREF (USGS Spectral Library (Kokaly et al., 2017)).....	86
Figure 65 - Graphic comparison between petalite spectral signature and the reference spectrum of montmorillonite matched with 98.9% of correlation rate (ECOSTRESS Spectral Library (Baldrige et al, 2009)).....	87

Figure 66 - Graphic comparison between spodumene spectral signature and the reference spectrum of montmorillonite matched with 99.2% of correlation rate (ECOSTRESS Spectral Library (Baldrige et al, 2009))..... 88

Figure 67 - Graphic comparison between lepidolite spectral signature and the highest rated reference spectrum, muscovite, matched with 99.1% of correlation rate (ECOSTRESS Spectral Library (Baldrige et al, 2009))..... 89

Figure 68 - Graphic comparison between montebrasite spectral signature and the highest rated reference spectrum of amblygonite, matched with 98.8% of correlation rate (ECOSTRESS Spectral Library (Baldrige et al, 2009))..... 90

Figure 69 - Graphic comparison between zinnwaldite spectral signature and the highest rated reference spectrum of muscovite, matched with 98.9% of correlation rate (ECOSTRESS Spectral Library (Baldrige et al, 2009))..... 91

# 1. Introduction

Lithium (Li) has always been a chemical element with several potentialities and uses, having been applied overtime in the industries of ceramics and glass. Over the past decade, the demand for more environmentally friendly technologies and energies has led to an increase in the search of this chemical element, which became a strategic material for the XXI century. This increase of interest is mainly due to the necessity of producing more efficient rechargeable batteries (Greim et al., 2020), where Li allows greater energy storage, thus enabling the construction of electric vehicles, with a much lower environmental cost than a common combustion car.

Thus, it is mandatory to identify new Li deposits to fill this current demand. For such, it is of extreme importance that for this purpose are employed technics that allow a rapid delimitation of a target area, since this rapid identification of a target could mean a significant decrease on the whole cost of the exploration campaign. The LIGHTS (Lightweight Integrated Ground and Airborne Hyperspectral Topological Solution) project objectives are aligned with this same point where new and more efficient methods of identifying a mineral deposit are researched, namely through remote sensing, a technology with great potential, yet little explored for Li.

The European project LIGHTS is aiming towards new methods and tools for the geological exploration of Li, based on the use of remote sensing data. The main objectives of LIGHTS project are: 1) study the genesis of Li deposits; 2) implement detection cameras in the VNIR-SWIR range on UAV (unmanned aerial vehicle); 3) build databases for the quick processing of UAV-borne hyperspectral data acquired above pegmatitic Li ores; 4) design the ground checking methods; and 5) gather all data in an intelligent mapping software to produce score maps while performing the drone and ground acquisitions.

The main objective of this thesis is the study of the spectral signatures of several Li minerals, present at the Fregeneda-Almendra aplite-pegmatite field, being inserted within the scope of the work carried out by the aforementioned project. Through the identification of these spectral signatures, it is intended to help solving several problems occurred during the previous works on remote sensing carried out within LIGHTS in this aplite-pegmatite field, particularly in the application of classification algorithms developed by Cardoso-Fernandes et al. (2018; 2019a). To this end, the obtained spectral characteristics and diagnostic features of the Li minerals are compared, with each other,

as well as compared to the signatures of the host lithologies, for a better understanding of the whole spectral picture from the study area. The Li minerals spectral signatures are also matched to reference spectra present in the free-access spectral libraries of USGS (United States Geological Survey), ECOSTRESS (ECOSystem Spaceborne Thermal Radiometer Experiment on Space Station), and CPRM (Companhia de Pesquisa de Recursos Minerais).

The present thesis is structured into 5 chapters, organized as follows: 1. Introduction, where the objectives of the present study are described, as well as, some information about remote sensing and also about the previous works performed in the study area; 2. Geographical and Geological Setting, geographic identification of the study area, and correspondent description of the geological context; 3. Sampling and Methodology, identification of the number of samples available, and its origins, as well as, the explanation of the methodology used for the analysis and a general description of the main characteristics and operating mode of the SR-6500 spectroradiometer used for the study; 4. Results, where all the results obtained are explained and discussed; 5. Conclusion, a description of the main ideas to get from this study, and an identification of a few techniques to be employed in the continuation of this study.

## 1.1 Remote Sensing

Remote sensing is a science that provides a set of techniques that allows obtaining information of an object without being in direct contact with that same object. That is, it allows to obtain, process, and interpret information, resulting from the interaction between the atoms/molecules of matter and the electromagnetic energy, in a process that occur at distance (Sabins, 1997). Where the observed features are produced by electronic and/or vibrational processes (Clark, 1999; Gaffey *et al.*, 1993 Hunt and Ashley, 1979; Hunt, 1977).

Considering remote sensing, it is possible to define the measurement of radiance or reflectance. Radiance is a variable measured directly by the instrument of remote sensing (Ray, 1994). Reflectance is the ratio between the quantity of light, which is reflected by an object, with the quantity of light, which is incident in that same object (Ray, 1994). Although reflectance may be influenced by some factors, radiance is very dependent on the illumination, orientation, and position of the target, which is why in many studies preference is given to reflectance measurements, as external factors are more easily overcome and mainly because reflectance is a property of the measured

material, making more reliable and repeatable studies possible. These measurements are acquired on the dependency of the electromagnetic wavelength, where this function results in a spectrum. The quantity of energy that is absorbed in a determined wavelength is defined by a parameter called absorption.

Remote sensing can cover a large section of the electromagnetic spectrum, from the visible to the microwave, being divided into four main regions: Visible (VIS); Reflected Infrared (RI); Thermal Infrared (TIR); and Microwave. The VIS region has a wavelength between 400 nm and 700 nm, and is essentially divided into three main bands, Blue, Green, and Red. The RI situates between 700 nm and 3000 nm, divided into two zones, the Near Infrared (NIR) (700-1300 nm), and the Short-Wave Infrared (SWIR) (1300-3000 nm). The latter is of great importance for remote sensing in geology. TIR is presented inserted within the wavelengths of 3000 nm to 14000 nm. Lastly, the Microwave region corresponds to the wavelength range from 1mm to 1m. In the present work, the spectra studied refer only the wavelength between 350 nm and 2500 nm, due to the spectral range of the spectroradiometer in use.

In geology, the features observed in a reflectance spectrum are based on the differences of chemical and physical properties of minerals and, consequently, rocks. Distinct minerals will emit different quantities of electromagnetic energy at various wavelengths due to the absorption of energy caused by the properties of the mineral, resulting in a unique electromagnetic spectrum. Therefore, through the identification of this spectrum, it will be possible to identify the mineral in the study (Bachri et al., 2019). However, in some cases, the spectrum presented may be affected by spectral features of alteration minerals, thus becoming difficult to correctly predict the minerals under study.

Spectroscopy has already proved to be a powerful tool in several disciplines of Geoscience, having been utilized since the '70s in the exploration of hydrothermal gold deposits (Moradi et al., 2014). It was only recently applied to the exploration of Li mineralizations, where Perrotta et al. (2005) have used a scene from the ASTER sensor, in the region of Vale do Jequitinhonha, Brazil, in an attempt of mapping the pegmatite intrusions related to Li mineralizations. Mendes et al. (2017) have also attempted to identify the spectral signatures of Li minerals, to facilitate the identification of future Li deposits. However, is Cardoso-Fernandes et al. (2018, 2019a) who have been publishing successive works, in which are described the attempts to demonstrate the application of remote sensing, in the identification and delimitation of possible litiniferous

deposits, in the aplite-pegmatite field of Fregeneda-Almendra, within the objectives of the LIGHTS project.

Nowadays, the exploration of Li with the resource to remote sensing is essentially done by recognizing the alteration zones associated with Li-bearing pegmatites (Cardoso-Fernandes et al., 2019a). To this end, innovative methodologies have been used to predict the occurrence of iron oxides and clay minerals, as well as the capacity to define the alteration zones and identify the areas of the potential presence of Li-bearing pegmatites. Therefore, the detailed knowledge of the spectra present in the target area is extremely relevant, so that the best possible selection of the classification algorithms to be applied can be made.

## 1.2 Previous Works

The application of remote sensing as a tool for Li exploration, is relatively new, with works published only in recent years. In Fregeneda-Almendra aplite-pegmatite field, intending to detect and identify Li-bearing pegmatites, Cardoso-Fernandes et al. (2018; 2019a) applied a methodology based on RGB (Red-Green-Blue) combinations, Band Ratio, Selective Principal Component Analysis (PCA), and Supervised Classification, utilizing different algorithms. Similar works of remote sensing for Li exploration were also published by Santos et al. (2019) and by Gemusse et al. (2018, 2019).

The Fregeneda-Almendra aplite-pegmatite field is a region where three open-pit mines exist, Bajoca, Alberto, and Feli, which are an important factor for the application of the methodology developed by Cardoso-Fernandes et al. (2018; 2019a), since these authors use these areas, where Li-bearing pegmatites are already known, as training zones for the spectral recognition, to apply the algorithms to new areas not yet explored.

The RGB combinations generally have a poor performance, since they were developed for mineral deposits of a different nature than the Li deposits. Furthermore, the application of RGB combinations confuse burnt areas with zones of alteration. Thus, is understood the need for more detailed studies for these alteration minerals, associated with Li mineralizations, as well as the study of their spectral signatures, to promote an easier identification and distinction. The successive failures in the various possible configurations for the use of Band Ratio, demonstrate this same need, for a better understanding of the minerals spectral behaviors. In the same way, Selective PCA, even though had presented better results, also showed the need for the continuation of spectral studies (Cardoso-Fernandes et al., 2019a).

The application of data machine learning (ML) algorithms, such as Support Vector Machines (SVMs) and Random Forrest (RF) (Cardoso-Fernandes et al., 2019b), demonstrate the importance of the inclusion of these more advanced and robust algorithms in the studies since both were capable of identifying the presence of Li-bearing pegmatites in the three open-pit mines, as well as, in other areas where these pegmatites are known, although, some selected areas are coincident with barren pegmatites. The SVMs results were more accurate, however, was RF the algorithm which has classified the higher number of Li-bearing pegmatites. The results of these algorithms application have also presented a few false-positive responses, which shows the high difficulty of them in separating the spectra of metasediments from the spectra of Li-bearing pegmatites, demonstrating once again the high necessity of a better knowledge of the Li minerals spectral signatures.

Santos et al. (2019) aiming to identify potential areas for the exploration of Li, in the pegmatitic districts of São João Del Rei and of Araçuaí, south, and northeast, respectively, of Minas Gerais, Brazil, have applied the same methodology of Cardoso-Fernandes et al. (2018; 2019a). Despite some weaknesses, the use of this methodology showed once more the great utility in the identification of Li mineralizations.

A similar methodology was used by Gemusse et al. (2018, 2019), to map and identify the occurrence of Li-bearing pegmatites in the Alto da Ligonha region, in the northwest of Mozambique. Gemusse et al. (2018) have also used a spectroradiometer to analyze the spectral behavior of several pegmatite samples, having used this newfound data in classification algorithms. The results showed a good correlation to what was already known for this region, demonstrating the importance of spectral knowledge in this type of studies.



## 2. Geographical and Geological Setting

### 2.1 Geographical Setting

The study area is located in the Fregeneda-Almendra aplite-pegmatite field (Figure 1) in the western part of the Iberian Peninsula. The region of Almendra-Barca D'Alva (Vila Nova de Foz Côa and Figueira de Castelo Rodrigo, Portugal, respectively), compose the westernmost part of the aplite-pegmatite field, and is situated in the transition zone of the Portuguese regions of Beira-Alta and Alto-Douro. This region is delimited to the west by the Vilaríça fault and the east by the Águeda river. The Águeda river not only constitutes a division in two parts of the aplite-pegmatite field but also, materializes the border between Portugal and Spain. In this way, the area extends to the east, reaching the villages of La Fregeneda and Hinojosa del Duero, in the Salamanca region, Spain. The whole study area is delimited to the north by the Douro river course, being largely included in the limits of the natural parks of Douro Internacional and Arribes de Duero.

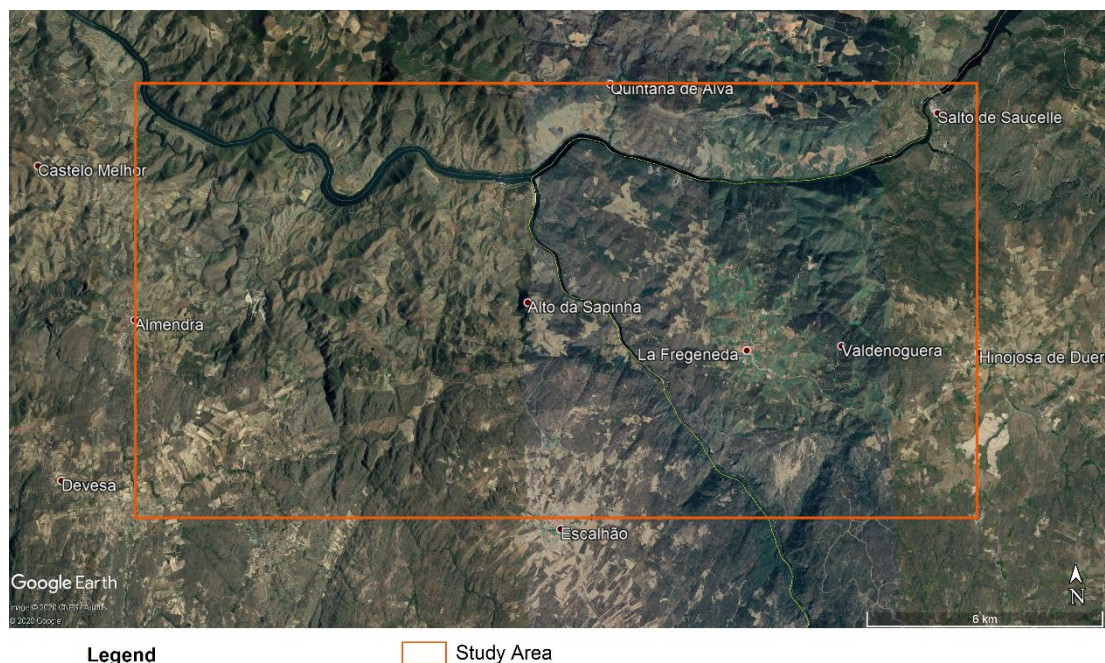


Figure 1 - Location of the study area. The study area represented is coincident with the geographical expression of the aplite-pegmatite field of Fregeneda-Almendra. Image source: Google Earth (Google Earth Pro, 2020).

## 2.2 Geological Setting

The Fregeneda-Almendra aplite-pegmatite field is situated in the Iberian Massif, a fragment of the European Variscan Belt, mainly composed of magmatic and metamorphic rocks of ante-Ordovician and Paleozoic ages. This belt deals with a folding of NW-SE direction resulting from the collision between two continents, in the Paleozoic, more specifically in the Carboniferous, through a long and complex process of convergence. Initially, the oceanic crust was subducted, culminating later in the collision of several continental blocks, originating the Variscan Belt (Quesada, 1992; Chaminé, 2000; Marques et al., 2000). As a result of the different geological characteristics, which made up the already present continental lands, and with the forces associated to the formation of the Variscan Belt, the Iberian Massif was divided into several geotectonic zones, parallel to the Variscan Belt, with different paleogeographic, structural, magmatic, and metamorphic characteristics (Julivert et al., 1974). These zones are correspondent to the: Cantabrian Zone (CZ); West Asturian-Leonese Zone (WALZ); Galica Trás-os Montes Zone (GTMZ); Central Iberian Zone (CIZ); Ossa-Morena Zone (OMZ); and Sul-Portuguesa Zone (SPZ) (Dallmeyer & Garcia, 1990) (Figure 2).

The study area is integrated into the Central Iberian Zone (CIZ) (Farias et al., 1987; Julivert, 1972; Lotze, 1945) (Figure 2), a zone that occupies the innermost and stable part of the Iberian Massif. This geotectonical zone is characterized through the predominance of pre-orogenic sequences, described as autochthonous metasedimentary formations, of Precambrian and/or lower Cambrian ages, deposited over the Cadomian massif and intruded by pre-Variscan granites, as well as Variscan granitoids (Dias et al., 2000; Martínez Catalán et al., 2004; Martínez Catalán et al., 2009). The general structuration present in CIZ is visible through the presence of folds, resultant from the actuation of the Variscan orogeny, especially of the actuation of the first phase of deformation (D1) (Ribeiro et al., 1979; Díez Balda et al., 1990; Dias and Ribeiro, 2013).

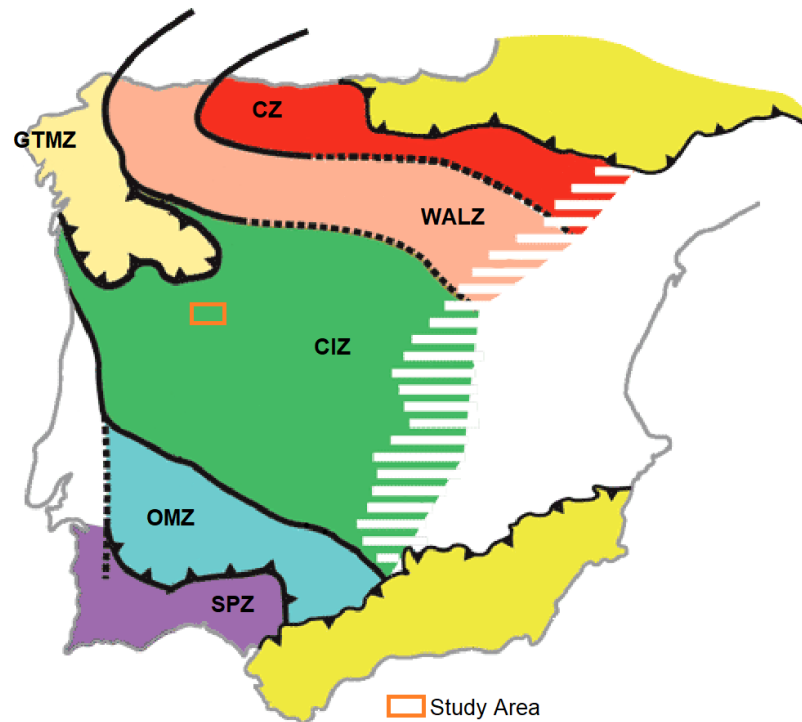


Figure 2 - Synthesis of the geotectonic zones present in the Iberian Massif (adapted from Gourvennec et al., 2010; Julivert et al., 1974; Dallmeyer & Garcia, 1990; Farias et al., 1987). Location of the study area in the geotectonic zones. Legend: CZ - Cantabrian Zone; WALZ - West Asturian-Leonese Zone; GTMZ - Galicia Trás-os Montes Zone; CIZ - Central Iberian Zone; OMZ - Ossa-Morena Zone; SPZ - Sul-Portuguesa Zone.

The region of study is mostly constituted by metasedimentary terrains, stretched in an E-W direction, belonging to the designated by Costa (1950) and Teixeira (1955) Complexo Xisto-Grauváquico (CXG). The CXG in this region is limited “to the north by the quartzitic formations of Poiares synclinal (Lower Ordovician), to the south by the Mêda-Penedono-Lumbrales Granitic Complex (MPLGC), to the west by Vilarica fault and northeast by Saucelle Granite” (in Vieira, 2010), as is possible to observe at Figure 3.

The Complexo Xisto-Grauváquico (CXG), of ages between the Upper Proterozoic and the Lower Cambrian, is a series of pelitic-sandy flysch, composed of pelitic schists interspersed by metaconglomerados and metagraywackes (Díez Balda et al., 1990; Rodríguez Alonso et al., 2004). Which outcrop in broad antiforms located, in Portugal, in the Douro Valley and in the Beiras region, spreading through Spain, in Salamanca, Estremadura, Montes de Toledo and Alcudia (Rodríguez Alonso, 2004; Silva, 2014; Silva, 2005).

In the region of study, CXG is identified through the occurrence of quartzites, graywackes, metagraywackes, schists and, pelites, interspersed with thin calco-

silicataded layers (Roda et al., 1999), corresponding to the designated Douro Group. Sousa (1982; 1983) has established for this group a stratigraphic succession of six distinct formations, which from the base to the top are: Bateiras formation, Everdosa do Douro formation, Rio Pinhão formation, Pinhão formation, Desejosa formation, and São Domingos formation. Silva and Ribeiro (1985) after detecting an assumed sin-sedimentary carriage, of Sarda age, in Senhora do Viso region (Vila Nova de Foz-Côa), have proposed a tectonic duplication in the Douro group, in which the top formations of Rio Pinhão and Pinhão would be the lateral equivalent to the base formations of Bateiras and Everdosa do Douro, respectively. In this way, Sousa and Sequeira (1989) have organized these CXG metasediments in two different sets: autochthonous and allochthon. Where the basal formations of Bateiras and Everdosa do Douro are considered as autochthonous, and the top formations of Rio Pinhão, Pinhão, and Desejosa are allochthones. Romão et al. (2005) suggest the São Domingos formation as a contemporaneous deposit to the Senhora do Viso carriage.

According to Vieira (2010), in the study area, is only possible to identify the allochthones formation of Rio Pinhão, Pinhão, and Desejosa, where the formations of Rio Pinhão and Pinhão are presented with a lesser cartographic expression when compared to the expression of Desejosa formation. The most abundant lithologies of Rio Pinhão formation are metagraywackes and/or metaquartzwackes, thinly interspersed with dark-grey to dark phyllites. The Pinhão formation outcrops in a stretched band, of E-W orientation, which spreads from the Vilarica fault to the Portugal-Spain border, in Águeda river. This formation is identified through greenish lithologies finely interspersed, with alternances of phyllites and quartzphyllites with thin layers of metagraywackes and/or metaquartzwackes (Vieira, 2010). The Desejosa formation is characterized by the occurrence of striped schists, where the striped aspect is acquired through thin alternances of dark phyllitic layers and whitish psamites (Vieira, 2010), in certain zones is also possible to observe the occurrence of calco-silicataded levels (metagraywackes calco-silicataded) (Sousa, 1981; Oliveira, 1982; Silva and Ribeiro, 1991, 1994; Gaspar, 1997).

Because the study area is part of CIZ and because CXG lithologies are the oldest observable in the region, it is possible to recognize the presence of the three main phases of Variscan deformation (D1, D2, D3), defined by Noronha et al. (1979), usually considered as responsible for the structuration of this part of the Variscan belt.

The D1 phase generated large folds of NW-SE trending orientation with a sub-vertical axial plan in the autochthonous terrains (CIZ) (Noronha et al., 2006). This folding

is associated with a schistosity ( $S_1$ ) parallel to the axial plan (Ribeiro et al., 1979; Díez Balda et al., 1990). The D2 phase is a very local deformation that has originated sub-horizontal shear zones, affecting especially the ante-Variscan and premature Variscan granitoids, generating stretching lineations (Vieira, 2010). According to Díez Balda et al. (1990), D2 has also generated smaller folds highly asymmetric with vergence to SE, affecting the  $S_1$  cleavage and developing a sub-horizontal schistosity. D3 phase developed large open folds with sub-vertical axial planes and an N100°E to N120°E orientation associated with a sub-vertical cleavage of crenulation (Pereira et al., 1993; Noronha et al., 2006). In association with this last phase, there are important sinistral and dextral shear zones of distensive component, WSW-ENE to WNW-ESE and NW-SE, respectively (Vieira, 2010).

Post-D3 phases were developed under ductile-brittle to brittle regimes, generating important sinistral movements, through NNE-SSW fractures, which cut and reject the previous structures, dextral movements are also identified through NNW-SSE fractures (Noronha et al., 2006; Vieira, 2010). These fractures and the fractures originated from the actuation of the D3 deformation phase control the installation of granites, in such a way that granites distributed along fractures related with D3 shear zones are considered as syn- to late-tectonic, and granites distributed along brittle fractures are considered as post-tectonic (Ferreira et al., 1987; Noronha et al., 2006; Frutuoso, 2015).

According to Ferreira et al. (1987), Noronha et al. (2006), and Dias et al. (2010) Variscan granites can be divided into two groups, two mica granites, and biotitic granites. In the region of the present study, the CXG lithologies are mainly intruded by two mica granites.

South to the border of CXG, outcrops the great Mêda-Penedono-Lumbrales Granitic Complex, mainly constituted by syn-D3 lithofacies, excepting for a few granites of small-expression which are late-D3 (Ribeiro e Silva, 1994; Silva e Ribeiro, 1991), such as the Lumbrales granite which has been dated to  $300 \pm 8$  Ma (Garcia Garzón & Locutura, 1981). These granites are classified as two mica, leucocratic, of heterogenous aspect and with a granulometry between fine and medium grain (Ferreira et al., 1987; López-Plaza & Carnicero, 1988; Silva & Ribeiro, 1991), they are still peraluminous granites, highly evolved and enriched in rare metals (Gaspar, 1997; Vieira & Lima, 2005a, b).

In the northeast part of the aplite-pegmatite field, outcrops the Saucelle granite, also a two-mica granite, peraluminous, of age late-to-post-D3 (Ribeiro e Silva, 1994). In

the same way to what happens with the syn-D3 MPLGC granites, also this one is installed in an antiform, due to the action of the forces from the Variscan orogeny (Ribeiro e Silva, 1994; Silva e Ribeiro, 1991).

The non-outcropping Feli granite was detected during a drilling campaign between Riba D’Alva (Portugal) and Feli mine (Spain). This is a leucocratic granite, essentially muscovitic, of grain fine to medium and with a hypidiomorphic texture (Vieira, 2010). The geochronology studies have dated this granite to  $305 \pm 3,3$  Ma (Vieira, 2010), thus showing a late-D3 age.

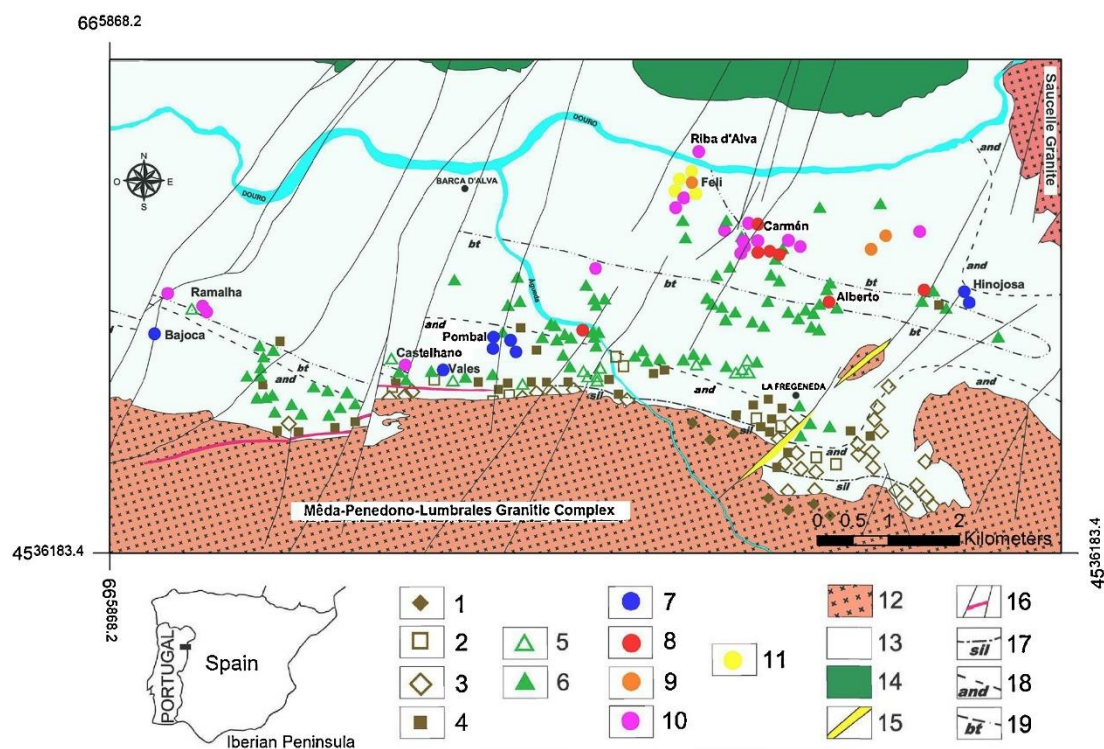


Figure 3 - Simplified geological map of the Fregeneda-Almendra aplite-pegmatitic field (Viera, 2010). Vein types : intra-granitic - T1 (1); quartz-andalusite - T2 (2); apophyses - T3 (3); simple concordant - T4 (4); potassium feldspar - T5 (5); simple discordant - T6 (6); petalite - T7 (7); spodumene - T8 (8); lepidolite and spodumene - T9 (9); lepidolite - T10 (10); quartz with cassiterite - T11 (11). Late-D3 granites (12); Complexo xisto-grauváquico (13); Formations of the Ordovician (14); Quartz veins (15); Granitic / rhyolitic porphyry and faults (16). Isograds: silimanite (17); andalusite (18); biotite (19).

### 2.2.1 General Geology of The Pegmatite

Lithium is a chemical element that can be found in a large variety of mineral deposit types, although, in Europe, the deposits with the most importance have the Li hosted in pegmatites (Kesler et al., 2012). The Iberian Peninsula constitutes an area of high interest, with several aplite-pegmatite fields recognized, such as the Fregeneda-Almendra aplite-pegmatite field, where approximately 800 pegmatitic bodies have already been mapped (Roda et al., 1999).

According to London (2008), a pegmatite is defined as an essentially magmatic rock of predominantly granitic composition, which is distinguished from other magmatic rocks, for its extremely coarse granulometry, that normally increases from the center to the margin of the pegmatite, is distinguished also, for the abundance of dendritic forms, graphic or any other habit of directional growth. Pegmatites occur in homogeneous to zoned bodies, installed in igneous or metamorphic rocks, taking advantage of weakness zones, such as shear zones, to accumulate. These are usually associated with parental granites, although currently there are studies that defend the possibility of an origin without relation to a parental granite (Müller et al., 2017), resulting in this way, from partial fusion and crustal anatexis, or even, from the melt circulation along deep lithospheric fault zones (Zagorsky et al., 2014). Therefore, there are two distinct genetic models, based on the production of melt for the origin of pegmatites: 1) melt results from the fractional crystallization of granitic magmas, in which silicon is separated and installed in the host metasedimentary rocks, where it will crystallize and form pegmatites (Dill, 2015), this model presents in this way an origin based on a parental granite (Figure 4); 2) melt originates, in the presence of fluids, through the partial fusion of the crust or mantle rocks (London, 2005) (Figure 5), not being directly related to a parental granite.

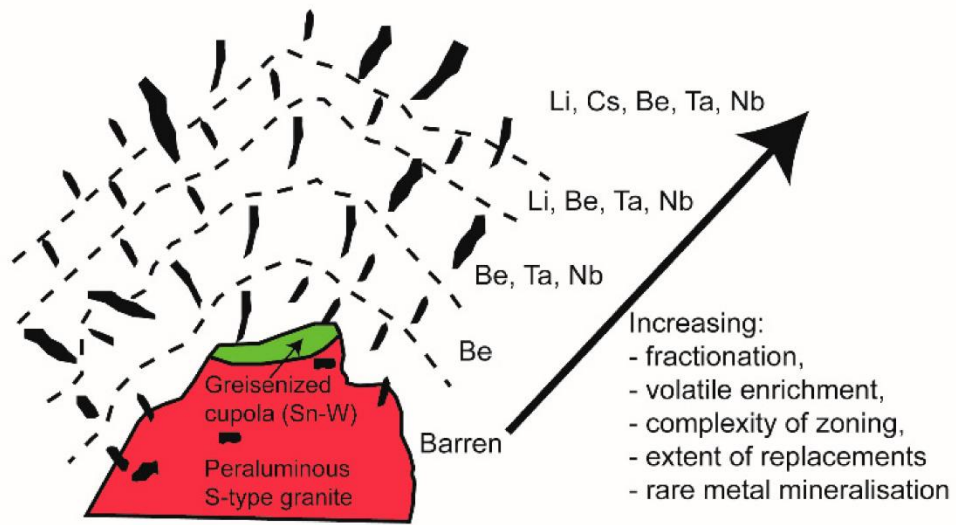


Figure 4 - Traditional model of the formation of a pegmatite field, based on an S-type granitic peraluminous pluton-related (Selway et al., 2005). LCT family pegmatites regional zoning.

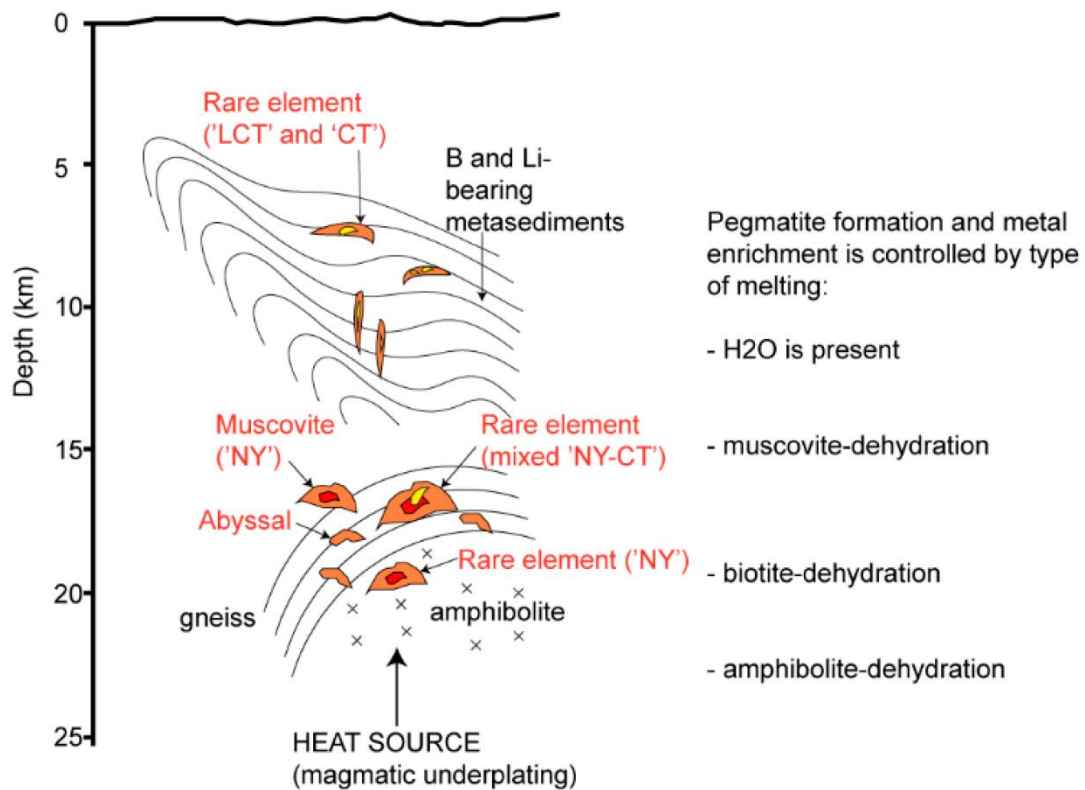


Figure 5 - Schematic crustal profile of the formation of pegmatites in a pluton-unrelated scenario. Formation based on partial melting of the crust. Simplified model of the zoning and enrichment of the pegmatitic field. Rare-metal pegmatites formed in this type of scenario may be lacking Li (therefore "CT" instead of "LCT") or F (therefore "NY" instead of "NYF") (adapted from Müller et al., 2017).

According to the pegmatitic classification of Černý and Ercit (2005), there are two families of pegmatites, LCT (Lithium, Cesium, Tantalum) family, and NYF (Niobium, Yttrium and Fluorine) family. Is to the LCT family that belong the Li minerals of higher economic value and the most sought after today, being them, spodumene, lepidolite, and petalite, which according to this same classification are included in the REE-Li (Rare-earth elements-Li) subclass and in the Complex type. This classification was obtained through studies of the mineralogical and geochemical composition, as well as, through the presented structure and P-T conditions (pressure and temperature). Despite these two genetic models, for the origin of the LCT pegmatites, it is nowadays more accepted the existence of a direct relationship with an S-type peraluminous parental granite (Černý et al., 2012), which is what the first model advocates. Through the observation of this model (Figure 4), it is noticeable that the LCT pegmatites are the ones that present a greater distance from the source, or better, from the parental granite. In this way, this model presents an ideal view of what is often recognized in the fieldwork, a regional zoning, where is possible to observe, from a proximal zone to a distal zone of the parental granite, a sequence of pegmatites with different enrichments. Initially are installed pegmatites enriched in Be, passing then to Be-Nb-Ta enriched, followed by Li-Be-Nb-Ta enriched and finally Li-Cs-Be-Ta-Nb (LCT) enriched pegmatites.

The LCT pegmatites are usually related to orogenic processes, involving terrains of high metamorphism degree, and exhumed or reworked continental crust (Steiner, 2019). The fertility of these pegmatites is in dependence of the presence of sedimentary protoliths rich in Li, Cs, Sn, and W, accumulated along the continental margins, as a result of tectonics and sedimentary processes, as well as, of a mantle heat source, to promote the mobilization of these elements for the peraluminous melt (Romer et al., 2016).

In the region of study, by combining several factors, such as mineralogy, morphology, internal structure, and relationship with the host rocks, eleven types of aplite-pegmatite veins were defined and characterized, being generally found installed in the CXG metasediments, with few intragranitic occurrences (Roda, 1993; Roda et al., 1999; Vieira, 2010), as it is represented in Figure 3.

Of the eleven types defined, classified from T1 to T11, only four correspond to Li-bearing veins, considered as belonging to the LCT family: T7 – petalite-bearing aplite-pegmatite veins; T8 – spodumene-bearing aplite-pegmatite veins; T9 – spodumene- and lepidolite-bearing aplite-pegmatite veins; T10 - lepidolite-bearing aplite-pegmatite veins (Vieira, 2010).

The T7 aplite-pegmatite veins occur in the Pinhão and Desejosa formations, in veins with no apparent internal zoning, although there are zones richer in petalite. In the contact with the host rocks, is often possible to observe the presence of turmalinization (Vieira, 2010). As for mineralogy, these aplite-pegmatite veins are constituted by petalite, quartz, albite, and potassic feldspar, with smaller phases such as muscovite and cassiterite (Vieira, 2010). A better example of this type of occurrence is the Bajoca mine.

The T8 aplite-pegmatite veins are mainly recognized in the eastern part of the Fregeneda-Almendra aplite-pegmatite field, being the main body outcrop in the Alberto mine, north of La Fregeneda. These veins are very similar to those identified as belonging to T7 veins, with identical mineralogy and showing discordant attitudes from the host rocks, with N-S to N30°E directions and subvertical dip, presenting thicknesses greater than one meter. However, in the T8 aplite-pegmatite veins spodumene is the dominant aluminosilicate phase, which occurs associated with primary petalitic masses. The macroscopic association of these two phases was only identify, up to now, in Alberto mine (Vieira, 2010). Spodumene can be found with intergrown quartz, in structures named SQUI (Vieira, 2010).

The T9 aplite-pegmatite veins are composed of quartz, feldspar, litiniferous-muscovite (lepidolite), and spodumene, where muscovite, cassiterite and montebrasite may also occur, as well as, accessory phases of apatite, Nb and Ta oxides, Fe-Mg phosphates, and eucryptite (Vieira, 2010). These veins are presented with an internal banded structure, where spodumene appears in association with lepidolite and potassic feldspar. Concerning the MPLGC, these are the most distant, being similar to the T7 and T8 in attitude (Vieira, 2010). The Feli mine is the most studied example of this type.

The aplite-pegmatite veins classified as T10 are discordant from the host rocks, presenting directions that vary between N10° and N40°, with a subvertical dip and a thickness which do not exceed three meters (Vieira, 2010). Mineralogically they are constituted by quartz, feldspars, and litiniferous-muscovite (lepidolite), wherein some cases it is possible to understand an internal banded structure (Vieira, 2010).

The remaining types of veins classified by Vieira (2010) are considered as barren for the presence of Li. They occur with the same direction of the tectonic foliation provided from the Variscan D3 deforming phase, of N110° to N120° attitude, appearing installed in intragranitic zones or near granitic plutons (Vieira, 2010) (Figure 3).

### 2.2.2 Mineralogy

The pegmatites present in the study area, in general, have an essentially granitic mineralogical composition, with quartz, feldspars, and micas. Feldspars, plagioclases and potassic feldspars, occur in the veins of the study area, in a such way that the albite portion (sodic plagioclase) increases in relation to the potassic feldspars portion as it gets further away from the MPLGC. This association with what has been already referred to the distance of the Li-bearing veins to this granitic complex, shows that the presence of albite is more common in the Li-mineralized veins than potassic feldspar (Vieira, 2010). Depending on the type of aplite-pegmatite vein under study, potassic feldspars present different trace elements, for example, when associated to veins with lepidolite, potassic feldspars appear enriched in Li (Roda et al., 1993; Roda et al., 1999). This ability to incorporate different trace elements leads some researchers to use them as indicators of the pegmatitic differentiation (Černý et al., 1985; Shearer et al., 1985; Černý, 1994; Neiva, 1995; Roda et al., 1999).

According to Vieira (2010), pegmatites rich in rare elements belonging to the LCT family have muscovite as the predominant mica, giving to the veins its peraluminous character. Throughout the study area, several Li micas that can be found, with lepidolite being the most recurrent one, present in two out of the eleven types of aplite-pegmatite veins (T9 and T10). Cookeite, Li chlorite, is another possible mica to be found, it appears in small crystals intergrown with muscovite, associated with the alteration of Li aluminosilicates, petalite and spodumene (Vieira, 2010). Zinnwaldite is also Li mica, of very fine grain, that can be found in the vein of Bajoca mine, in the Feli granite, and in the surroundings of Feli mine (Vieira, 2010).

Petalite and spodumene occur in the veins of the Fregeneda-Almendra aplite-pegmatite field. Both are Li aluminosilicates, which means, that they are constituted by Li, Al, Si, and O. Petalite is stable at relatively high temperatures. However, when the temperature drops below that of the stability field of petalite, one spodumene and two quartz minerals crystallize instead of petalite, hence maintaining the global chemical composition. Thus, arises an intergrowth of spodumene and quartz (SQUI), where the growth happens orthogonally to the major axis of the petalite crystals (Černý e Ferguson, 1972). In this way, spodumene can occur, in Fregeneda-Almendra aplite-pegmatite field, as a result of petalite alteration or as a primary phase. In some cases, is detected the presence of eucryptite as a product of the alteration of these two Li minerals, accumulating along cleavages, fractures, or crystals contacts (Vieira, 2010).

Normally, in association with the Li-bearing pegmatites, a halo of alteration is generated by hydrothermal processes. According to Sabins (1999), there are two groups of minerals associated with altered rocks by hydrothermal processes: 1) alunite and clay minerals, such as illite, kaolinite, and montmorillonite; 2) iron oxides and sulfates. For this reason, beyond the principal mineralogy of the Li-bearing pegmatites, it is almost always possible to identify these groups of minerals, as a result of hydrothermal alteration.

### 3. Sampling and Methodology

The samples treated during the studies carried out in this work, came from several locations of the Fregeneda-Almendra aplite-pegmatite field. A total of 68 hand samples, from 46 different sampling sites, have been measured, resulting in 399 spectra. Of these samples, 25 are of aplite-pegmatite veins, where was recognized the presence of Li minerals, collected in 13 different locations, totaling 170 measured spectra. The remaining samples consist in metasediments, from CXG, and in granites from the MPLGC.

During a field trip to the Fregeneda-Almendra aplite-pegmatite field, done on the 6<sup>th</sup> and 7<sup>th</sup> of February 2020, part of the studied samples was collected. These samples were collected in exposed areas and open-pit mines, being mainly samples of CXG metasediments, having been also sampled, in four different sites, the T7 aplite-pegmatite vein (petalitic) of Bajoca mine. Table 1 details information on the sampling locations carried out in this field trip. Being identified by a code, it is possible to understand how many samples were collected, by each location, and how many spectra were obtained, as well as a brief description of the sample. In Figure 6, is observed the sampling sites performed in the Fregeneda-Almendra aplite-pegmatite field. A part of the sampling sites is outside the limits of the study area, being representatives of CXG metasediments and MPLGC granite samples. The points 449 and 448, identify two sampling sites in the Bajoca mine aplite-pegmatite vein. In Figure 6, points PP01, BJ1-01, and BJ1-02 are not identified, since these were loose samples or were part of the stock-pile of the Bajoca mine, and the place origin is unknown.

The remaining samples studied were made available by the Departamento de Geociências, Ambiente e Ordenamento do Território, da Faculdade de Ciências da Universidade do Porto, having been collected over time, in different locations of the Fregeneda-Almendra aplite-pegmatite field. These are samples of CXG metasediments and litiniferous aplite-pegmatite veins of different types, thus allowing the study of the spectral signatures of the different minerals. In Table 2, in the same way as before, there is more detailed information about the samples.

In general, the studied samples show signs of alteration, even when observing a recently broken surface. This alteration is verified by a granular touch when passing the finger on the sample surface, and by the identification of typical alteration minerals, such as clay minerals. On surfaces exposed to the elements, it is possible to verify, in

many cases, the presence of iron oxides and small signs of vegetation, such as mosses and lichens.

Table 1 - Description of the samples collected during the field trip, of 6<sup>th</sup> and 7<sup>th</sup> of February 2020, to the Fregeneda-Almendra aplite-pegmatite field.

Identification	Description	Samples	No. of Measurements
439	CXG: Desejosa formation; sample taken on a sub-horizontal joint surface.	1	11
440	CXG: Desejosa formation; fresher sample.	2	16
441	CXG: Desejosa formation; altered sample.	1	15
PP01	CXG: Desejosa formation;	1	7
442	CXG: Desejosa formation; soil stirred with several blocks of schists.	1	10
443	CXG: Desejosa formation; soil stirred with several blocks of schists.	2	12
444	Loose quartzite blocks.	3	21
445	CXG Desejosa formation sample.	3	14
446	CXG Desejosa formation sample.	3	13
448	T7 vein; petalite sample.	4	16
BJ1-01	T7 vein (stock-pile of Bajoca mine).	4	29
BJ1-02	T7 vein (stock-pile of Bajoca mine).	2	9
449	T7 vein; petalite sample.	2	8
452	Fresh granite sample.	1	13
453	Altered granite sample.	3	20
454	Granite sample.	1	4

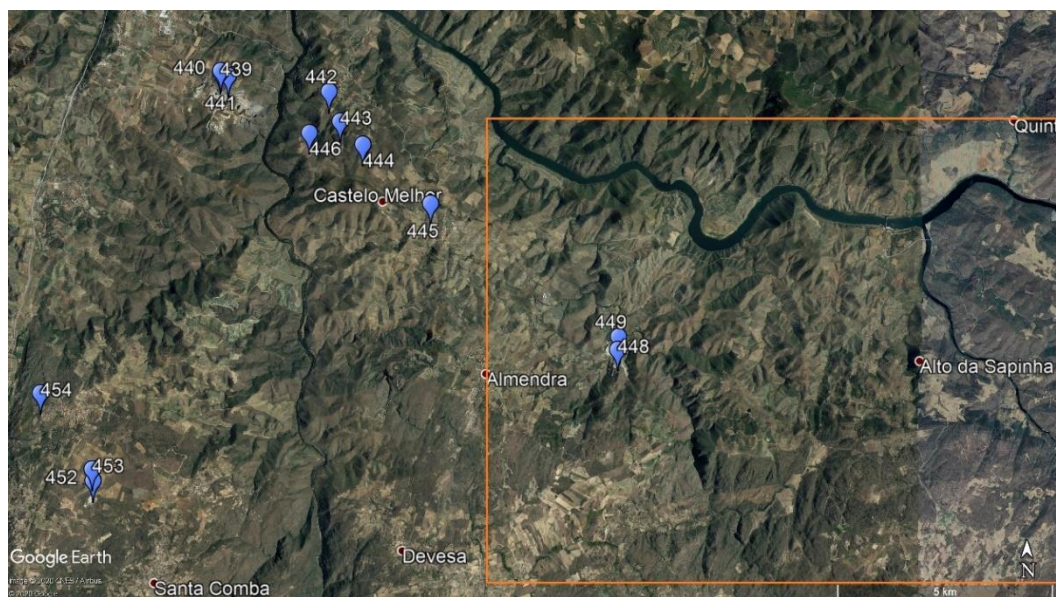


Figure 6 - Location of the sampling sites, performed during the field trip of 6<sup>th</sup> and 7<sup>th</sup> of February 2020, to the Fregeneda-Almendra aplite-pegmatite field. In orange are represented the limits of the study area. Image source: Google Earth (Google Earth Pro, 2020).

Table 2 - Description of the studied samples, made available by the Department of Geosciences, Environment and Spatial Planning, Faculty of Sciences, University of Porto.

Identification	Description	Samples	No. of Measurements
<b>FE-19-01</b>	CXG: sample from Feli mine.	1	4
<b>T7-19-01</b>	CXG: sample from near a T7 vein.	1	3
<b>T7-19-02</b>		1	2
<b>T7-19-04</b>		1	4
<b>ALB-19-01</b>		1	4
<b>ALB-19-02</b>	CXG: samples, collected perpendicular to the T8 vein of Alberto mine.	1	4
<b>ALB-19-03</b>		1	4
<b>ALB-19-04</b>		1	3
<b>ALB-19-05</b>		1	4
<b>ALB-19-06</b>		1	3
<b>T5-19-01a</b>		CXG: sample, collected in the vicinity of a T5 vein.	1
<b>T5-19-01b</b>	Sample of a T5 vein (barren for Li).	1	7
<b>T5-19-02</b>	CXG: sample, collected in the vicinity of a T5 vein.	1	2
<b>T5-19-03</b>		1	3
<b>T5-19-04</b>		1	3
<b>TC-19-02</b>		CXG: sample from a profile with one T6 vein.	1
<b>TC-19-04</b>	1		3
<b>TC-19-07</b>	CXG: sample from a profile with two T6 veins.	1	2
<b>TC-19-08</b>		1	3
<b>TC-19-09</b>		1	4
<b>TC-19-10</b>		1	4
<b>SPB-18</b>	Samples from the stock-pile of Bajoca mine; T7 vein.	2	21
<b>Alberto 1</b>	Samples of petalite, from the T8 vein of Alberto mine.	2	10
<b>Alberto 2</b>	Samples of spodumene + quartz, from the T8 vein of Alberto mine.	1	8
<b>Alberto 3</b>		3	24
<b>Fel-Lep</b>	Lepidolite sample, from the T9 vein of Feli mine.	1	13
<b>ZIN</b>	Zinnwaldite sample (Li mica).	1	13
<b>Bajoca-L</b>	Lepidolite sample, collected within the limits of Bajoca mine.	1	8
<b>Fregeneda</b>	Petalite sample, from La Fregeneda region.	1	5
<b>Massu-Mont</b>	Montebrasite sample (Li phosphate), from Massueime mine.	1	6

The spectral analyzes were performed in the GeoRessources laboratory, at the University of Lorraine, in Nancy, France, during a two-month internship. The electromagnetic spectra measured and treated during the present study were acquired through the use of the spectroradiometer, SR-6500 (Spectral Evolution, Inc.), described ahead in 3.1 sub-chapter.

The samples did not have any treatment prior to the analysis, since that for the present study it is wanted to know the spectral response of the sample in its most natural state, taking care only for the analyzes to be carried out on dry samples, since the high capacity of water for absorption may interfere with measured reflectance values.

Each sample was subjected to a set of measurements, to capture the maximum data from it, thus, for each sample, a set of measurement points was obtained and respectively, also a set of measurement spectra was obtained. The distribution of these points was performed according to the homogeneity/heterogeneity of each sample and to the size of the same, always trying to make the best coverage of the whole sample, in order to have the most representative result. At each measured point, its main characteristics were recorded, noting the face type (exposed; broken; or natural break), the mineral under observation, when possible to identify, the color, and some other observations, such as the presence of iron oxides and vegetation, so that the best interpretation of the results was possible.

### 3.1 SR-6500 Spectroradiometer

The SR-6500 spectroradiometer (Spectral Evolution, Inc.), presented in Figure 7, utilized in this present work for spectral measurement of samples, is a device with the capacity of collecting and storage spectral data, in a wavelength range from 350 nm to 2500 nm (UV-VIS-NIR-SWIR), with high spectral resolution (1,5 nm at 700 nm, 3,0 nm at 1500 nm and 3,8 nm at 2100 nm).



Figure 7 – High-resolution SR-6500 spectroradiometer (Spectral Evolution, Inc.). Optical fiber cable of 1.5 m of length. Image source: [https://www.alphaomega-electronics.com/5506-cart\\_default/sr-6500-espectrofotometro-de-alta-resolucao.jpg](https://www.alphaomega-electronics.com/5506-cart_default/sr-6500-espectrofotometro-de-alta-resolucao.jpg)

SR-6500 is equipped with three spectral detectors, the 1024 element TE-cooled silicon detector, used for the spectral range from 350 nm to 1000 nm (UV-VIS-NIR), the 512 element TE-cooled InGaAs detector, for a spectral range up to 1630 nm (SWIR1), and the 512 element TE-cooled extended InGaAs detector, for a range up to 2500 nm (SWIR2).

The measurements with this device can be carried out through several optional optical instruments (foreoptic), where the connection of these to the device, is accomplished by a 1.5 m length fiber optic cable (Figure 7), which will have associated noise. This noise is measured in equivalence to radiance (Noise Equivalence Radiance), being  $0.8 \times 10^{-9} \text{ W/cm}^2/\text{nm}/\text{sr}$  at 400 nm,  $0.3 \times 10^{-9} \text{ W/cm}^2/\text{nm}/\text{sr}$  at 1500 nm and  $5.8 \times 10^{-9} \text{ W/cm}^2/\text{nm}/\text{sr}$  at 2100 nm.

The data acquisition and configuration of measurement parameters are controlled by the DARWin SP software (Spectral Evolution, Inc.), running on a separate computer. It also enables a first processing of the data. On the other hand, all synchronization of data acquisition and readings from the detectors are in charge of the microprocessor present in the device system.

During the analysis, by triggering over a target area, the instrument will receive the reflected light converting it to current, stored as ASCII characters and binary values readable by the software, which graphically displays them as a spectrum. The spectrum data is then saved into .SED files, with the reflectance percentages (0-100%) and the correspondent wavelength, as well as metadata of the associated measurement conditions.

Two measurement modes are available with this spectroradiometer: on one hand, a radiance mode which uses the sun as light source and requires measurements at a distance from the sample; and on the other hand, a reflectance mode, which is done with contact to the sample and requires an extra light source. The latter mode was chosen in order to avoid influence from the atmosphere and to analyze as small areas as possible. The Handheld Contact Probe (HCP) presented in Figure 8, is the optical instrument required for the reflectance mode. The HCP has a halogen lamp (4.25 V, 1.06 A) allowing a study in a controlled lighting environment. HCP receives electrical energy from the device through a power cable. The reflectance reading results from the transportation of the reflected light by the object in study, through the optical cable, connected to the HCP at an angle of  $10^\circ$ , to the instrument. Each measurement point performed with the HCP represents a 10 mm diameter circle. For a more precise reading, the manufacturer advises for a measurement with the HCP in a position as perpendicular to the object surface as possible.



Figure 8 - Handheld Contact Probe, optical instrument. Image source: SR-6500 Operator's Manual.

### 3.1.1 Operating Mode

Before starting measuring, the SR-6500 spectroradiometer requires some previous procedures, such as the connection to the software and specifying the measuring type. With this, the instrument will be warming for 15-20 minutes, where during this time the software will collect several operational parameters and calibration data, from the device. After the warmup, it is necessary to take a measurement of a white reference plate, to obtain a standard reference for reflectance, from which the software will calibrate the following measurements, thus, Spectralon reflectance standard (from Labsphere) was used. This Spectralon has over 95% of reflectance in the wavelengths between 250 nm and 2500 nm.

The Averages option from the DARWin SP software allows each measurement to actually be the average of a defined number of analyses. In this study, each spectrum exported by DARWin SP was the average of 40 individual spectra, reducing the possibility of errors and the occurrence of noise. *Integration* (ms) represents the aperture time for each detector, where the *Auto Integration* option was selected, allowing the software to specify the values needed for the best spectral resolution.

Figure 9 exemplifies the assembly scheme necessary for working with the SR-6500 spectroradiometer.



Figure 9 - Assembly scheme for the SR-6500 spectroradiometer. From left to right is possible to observe the spectroradiometer (on the left) connected to the Handheld Contact Probe (in the center) and (on the right) the computer to which the device is also connected, where a scene of DARWin SP is observed.

## 4. Results

The results were processed with the Spectragryph software (The Spectroscopy Ninja) (Menges, 2020), where the analyses to all collected electromagnetic spectra were performed, as well as the comparison with the reference spectra from the spectral libraries of USGS (Kokaly et al., 2017) and ECOSTRESS (Baldrige et al., 2009).

A Python application, named Pysptools (Therien, 2020), was used for the continuum removal (hull quotient), which is a method of normalizing a reflectance spectrum, allowing an easier identification, and understanding of the absorption features implicit in the spectrum. These absorption features appear in the spectrum as troughs and correspond to zones of the wavelength where the energy, in the form of light, is absorbed due to specific molecular bonds of the target material (Binotto et al., 2015). For the analysis of a determined absorption feature, it is important to identify and register the position and depth of the feature, being thus able to classify specific mineralogy. The depth corresponds to the value of absorption associated with the feature. In the case of the present work, this value is presented in percentage of absorption, obtained by subtracting the reflectance percentage, to the absolute reflectance (100%).

### 4.1 Lithium Minerals

The results presented below, are intended to describe the main spectral characteristics of the Li minerals studied. For a better understanding, the continuum removed spectrum was sliced into four portions, capturing the main features of the spectrum, where, to respect them, these portions were taken at a different range of wavelengths, making sure that no feature would be sliced.

#### 4.1.1 Petalite

The study of the spectral signature of petalite was based on twelve measurement points, performed on areas of the sample where petalite minerals were identified, being these from four different sampling locations. In Table 3, it is possible to find the description of these points used in the petalite signature spectrum generation. In Table 3 it is also listed the identification of the sampling location and the type of aplite-

pegmatite vein to which it belongs. The vein type of the Fregeneda sample was not possible to correctly identify since its precise sampling location is not known.

The beginning of the study of the spectral signature of the minerals of petalite, started by stacking all the spectra measured in a graphic form, as presented in Figure 10. With the analysis of this graphic, it is possible to get an idea of the tendency that the spectral signature of petalite will have, with the presence of three peaks of absorption. Comparing all the spectra presented in Figure 10, it is noticeable some slight differences, wherein four of these spectra the differences are more accentuated.

Table 3 – Identification of the measurement points used in the elaboration of the spectral signature of petalite. Description of the sampling location, vein type and measurement point.

<b>Sampling</b>	<b>Vein</b>	<b>Measurement Point</b>
448	T7	13_03_00072
		13_03_00073
449	T7	13_03_00127
		13_03_00131
Alberto-1	T8	13_03_00089
		13_03_00091
		13_03_00092
		13_03_00095
Fregeneda	Unknown	13_03_00100
		13_03_00101
		13_03_00102
		13_03_00103

The spectra identified as 13\_03\_00072 and 13\_03\_00073 presented in Figure 10, shows the existence of an absorption zone between 750 nm and 1280 nm, being this different from the behavior of the other spectra. Inside this zone, it is visible the slight accentuation of absorption resulting in the presence of two absorption peaks, at 964 nm and 1153 nm. In the remaining wavelengths is observed the same trend as the other spectra studied. The Figure 11 presents the minerals of petalite which have produced these spectra, appearing with a dark to greenish tone, showing signs of alteration. The presence of alteration minerals in the measurement spots, might be inducing spectral responses in the obtained spectrum, resulting in different features from the observed in minerals with no alteration.

The 13\_03\_00127 and 13\_03\_00131 spectra represented in Figure 10, shows a high similarity trend to the remaining spectra, with a slight decrease in the reflectance in the higher wavelengths. However, the identification of the absolute peaks of absorption is difficult. The first peak is still possible to detect, despite being tenuous, but for the two others, it is practically impossible. This might be related to the fact that these two spectra were produced by a sample of small dimension (Figure 12), not being able to correctly put on the probe and for that allowing to part of the energy from the instrument to escape.

Therefore, to elaborate the spectral signature of petalite, the mentioned above spectra were removed. The spectral signature of petalite was accomplished using the arithmetic average of the remaining eight measured spectra, resulting in the spectrum presented in Figure 13.

The spectral signature of petalite (Figure 13), starts with a strong increase in the percentage of reflectance, going from 24% to 46.5%. In the remaining spectrum, the percentage of reflectance suffers a successive decrease, getting to values of around 25% at the end of the spectrum (2500 nm). Observing the spectrum, it is notable for the presence of three absolute absorption peaks, situated at 1413 nm, 1910 nm, and 2206 nm.

The removal of the spectrum continuum (Figure 14), enable a more detailed study of the zones where is identifiable the absorption of energy, allowing to not only a better understanding to the already detected absolute absorption peaks but also to determine relative absorption peaks of smaller expression in the spectrum.

The first portion obtained from the removed continuum comes up between 800 nm and 1250 nm (Figure 15 (A)). It is observed the effect of absorption throughout the spectrum, which can be related with the absorption found in the 13\_03\_00072 and 13\_03\_00073 spectra, meanwhile removed from these analyses, where these two presented an absorption much more accentuated, with higher absorption percentages. The emergence of this absorption zone may be produced by the presence of three small peaks, hardly noticeable without the removal of the continuum. At the wavelength of 907 nm, it is observed the first peak with 1.5% of absorption, the second comes up at 963 nm with 2% absorption and finally, the third peak is found at 1159 nm with 1.3% absorption.

The second portion was taken between 1300 nm and 1600 nm, in a zone of absorption which was already detected in the spectrum of the signature of petalite (Figure 15 (B)). This portion is marked by the presence of a single absorption peak of 18.1%, where this maximum is reached at the wavelength of 1413 nm. Observing this

zone, it is noticeable a rapid increase of absorption until it gets to the minimum reflectance for then the decrease to be done in two phases. Firstly, the decrease of absorption is as rapid as the increase, starting then to diminish the rhythm of decreasing, ending up stagnating between the wavelengths of 1453 nm and 1466 nm, keeping a constant reflectance of 89.1%. The second phase of the decrease of absorption starts after 1466 nm, with a slightly slower pace than the last.

The third portion appears between 1840 nm and 2240 nm, presented in Figure 15 (C), and it is marked by the presence of two absorption peaks. Where the first manifests by a rapid ascent of the percentage of absorption, getting to a maximum of 32.6% at the wavelength of 1910 nm. Right after reaching the maximum percentage, the absorption starts to decrease rapidly. However, this decrease is slower than the initial increase, being interrupted by a new increase of absorption originating the second peak observed. This second peak comes up with a smaller percentage of absorption, of 11% at 2206 nm.

The last portion taken from petalite removed continuum spectrum happened between 2240 nm and 2500 nm (Figure 15 (D)). This portion presented two absorption zones, marked by two troughs in the spectrum. Due to the low percentages of absorption and because this is at the ending part of the spectrum, the layout has some irregularity associated, being difficult to find the maximum of absorption in both zones. The first zone has its close maximum in the 2353 nm and the second in the 2442 nm, being this last with higher absorption, where this absorption is no more than 2.3%.

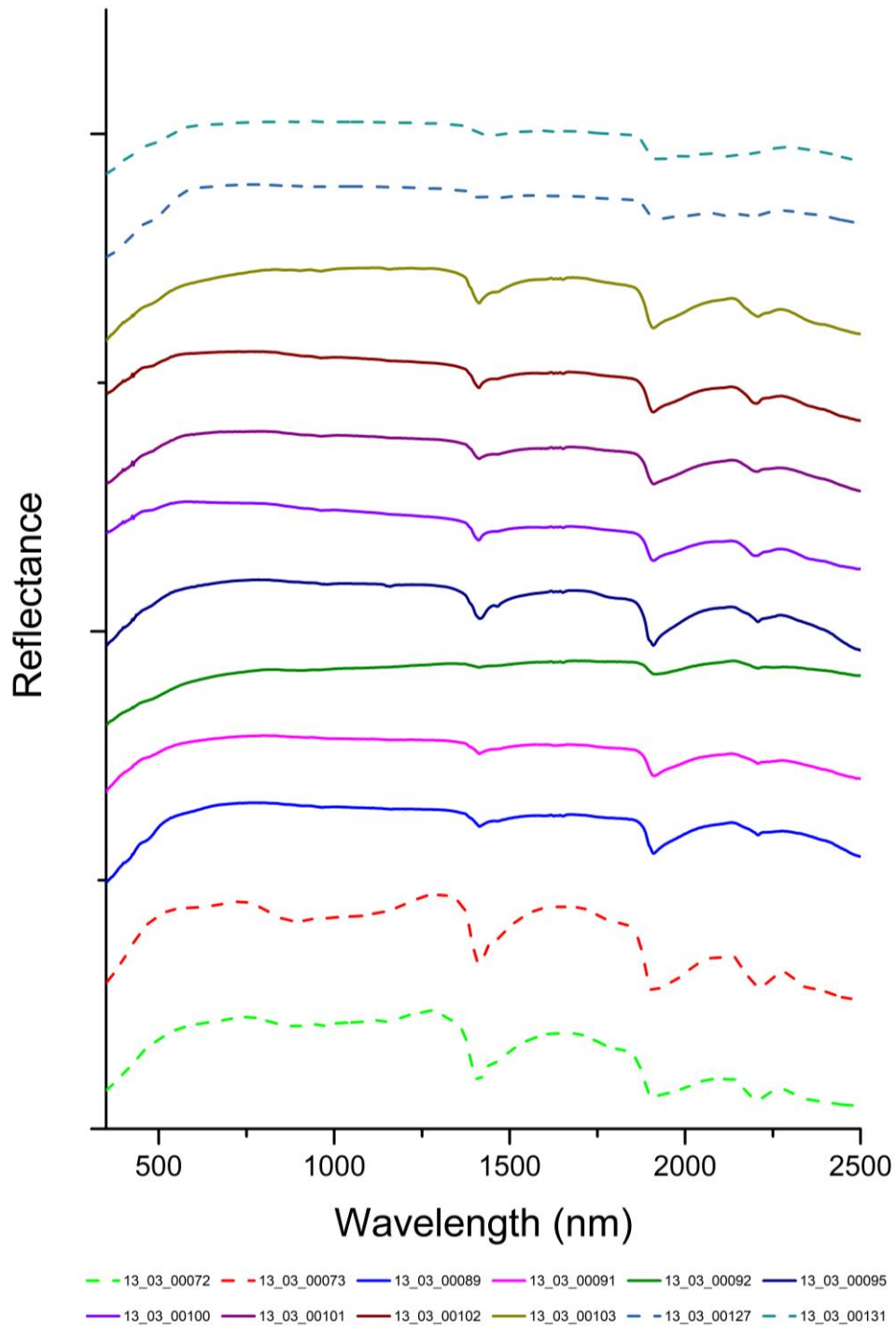


Figure 10 - Graphic representation of the twelve electromagnetic spectra obtained from the study of petalite minerals. The spectra shown with dashed line were removed from the elaboration of the spectral signature of petalite.



Figure 11 - Sample of the aplite-pegmatite vein of Bajoca mine T7 (448). The red circles represent the location where the measurement points were taken. In the left is find the point 13\_03\_00072 and in the right is find the point 13\_03\_00073. In both images inside the circle is observed a petalite mineral with visible alteration, marked by the dark to greenish tones.



Figure 12 - Small samples of petalite (449), collected in the aplite-pegmatite vein of Bajoca mine T7. In the left is represented the sample and face where measurement point 13\_03\_00127 was taken and in the right is represented the sample and face where measurement point 13\_03\_00131 was taken.

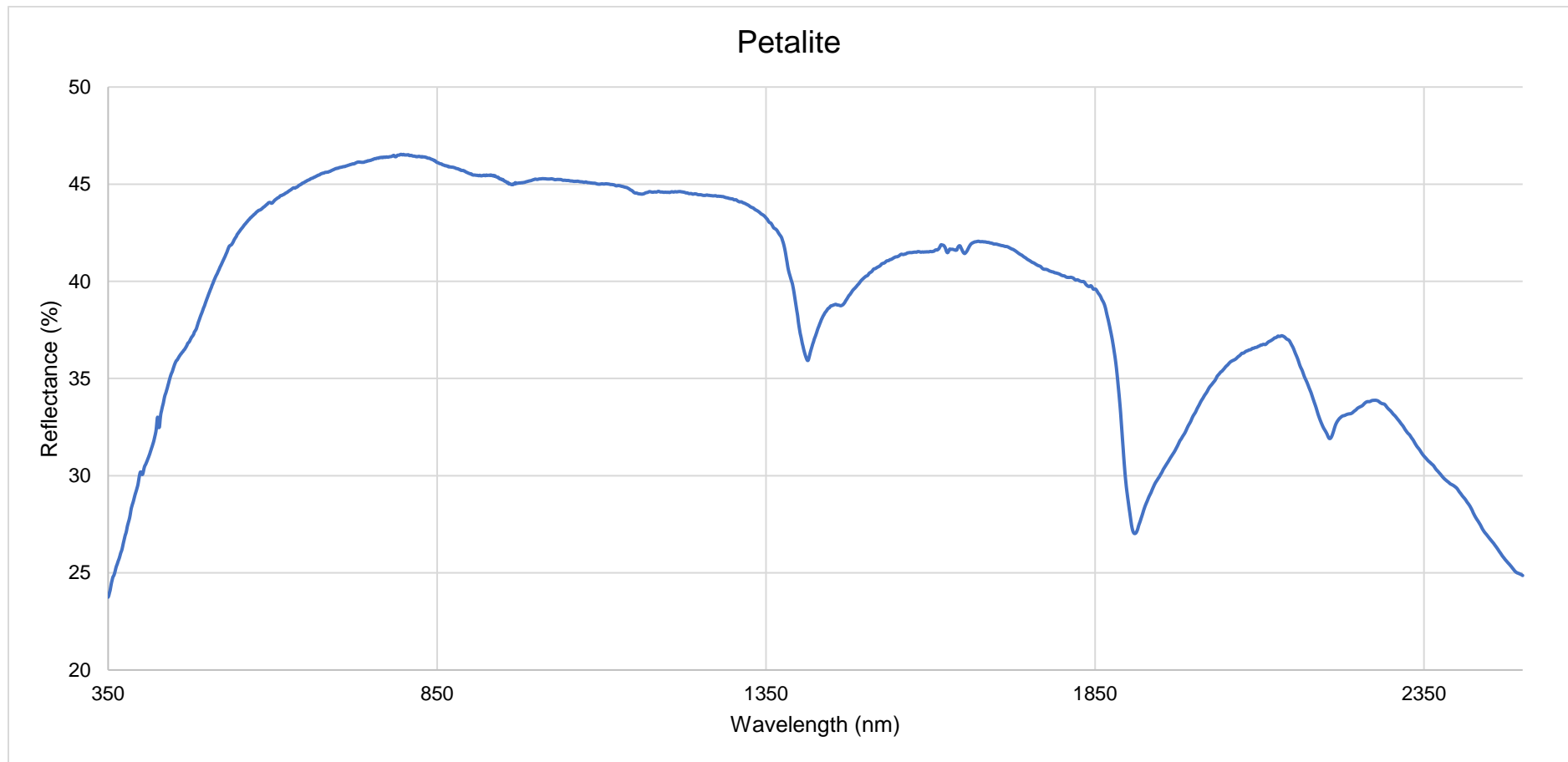


Figure 13 - Spectral signature of petalite. Obtained from the average of the spectra measure in the several petalite minerals studied.

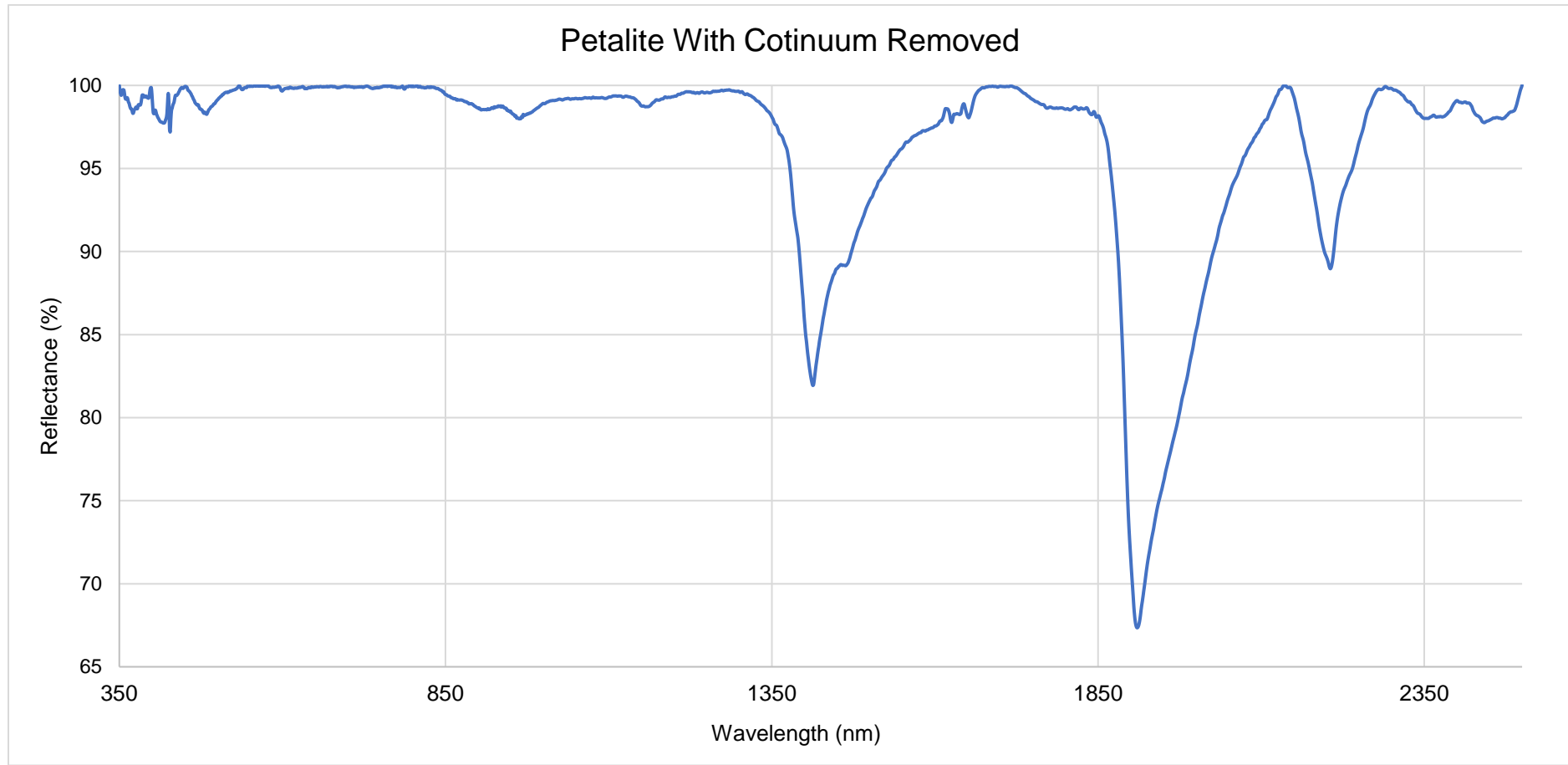


Figure 14 - Spectral signature of petalite with the continuum removed.

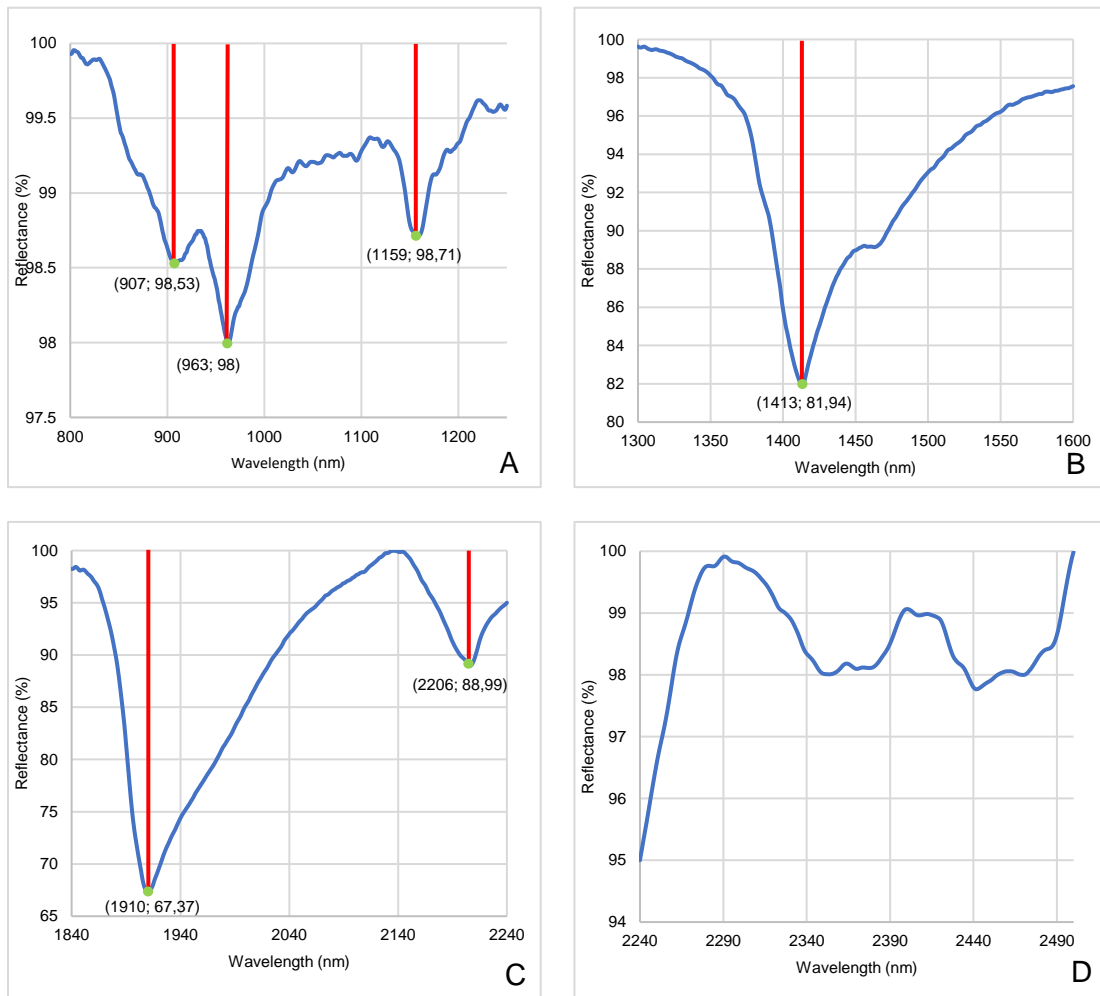


Figure 15 - Portions of wavelength, where is observed the absorption of energy. (A, B, C, D) portions obtained from the slicing of the spectrum of petalite with the continuum removed. The red vertical lines correspond to the maximum absorption, in a determine peak of absorption.

### 4.1.2 Lepidolite

The study of lepidolite spectral signature was performed considering nine measurement points, collected in samples where lepidolite was recognized. In Table 4, it is possible to find the identification of the measurement points and the sample to which belong, as well as the vein type. In the case of Fel-Lep (Figure 16) corresponds to a sample collected in an aplite-pegmatite vein T9 from Feli mine. For Bajoca-L (Figure 17) it was not possible to identify the vein type with certainty, however, with the observation of the map of the aplite-pegmatite veins in the Fregeneda-Almendra aplite-pegmatite field (Figure 3) is possible to set a correspondence to a T10 vein. Once these samples were not collected by the author of the present study, there is a lack of information about them.

Table 4 - Identification of the measurement points, used in the elaboration of the spectral signature of lepidolite. Description of the sample and vein type to which measurement point belong.

Sample	Vein	Measurement Point
Fel-Lep	T9	13_03_00266
		13_03_00267
		13_03_00268
		13_03_00271
		13_03_00272
		13_03_00275
Bajoca-L	Unknown	13_03_00132
		13_03_00134
		13_03_00136

Observing the graphic from Figure 18, where are stacked all the nine spectra used in the elaboration of the spectral signature of lepidolite, it is noticeable a great variety on the trends from the different spectra. Some show a tendency in a shape of a parabola, starting in lower percentages of reflectance and increasing to higher percentages reaching the maximum around the middle of the wavelength (~1610 nm), decreasing then to percentages similar to the starting ones. The other spectra show a tendency that starts with a rapid increase to stabilize in higher reflectance percentages, starting to decrease only on the last third of the spectrum.

The peaks of absorption have also some differences between the spectra, where in some cases it is possible to detect a great number of peaks and in the others, this number is lower, although is still identifiable some small tendencies to have the same number of peaks. This might be related to the fact that the minerals of lepidolite studied

are of small dimension, allowing that other minerals presented in the samples contribute to the spectrum produced, and then resulting in several peaks, once the measurement probe as a 10 mm measuring diameter, much bigger than the size of lepidolite minerals.

Considering the arithmetic average of the nine spectra used to elaborate the spectral signature of lepidolite (Figure 19) it is noticeable that the parabola shape tendency is the one which prevails. The spectrum starts at a percentage of reflectance of 24.5% and keeps increasing towards the middle of the wavelength (~1610 nm), where it reaches the maximum of 41.7% of reflectance. In the second part of the spectrum (~1610 nm to 2500 nm) the percentages of reflectance start to decrease, completing the parabola shape and getting at the end in percentages of 18.3%.

The observation of the spectral signature of lepidolite (Figure 19) is marked by the presence of three absolute peaks of absorption, with different percentages, which interferes with the overall shape of the spectrum. The first peak observed occurs at 1410 nm, the second appears with lower absorption percentages at 1905 nm and the third, at 2196 nm, is the one with of higher depth meaning a greater absorption percentage.

The study of the continuum removed spectrum of lepidolite allowed to better understand the existence of these absolute peaks (Figure 20). Just by observing it is possible to notice that the number of peaks presented by the signature of lepidolite is higher than what was described, with the presence of several absorption peaks of smaller expression. The first portion, presented in Figure 21 (A), from 400 nm to 1270 nm, is characterized by low percentages of absorption, although it is possible to identify three peaks of absorption. The first peak occurs in the green band from the VIS, at 566 nm with 5.7% of absorption, being a typical peak of lepidolite signature, related with the purple color that characterize this mineral. With maximum percentage of absorption at the wavelength of 860 nm a zone of absorption is followed, which together with the nearby peaks seems to decrease the percentage of reflectance, originating a higher absorption zone, that persists until the wavelength of 1270 nm. The second peak comes up at 963 nm with 4.5% of absorption. Before the third peak, it is noticeable the traces of other peak, with low expression, at 1151 nm. The third is presented at 1246 nm with 0.8% of absorption.

The second portion, presented in Figure 21 (B), is comprised between 1270 nm and 1700 nm and is only possible to identify one single peak at the wavelength of 1410 nm with 35.4% of absorption. The increase of absorption for this peak is high, as well as the decrease.

The third portion, as shown in Figure 21 (C), goes from 1860 nm to 2280 nm and is marked by the presence of two main peaks of absorption. The first peak is detected at 1905 nm with 22% absorption. The increase of absorption is fast, and the decrease is made in two phases, once the decrease is interrupted between 1983 nm and 1994 nm, where is visible a slight increase in the absorption, getting to decrease right away. At the wavelength of 2114 nm a peak is identified with 7.1% of absorption, which is very small when compared with the two main absolute peaks observed in this portion, but significative when compared with the peaks described in the first portion. Right after this zone comes up the second peak at 2196 nm and with 37.1% of absorption.

Finally, the fourth portion (Figure 21 (D)) ranges between 2280 nm and 2500 nm and can be interpreted as a single absorption zone that covers all this portion and it is related to the presence of two absorption peaks. The first at 2346 nm, with absorption of 16.2% and the second at 2432, with 13.4%.



Figure 16 - Fel-Lep sample. Aplite-pegmatite vein T9 from Feli mine. Lepidolite is represented by the crystals in purple tones.



Figure 17 - Bajoca-L sample. Sample of aplite-pegmatite vein with lepidolite, represented by the purple hued minerals.

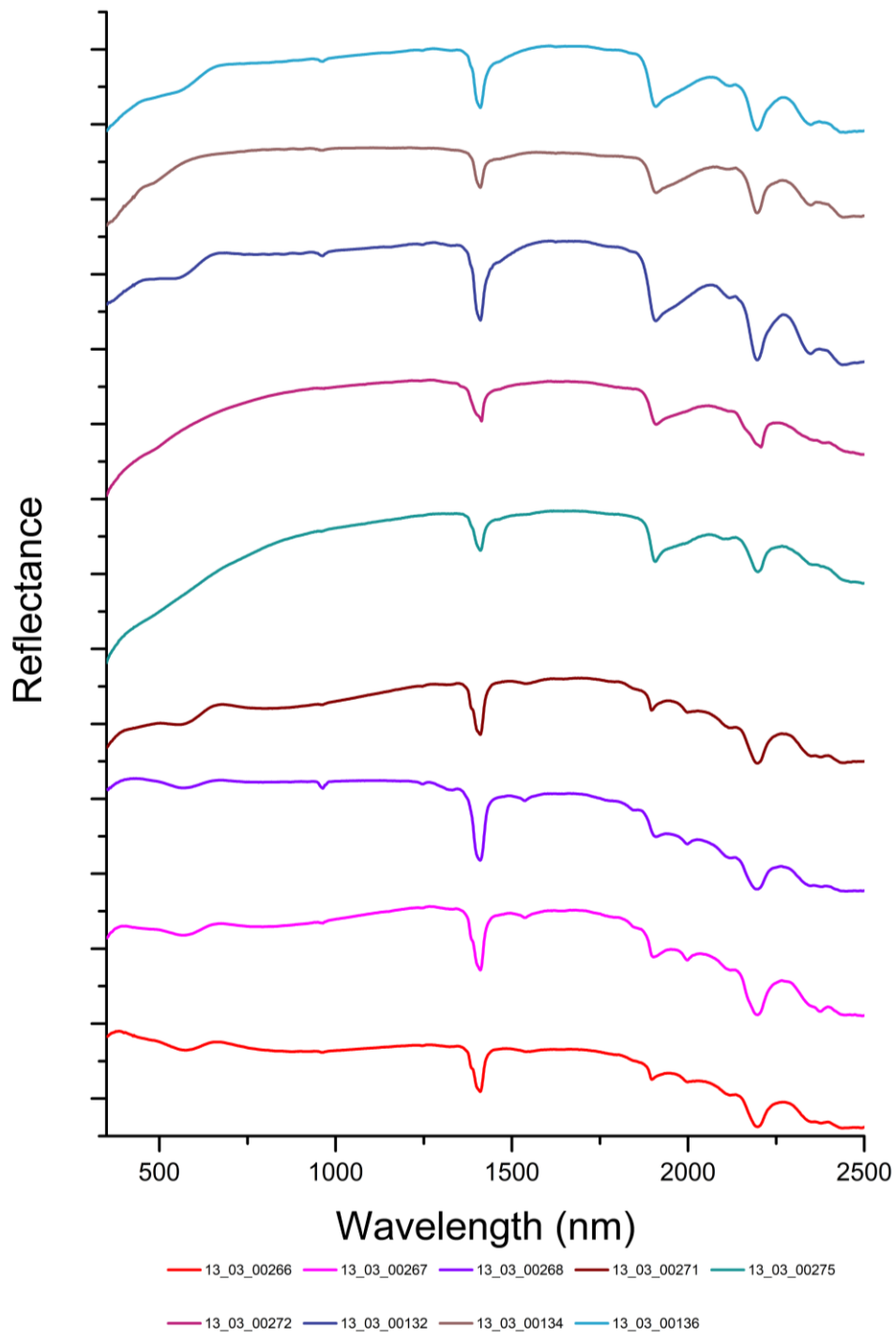


Figure 18 - Graphic representation of the nine electromagnetic spectra obtained from the study of lepidolite minerals.

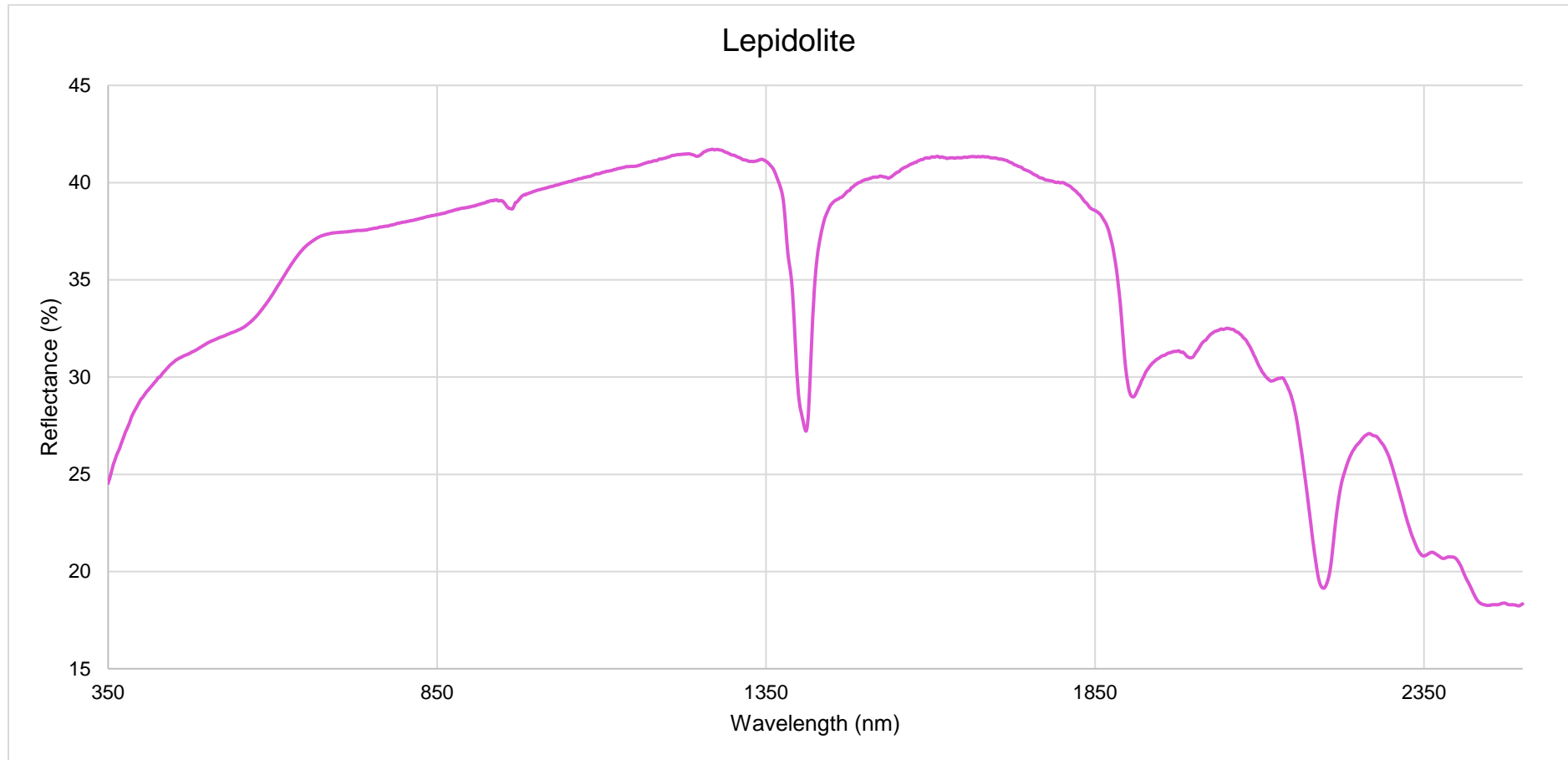


Figure 19 - Spectral signature of lepidolite. Obtained from the average of the spectra measure in the several lepidolite minerals studied.

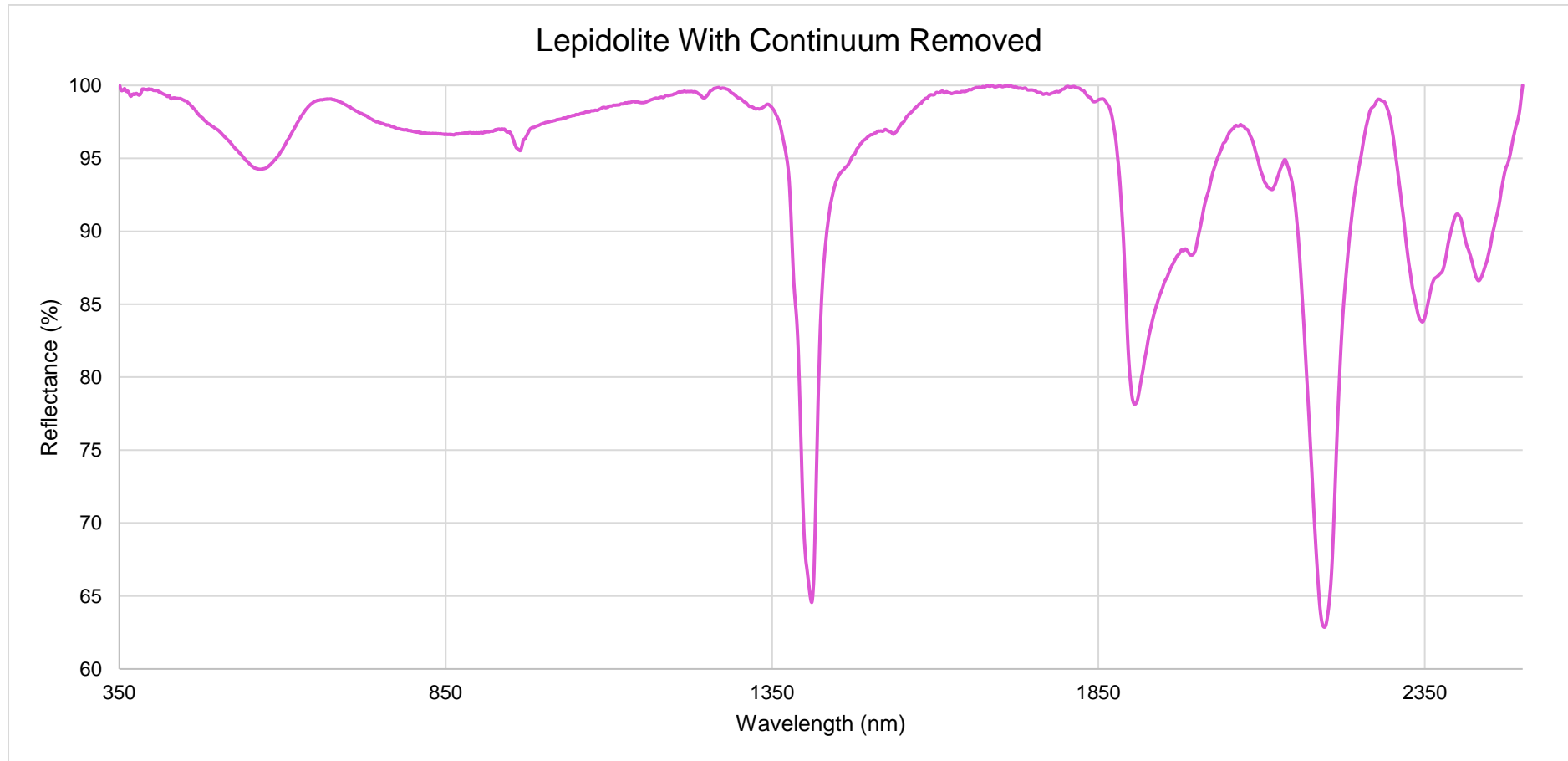


Figure 20 - Spectral signature of lepidolite with the continuum removed.

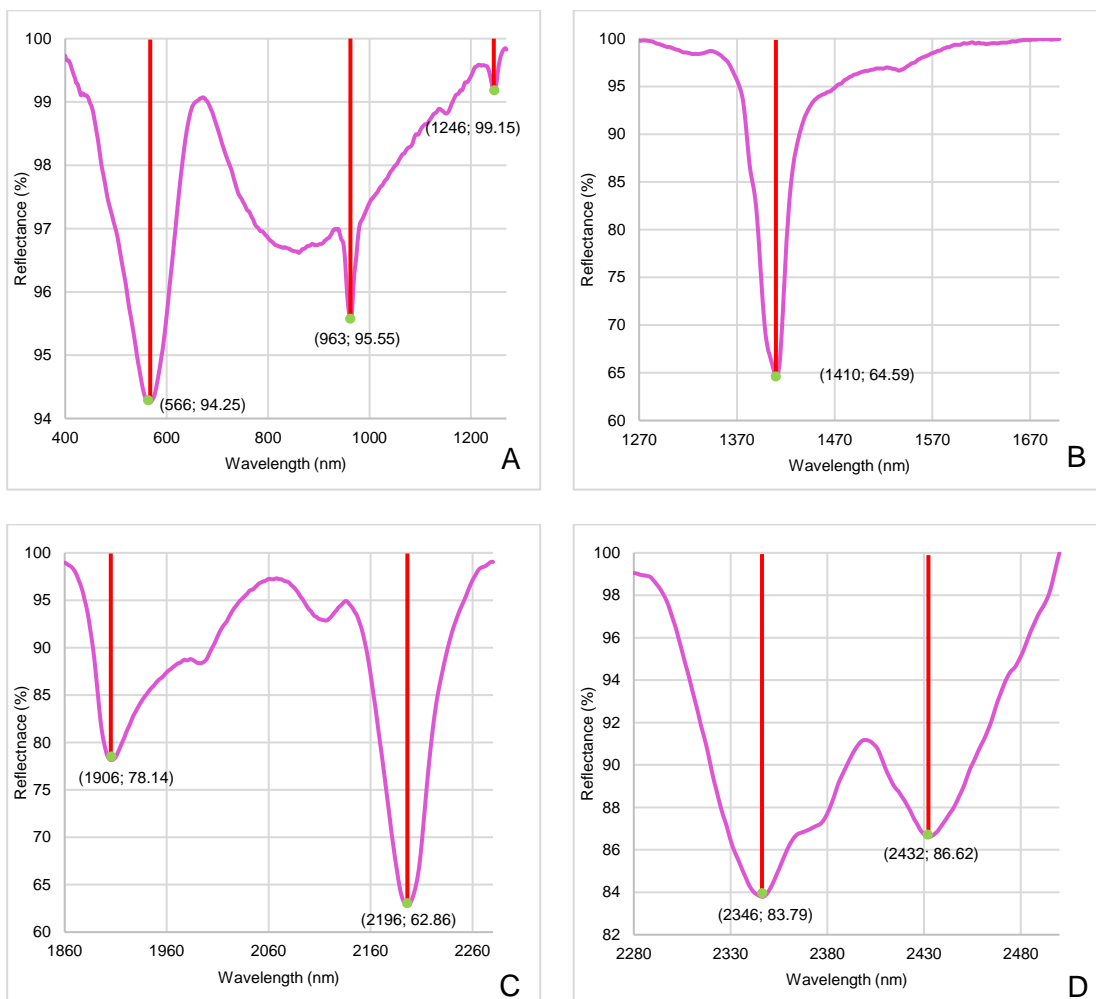


Figure 21 - The four portions of wavelength used for the study of absorption zones in the spectral signature of lepidolite. The spectrum presented has the continuum removed. The red vertical lines represent the depth caused by the effect of absorption. The length of the red line is the percentage of absorption.

### 4.1.3 Spodumene

The study of spodumene was only accomplished with the samples from the Alberto mine, a T8 aplite-pegmatite vein. As mentioned before, this type of vein has spodumene associated with petalite, where spodumene can be in intergrowing with quartz, forming the SQUI type structures. In the current work, it will be firstly present the elaboration and analyses to the spectral signature of spodumene obtained with the measurement points where was only identified spodumene, without quartz association (Table 5, Figure 22). After it will be shown a comparison between the signature of spodumene, without quartz association, and the signature produced by the SQUI structure. The measurement points used for the elaboration of the spectral signature of SQUI, are presented in Table 6, and in Figure 23 is possible to observe the aspect of the sample studied.

Observing the graphic of Figure 24, accomplished with the spectra from the measurement points of Table 5, these points corresponding to measures done in spodumene minerals. It is noticeable a great similarity between all spectra, showing identical tendencies. The percentages of reflectance have some variety, being the maximum close to 41% in the spectrum with the lowest percentages, and 82% in the spectrum with the highest percentages.

Table 5 - Identification of the measurement points, used in the elaboration of the spectral signature of spodumene. Description of the sample location and vein type. Study of spodumene without quartz association.

Sample	Vein	Measurement Point
Alberto-3	T8	ALB3_00004
		ALB3_00005
		ALB3_00006
		ALB3_00010
		ALB3_00012
		ALB3_00013
		ALB3_00014
		ALB3_00015

Table 6 - Identification of the measurement points, used in the elaboration of the spectral signature of the SQUI structure (spodumene + quartz). Description of the sample location and vein type.

Sample	Vein	Measurement Point
Alberto-2	T8	13_03_00115
		13_03_00116
		13_03_00117
		13_03_00118
		13_03_00119
		13_03_00120
		13_03_00121
		13_03_00122
Alberto-3	T8	ALB3_00001
		ALB3_00002
		ALB3_00003
		ALB3_00011
		ALB3_00016
		ALB3_00018
		ALB3_00019
		ALB3_00020
		ALB3_00021

Analyzing the spectral signature of spodumene, presented in Figure 25, obtained by the arithmetic average of the spectra measured in minerals of spodumene without quartz associated, it is possible to identify the presence of three absolute peaks of absorption, at the wavelengths of 1412 nm, 1910 nm, and 2206 nm. The tendency of the spectrum shows an initial high increase of the reflectance percentage, towards the highest values found in this spectrum, going from percentages of 29% to 62%, where it stabilizes for the wavelengths between 790 nm and 1280 nm. During this stability period, it is detectable the presence of two small peaks of absorption, detailed below, in the first portion of the spectrum with the continuum removed. With the first absolute peak observed, the spectrum starts to show a tendency of decreasing the reflectance percentage, at a much slower rate than the initial increase, ending with a percentage similar to the one that begins with, a little over 30%.

The resource to the spodumene spectral signature with the continuum removed, presented in Figure 26, shows an initial zone where is understandable the effects of absorption in the spectrum, going from 350 nm to 660 nm, which can be correlated with some resistance to the initial increase of reflectance, detected in the graphic with the spectral signature of spodumene (Figure 25). As happened before, this spectrum with the continuum removed was also cut into four portions, to have a better perspective of the areas where is found absorption in the spectrum.

The first portion was taken between 775 nm and 1280 nm, as shown in Figure 27 (A), wherein similarity with what was detailed to the others Li minerals, it is possible to identify a zone of absorption that affects all of these wavelengths, being marked and possibly promoted by the presence of two absorption peaks. Around the wavelength of 883 nm is noticeable in a zone where absorption is trending, producing a round shape on the spectrum. This zone ends with the appearance of the first absorption peak, with 2.1% of absorption maximum, at 965 nm. For this peak, the absorption rapidly increases until reaching the maximum percentage, for then decrease rapidly, in a small first part, till it gets to a zone where is going to increase slightly, getting back to decreasing rapidly again. The second peak comes up at the wavelength of 1157 nm with 1.5% of absorption. Throughout this portion of the spectrum is noticeable some noise, resulting in an irregular layout, yet this does not seem to interfere in the normal tendency of the spectrum.

The second portion of the spectrum was taken between 1280 nm and 1700 nm (Figure 27 (B)). This portion is marked by the presence of just one absorption peak, at the wavelength of 1412 nm, with absorption of 27.2%. The increase of absorption in this peak happens rapidly and the decrease is done into phases, similar to what has been happening before: firstly, the decrease is accentuated, ending up stabilizing after, until getting back to decreasing at a lower rate. Between the wavelengths of 1610 nm and 1660 nm is observed a zone where the percentages are unstable, showing the presence of noise, something that is also possible to observe in the spectral signature of petalite in Figure 13.

The third portion of the spectrum is compressed between the 1840 nm and the 2290 nm, as shown in Figure 27 (C). In this portion is detected the presence of two absorption peaks, where they are noticeable very symmetrical and with high sharpness. The first peak comes up at 1910 nm with 37.9% of absorption and the second at 2206 nm with 20.1% of absorption.

For the last part of the spectrum, a fourth portion was taken between 2290 nm and 2500 nm (Figure 27 (D)), at the end of the spectrum. In this portion is possible to observe the presence of two small absorption peaks, where the wavelength of 2346 nm marks the first peak with 5.7% of absorption and 2437 nm marks the second with 4.1%. These absorptions are almost impossible to identify without the continuum removed spectrum.

The same procedure was made for the elaboration of the spectral signature of the SQUI structure, having to use the measurement points indicated in Table 6, except for the points labeled with 13\_03\_00120, 13\_03\_00121, and 13\_03\_00122, due to the

high differences in the values presented, possibly related with the bad surfaces of the samples where the points have been measured, being irregulars and with great evidence of exposure to the elements.

The SQUI spectral signature is presented in Figure 28, where is also possible to observe the representation of the obtained signature for spodumene, allowing to compare both. This analysis does not allow to make any distinctive difference, arising both with the same three distinctive absorption peaks, at 1412 nm, 1910 nm, and 2206 nm, even the very small peaks detected at the beginning of the NIR zone, between 775 nm and 1280 nm, are possible to identify. The only main difference possible to point out is the fact that the signature of spodumene starts at a lower reflectance and rapidly increases to a reflectance of about 12% higher than the signature of SQUI. This might be happening due to the presence of residual petalite, once this intergrowing happen in the crystals of petalite, in the result of the alteration of this last. Observing the spectral signature of petalite, in Figure 13, the reflectance is similar to the one found in the signature of the SQUI structure. Also, the presence of quartz might be interfering with the purity of spodumene diminishing the reflectance.



Figure 22 - Sample from Alberto-3. Aplite-pegmatite vein T8 from Alberto mine. Inside the red circle is observed a mineral of spodumene, where the measurement point ALB3\_00004 was taken.



Figure 23 - Sample from Alberto-3. Aplite-pegmatite vein T8 from Alberto mine. Sample with SQUI, where is the presence of spodumene, in a with color, and quartz, in a more translucent tone.

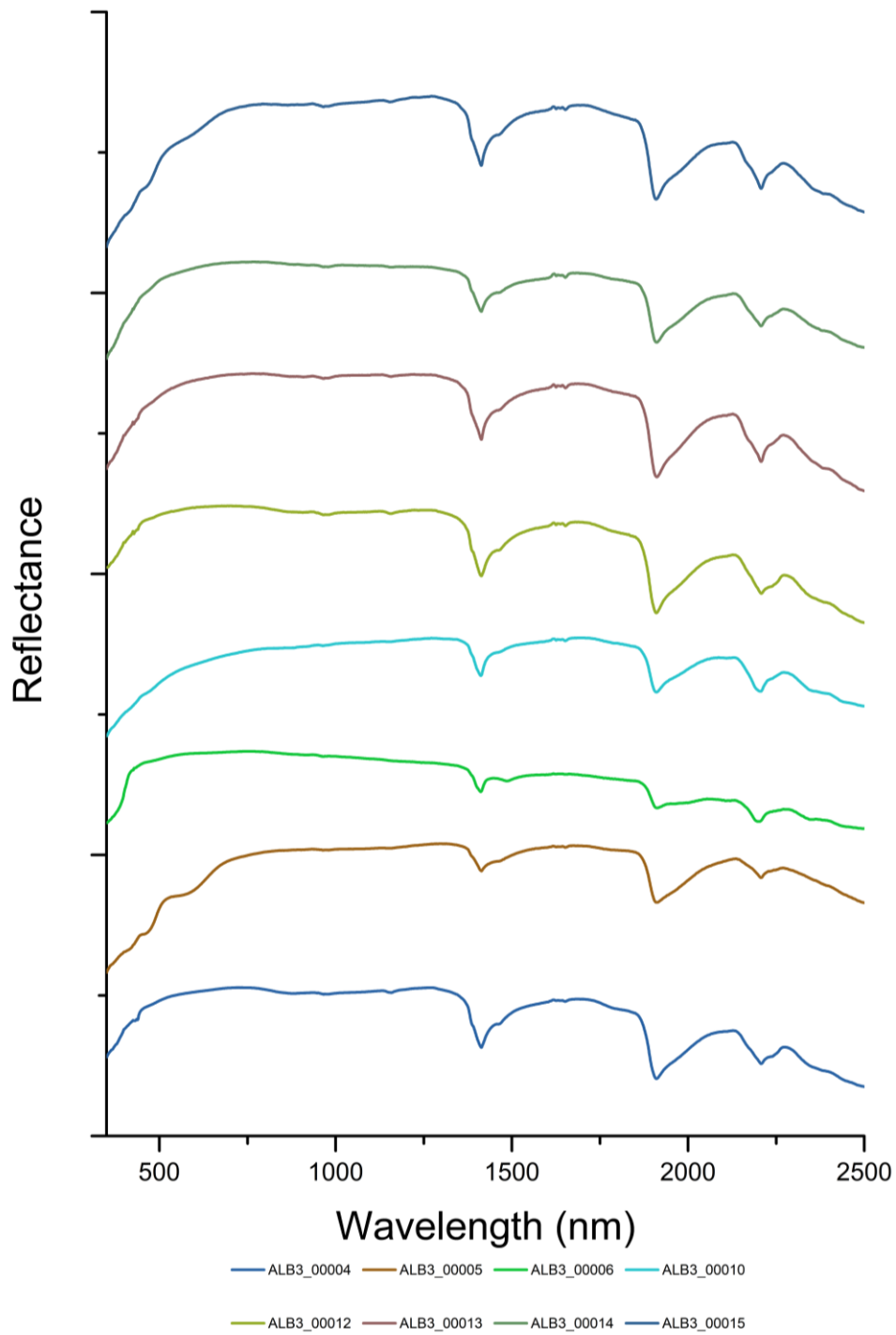


Figure 24 - Graphic representation of the eight electromagnetic spectra obtained from the study of spodumene minerals, without quartz association.

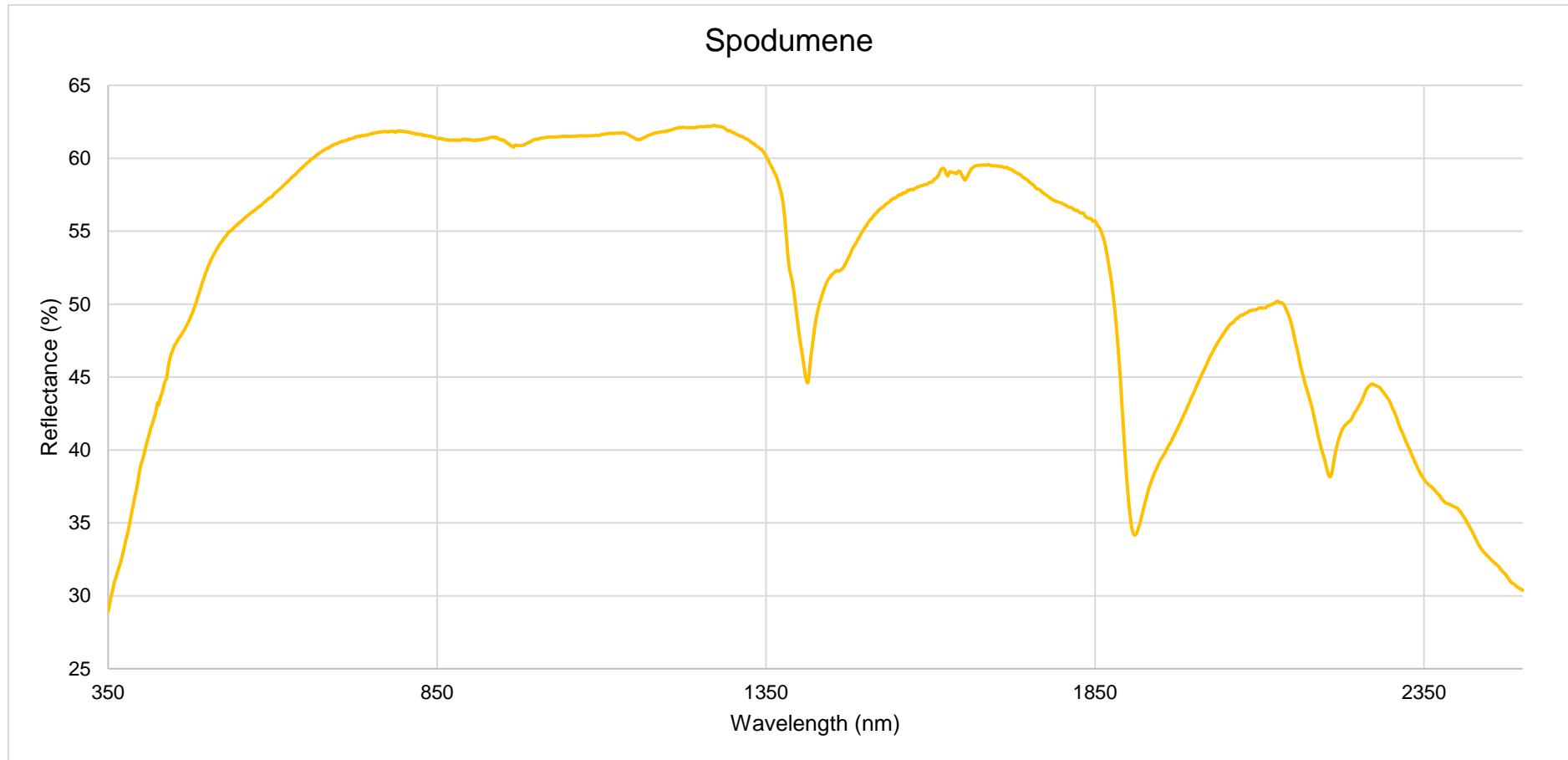


Figure 25 - Spectral Signature of spodumene. Obtained from the average of the spectra measure in the several spodumene minerals studied, without quartz association.

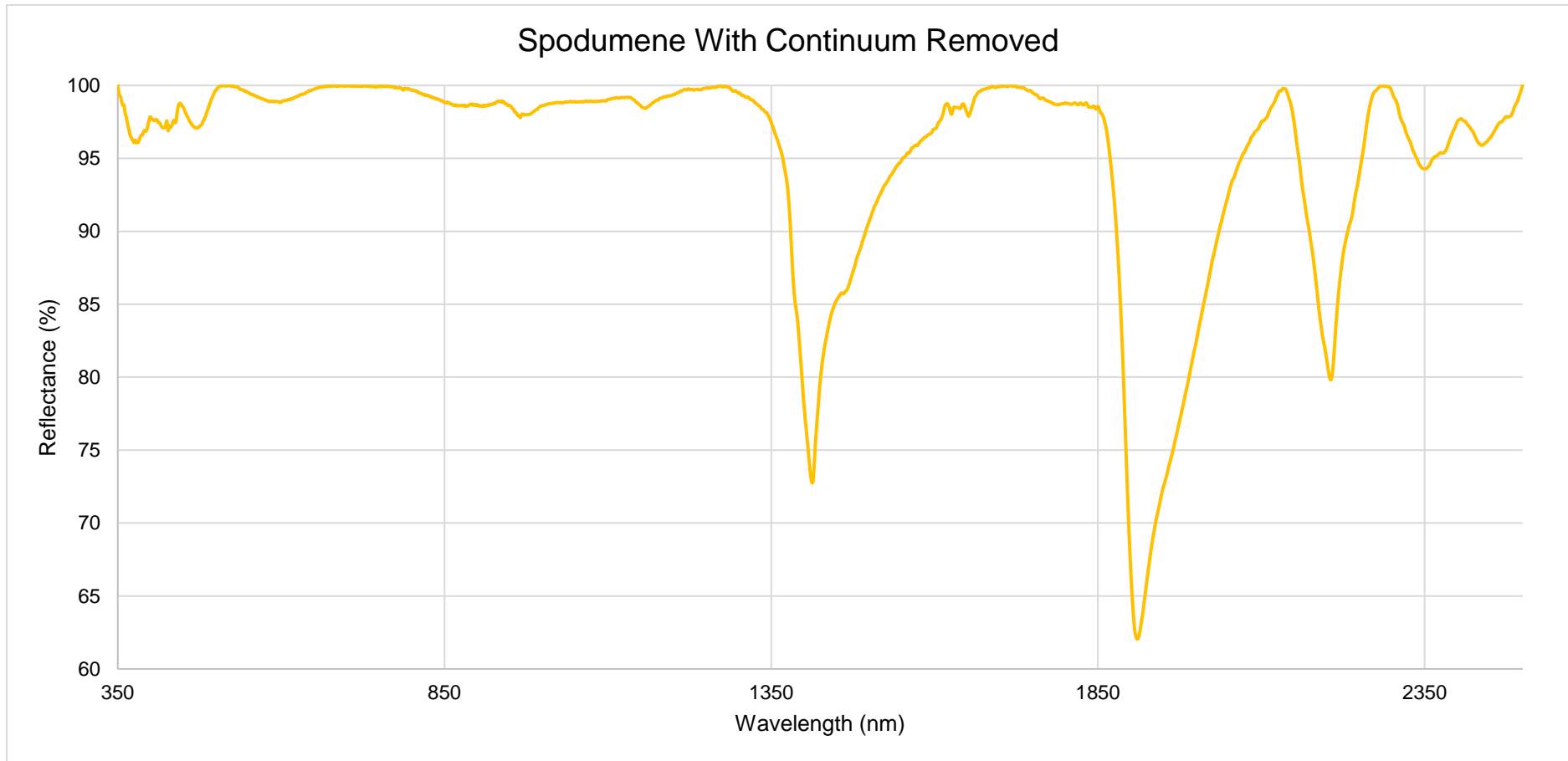


Figure 26 - Spectral signature of spodumene with the continuum removed.

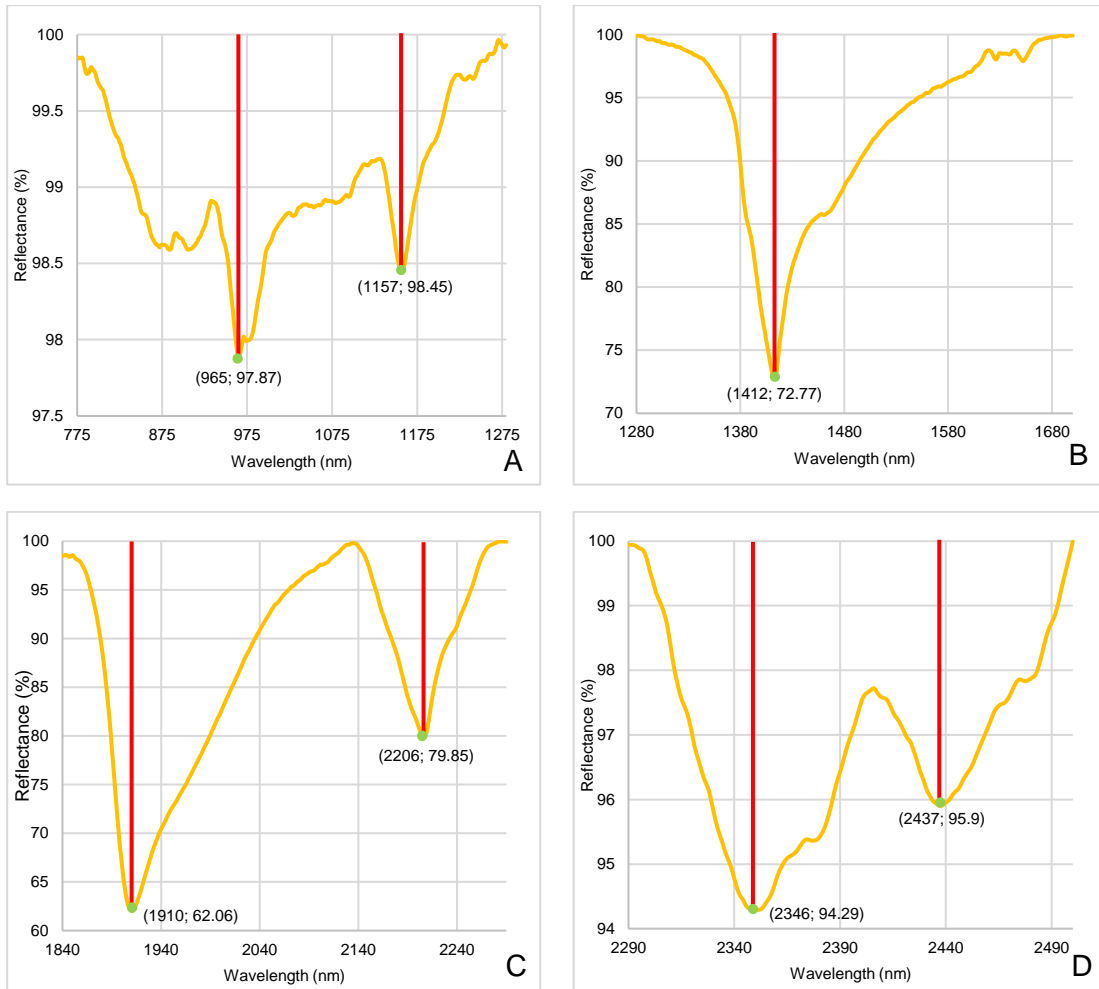


Figure 27 - The four portions of wavelength (A, B, C, D) used for the study of absorption zones in the spectral signature of spodumene. The spectrum is presented with the continuum removed. The red vertical lines represent the depth caused by the effect of absorption. The length of the red line is the percentage of absorption.

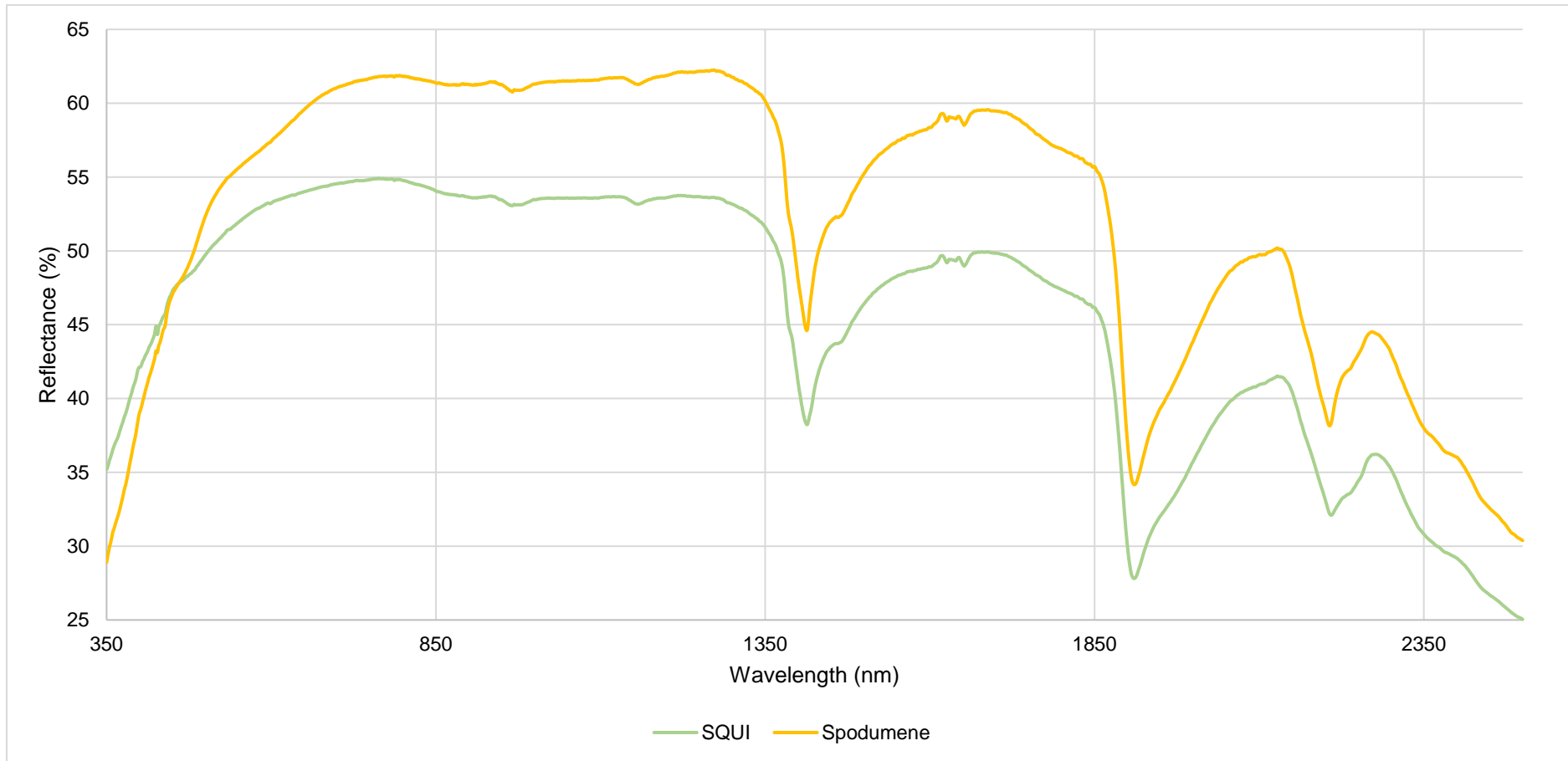


Figure 28 - Spectral signature of spodumene VS Spectral signature of SQUI.

#### 4.1.4 Zinnwaldite

As mentioned before, the sample where the spectral data of zinnwaldite minerals were collected (Figure 29) had been provided by the Departamento de Geociências, Ambiente e Ordenamento do Território, da Faculdade de Ciências da Universidade do Porto, and for this reason, there is not much information regarding the place of sampling or the host lithology. The identification of the measurement points used for the elaboration of the spectral signature of zinnwaldite is presented in Table 7.

The spectral signature of zinnwaldite was accomplished based on seven spectra, measured in points of the sample where these minerals had been visually identified. The analyses of the graphic representation of all these seven spectra, presented in Figure 30 shows an intense correlation between each other, presenting the same curve tendency and absorption zones. The differences in the percentages of reflectance are similar to the other minerals studied, with a wide range of possible percentages, where the difference from the highest to the lowest is about 30%.

Furthermore, it is possible to find other visible differences, such as the lack of noise in 13\_03\_0002, 13\_03\_0003, and 13\_03\_0005 spectra, when compared to the remaining spectra, which at the wavelength from 1610 nm to 1660 nm, is detected variations in the percentage of reflectance, with this going up and down. This noise, as seen previously, is also visible in the spectra from petalite and spodumene in the same wavelengths, which might be related to an interference caused by the transition between the SWIR1 and SWIR2 detectors of the spectroradiometer, that takes place at 1630 nm.



Figure 29 - Aplite-pegmatite vein sample with zinnwaldite (observed in brownish colors).

Table 7 - Identification of the measurement points, used in the elaboration of the spectral signature of zinnwaldite.

Sample	Measurement Point
Zin	13_03_00002
	13_03_00003
	13_03_00005
	13_03_00007
	13_03_00008
	13_03_00010
	13_03_00012

The observation of the spectral signature of zinnwaldite, presented in Figure 31 and obtained considering the arithmetic average of the spectral data from the measurement points, shows a spectrum with several zones and peaks of absorption. Once again, to perform a better examination of the absorption in this spectrum, the continuum was removed (Figure 32) and then sliced into four portions.

In the first portion of the spectrum, compressed between 700 nm and 1360 nm (Figure 33 (A)), it is noticeable the presence of two absorption zones, producing two troughs, the first between the 800 nm and 1000 nm and the second between 1000 nm and 1360 nm. In this way, it is perceptible the effect of absorption throughout this part of the spectrum, which due to the second trough be more intense than the first, leads to a successive decrease of reflectance, from the start to finish of the portion.

The second portion, between 1360 nm and 1800 nm, showed in Figure 33 (B), includes an absorption peak, with the maximum percentage of absorption of 30.1% at 1413 nm. This peak is defined by a rapid increase and decrease of absorption. This portion also includes the visible noise already mentioned, from 1610 nm to 1660 nm.

The third portion, between 1800 nm to 2290 nm (Figure 33 (C)) starts with a very small zone of absorption, with small percentages, just before the wavelength of 1850 nm. Right after, comes up a peak, with a rapid increase of absorption, reaching the maximum at 9.4% in 1912 nm, decreasing then at a lower rate. Just before the second peak, it is noticeable another small zone of absorption, with higher percentages than the last. For the second peak, the absorption rapidly increases, reaching the maximum at 2207 nm with 32.4% of absorption, getting back to decreasing at the same speed.

Lastly, the fourth portion, between 2290 nm and 2500 nm, presented in Figure 33 (D), shows an intense interference in the spectrum by absorption. This is marked by

the presence of two peaks, the first at 2351 nm, with 15.5% of absorption and the second at 2439 nm, with 11.4%.

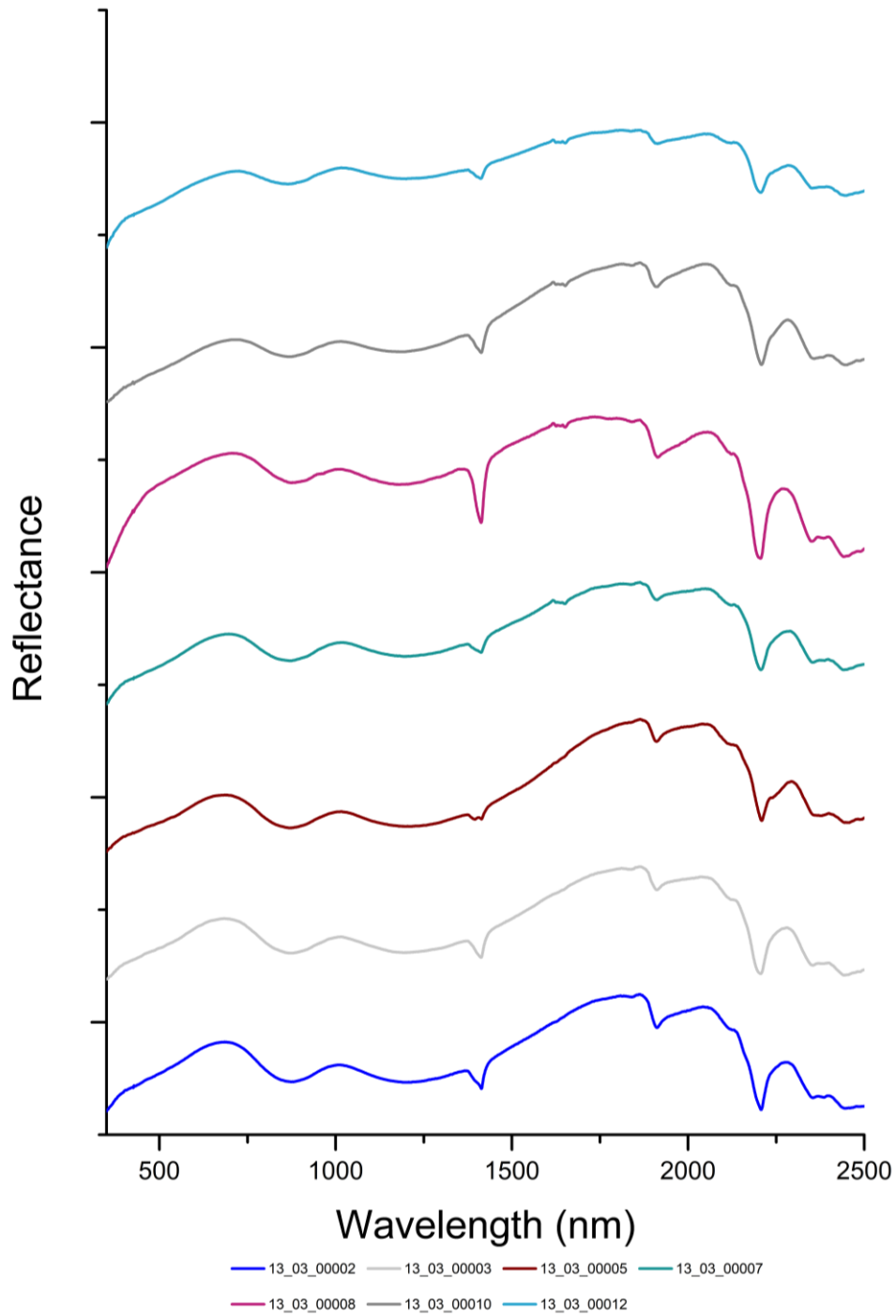


Figure 30 - Graphic representation of the seven electromagnetic spectra obtained from the study of zinnwaldite minerals.

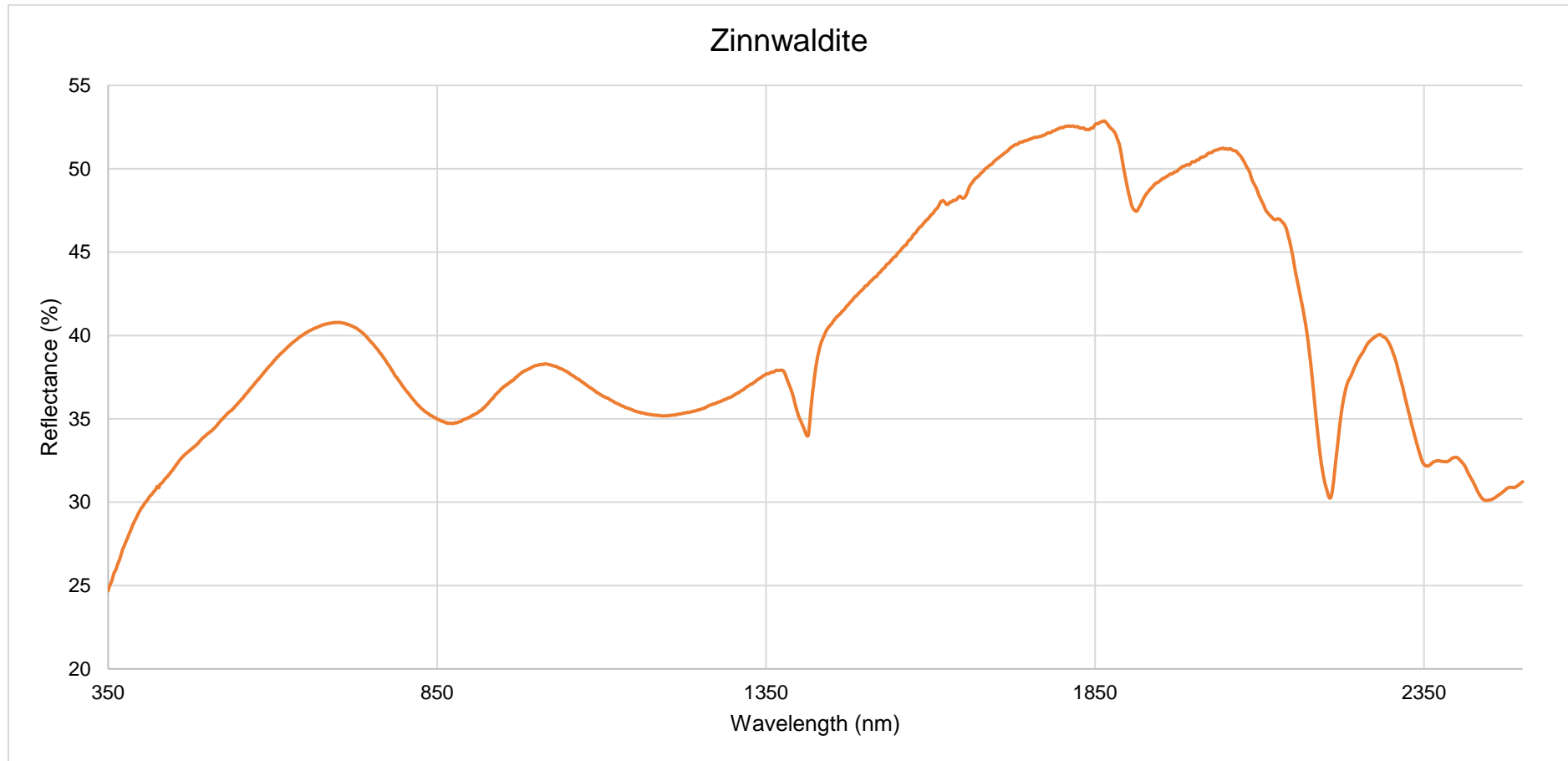


Figure 31 - Spectral signature of zinnwaldite.

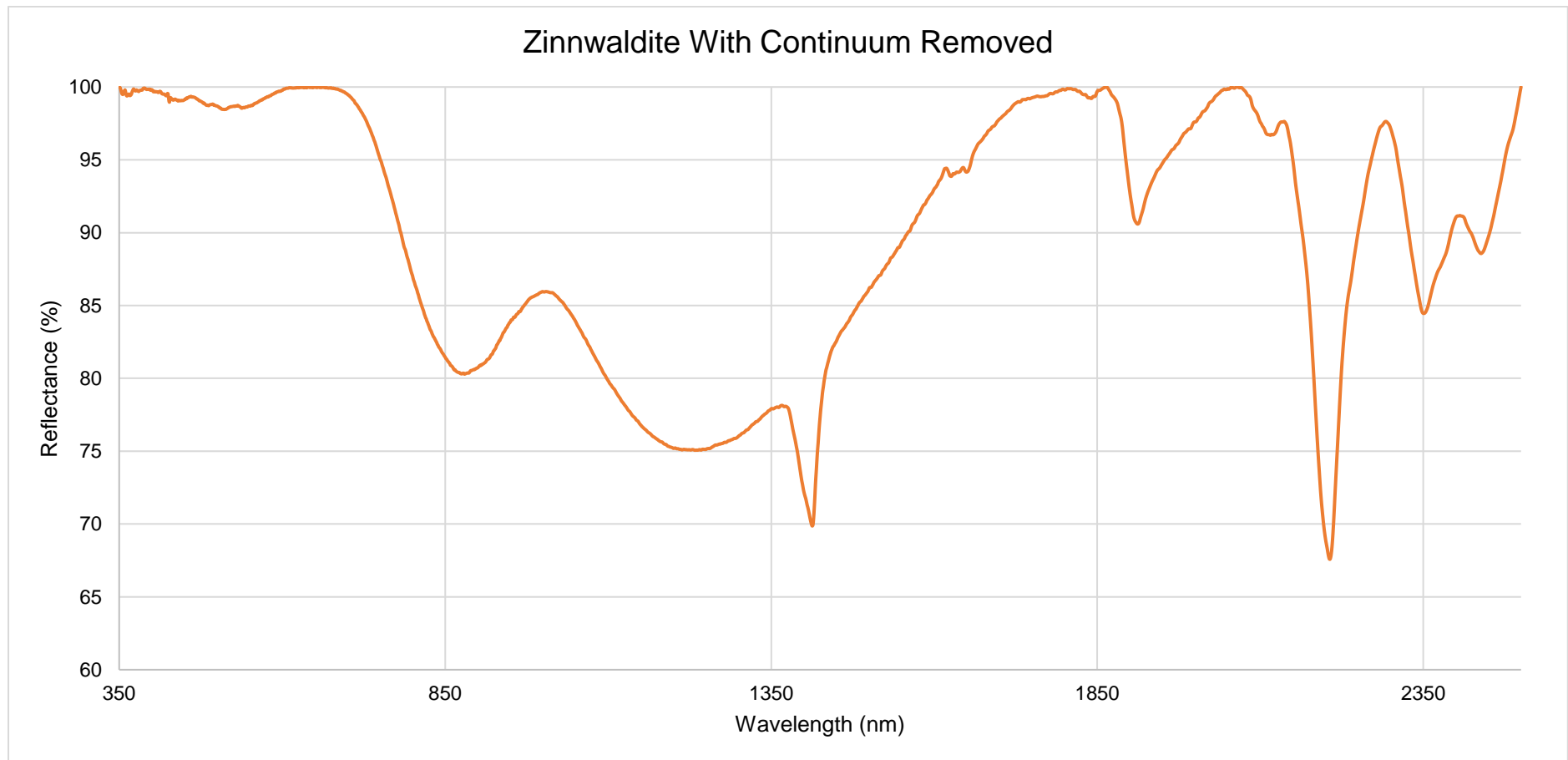


Figure 32 - Spectral signature of zinnwaldite with the continuum removed.

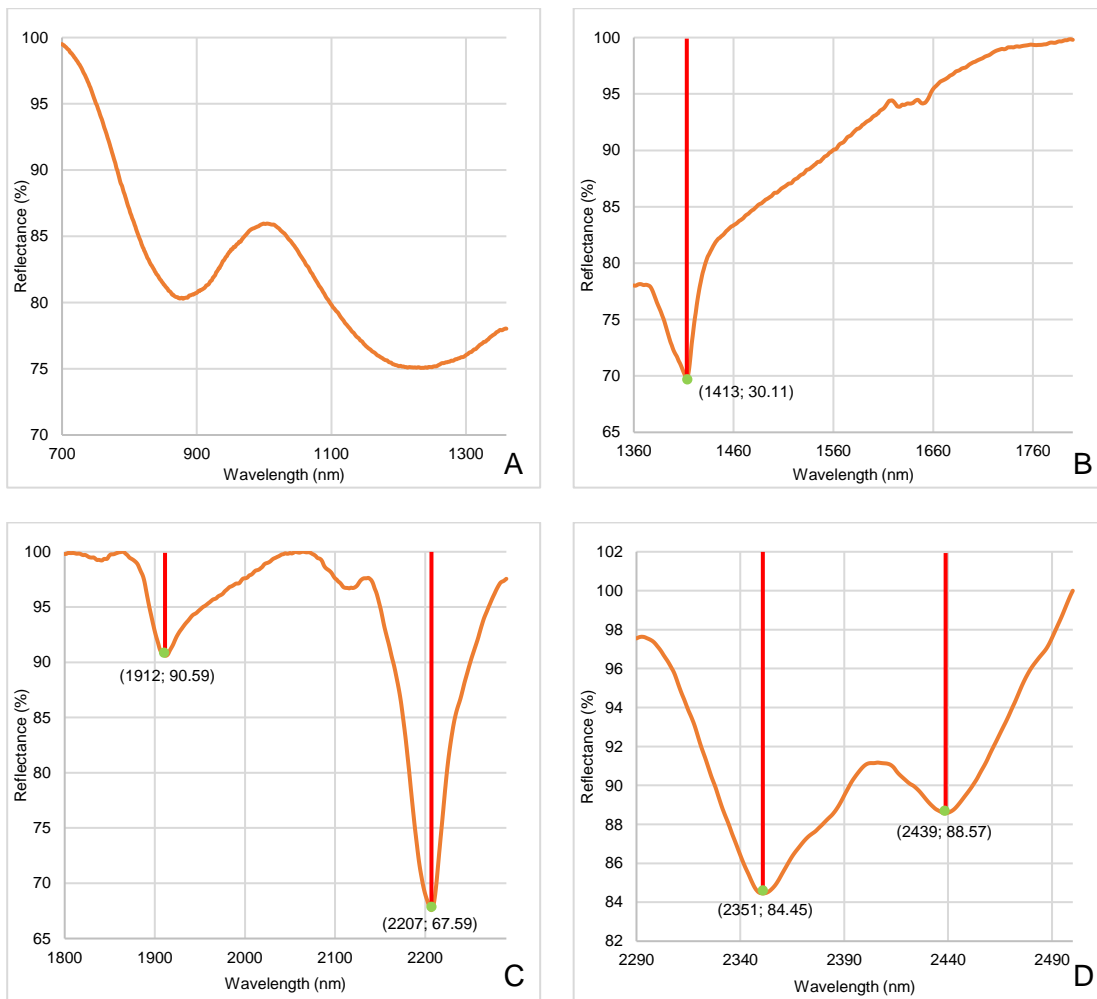


Figure 33 - The four portions (A, B, C, D) sliced from the spectral signature of zinnwaldite spectrum with continuum removed. The red vertical lines represent the depth caused by the effect of absorption. The length of the red line is the percentage of absorption.

#### 4.1.5 Montebrasite

Montebrasite sample was also provided by the Departamento de Geociências, Ambiente e Ordenamento do Território, da Faculdade de Ciências da Universidade do Porto and therefore there is not much information about it. However, it was known that the place of sampling occurred in the surroundings of Massueime mine (40°48'17.0"N; 7°12'52.9"W), southern to the aplite-pegmatite field of Fregeneda-Almendra.

From the available sample was only possible to measure three points where montebrasite was recognized, due to the size of the sample and mineral (Figure 34). Figure 35 represents the spectral data from the three measured points, 13\_03\_00084, 13\_03\_00085, and 13\_03\_00086, where only this last deviate from the trend, at the beginning of the spectrum, possibly due to bad positioning of the probe from the spectroradiometer, allowing to some external light to interfere with the measurement.

The spectral signature of montebrasite, presented in Figure 36, initiates with a small increase of reflectance, in the VNIR zone, and after slowly starting to decrease until the end of the spectrum (from ~810 nm to 2500 nm). The first half of the spectrum presents a stable tendency without showing signals of absorption peaks. The second part, from 1350 nm to 2500 nm, as a more complex appearance, being characterized by the presence of numerous absorption peaks, where is possible to identify five of these peaks, at 1538 nm, 1848 nm, 1995 nm, 2176 nm, and 2375 nm, respectively.

The continuum was removed (Figure 37) for montebrasite and sliced into portions, to have a better analysis of the effect of energy absorption in this spectrum. Right at the beginning of the spectrum with the continuum removed, it is noticeable a slight effect of absorption, which is related to the initial increase of reflectance, as happened before for the other studied Li minerals.

The first portion was taken between the 800 nm and the 1260 nm, as presented in Figure 38 (A), where is noticeable a very small presence of absorption, which is related with the presence of two small peaks, with 1.1% of absorption, at 906 nm and 961 nm. This portion as a representation of low absorption percentages, which may produce a noisy appearance, with the reflectance going up and down, especially in the second half.

The second portion comes from 1260 nm to 1875 nm (Figure 38 (B)) and shows the existence of various small peaks of absorption, where is possible to highlight two of them with higher percentage values, at 1538 nm with 18.9% of absorption and at 1848 nm with 14.9%. The other small peaks are placed throughout this portion, being the first two marked at 1290 nm and 1355 nm, then within the increasing of absorption for the

first bigger peak mentioned, two more small peaks are identified at 1416 nm and 1446 nm, preceded by a zone, between 1482 nm and 1493 nm, there exists a slight resistance to this increase of absorption. In correlation with the spectra of petalite, spodumene, and zinnwaldite, also montebrasite presents that noise type, between the wavelengths of 1610 nm and 1660 nm. Between the two bigger peaks mentioned, from 1702 nm and 1814 nm, the spectrum is strongly affected by absorption creating a trough, with 4.1% of absorption. Within this zone exists two troughs, at 1736 nm and 1766 nm, being this last where if found the maximum absorption.

The third portion comes up between 1875 nm and 2330 nm, as presented in Figure 38 (C), with a lesser complex appearance than the last. In the first wavelengths (~1915 nm) is noticeable a small trough, which after a quick increase of reflectance, decreases rapidly originating an absorption peak, with 37.1% of absorption at 1995 nm. Another small trough comes up right after this last peak (~2060 nm), being more accentuated than the last. With a rapid increase of absorption, another peak is detected with maximum absorption of 60.1%, at 2176 nm, for then the decrease to be done at a lower speed than the increase.

Lastly, the fourth portion, from 2330 nm to 2500 nm, showed in Figure 38 (D), present a great absorption effect, producing an absorption peak with a maximum of 50.8% at 2375 nm, where the rhythm of increase and decrease of absorption, is practically the same. Another peak is detected with a wide aperture and a lower percentage of absorption, of 6.6%, at the wavelength of 2478 nm.



Figure 34 - Sample with a mineral of montebrasite, identified inside the red circle, from Massueime mine.

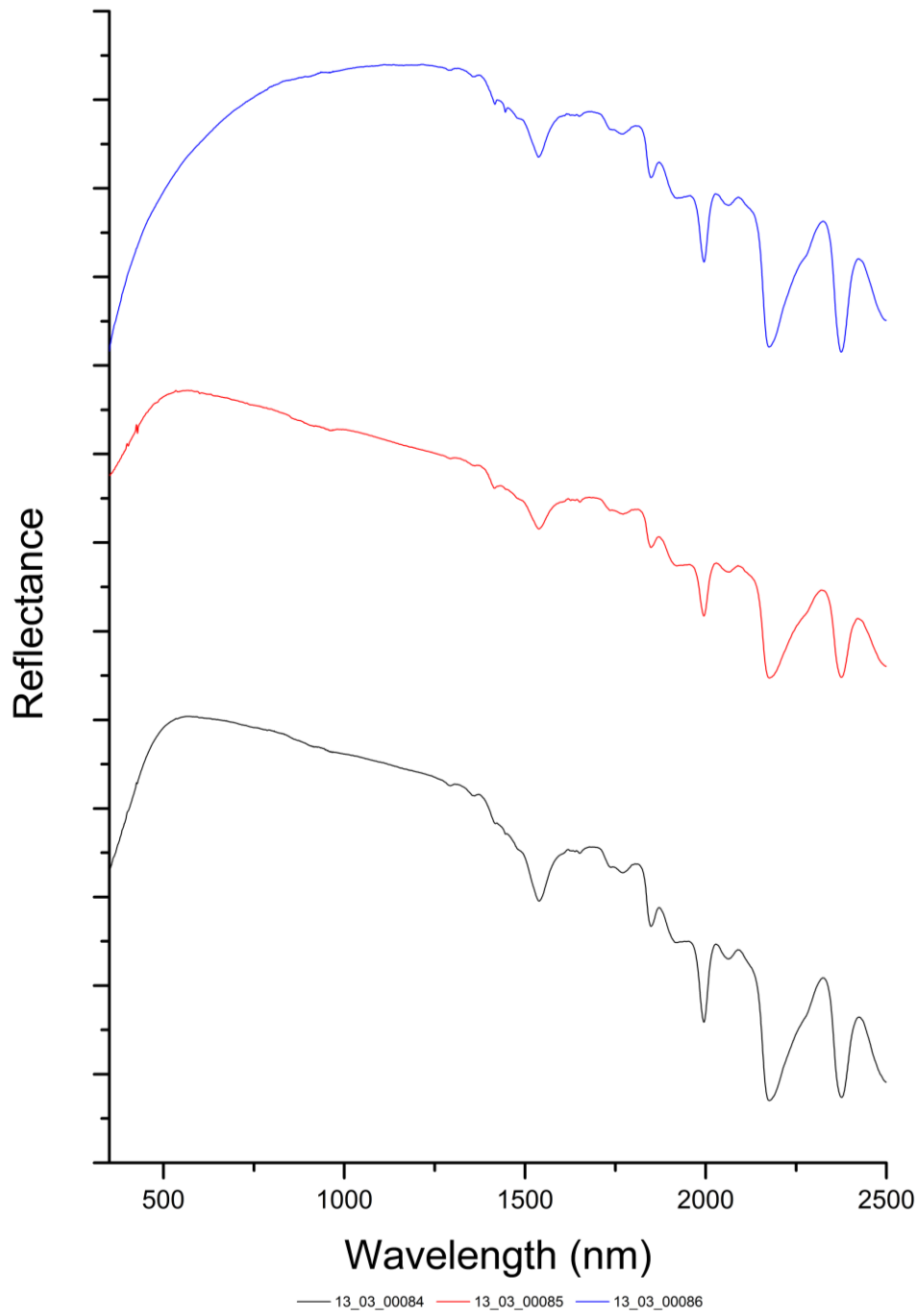


Figure 35 - Graphic representation of the three electromagnetic spectra obtained from the study of a montebrasite mineral.

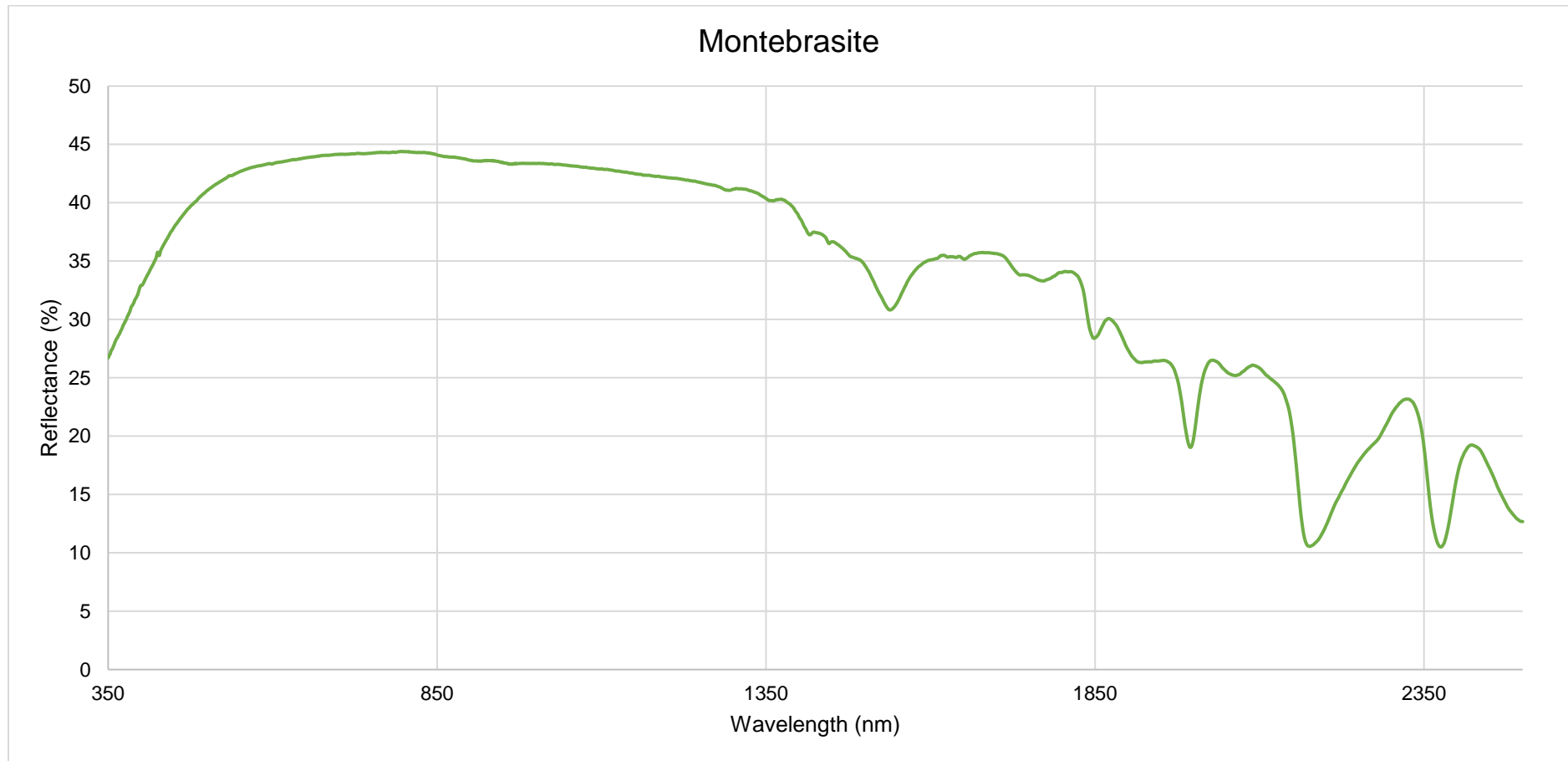


Figure 36 - Spectral signature of montebrasite.

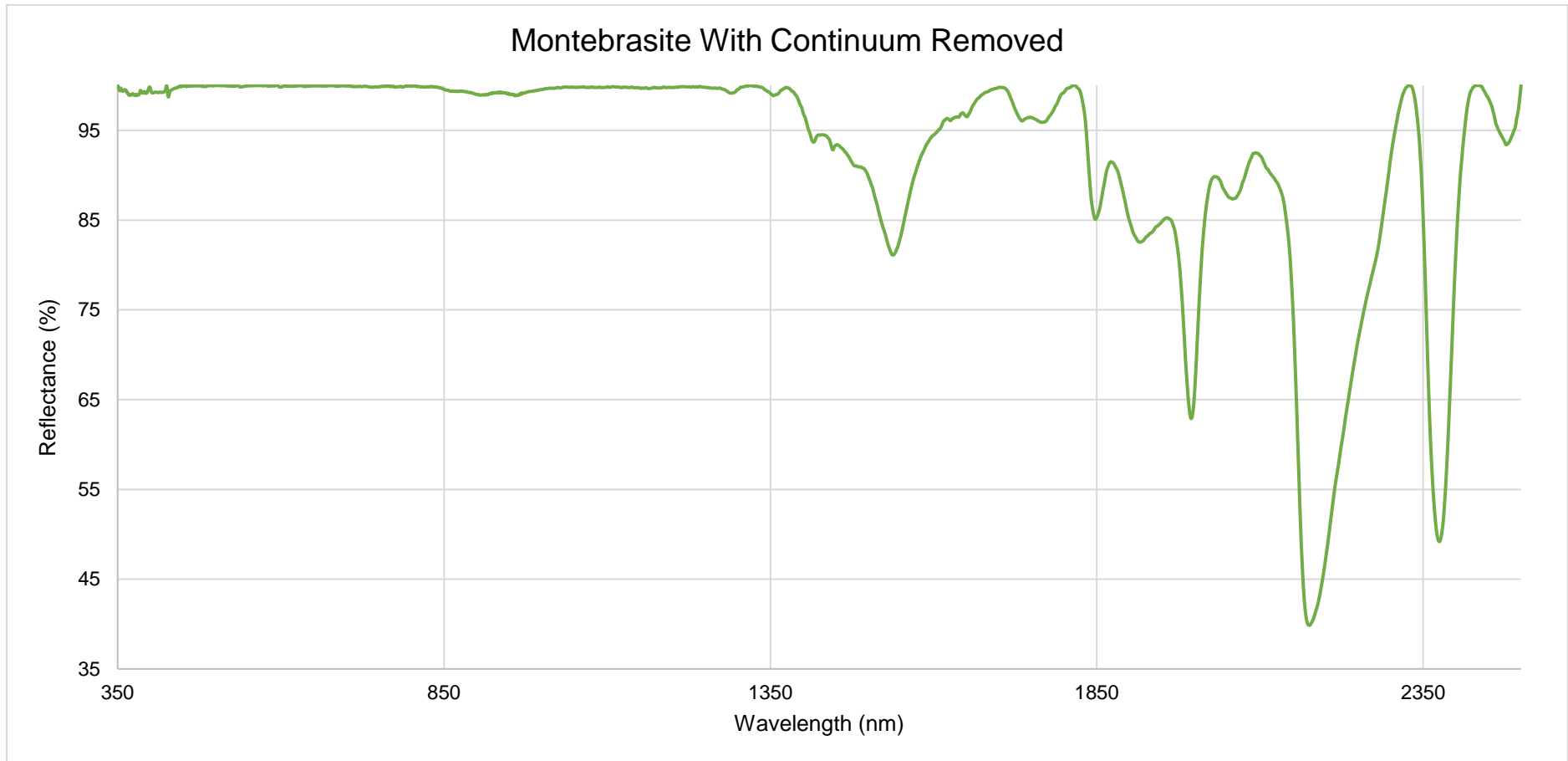


Figure 37 - Spectral signature of montebrasite with the continuum removed.

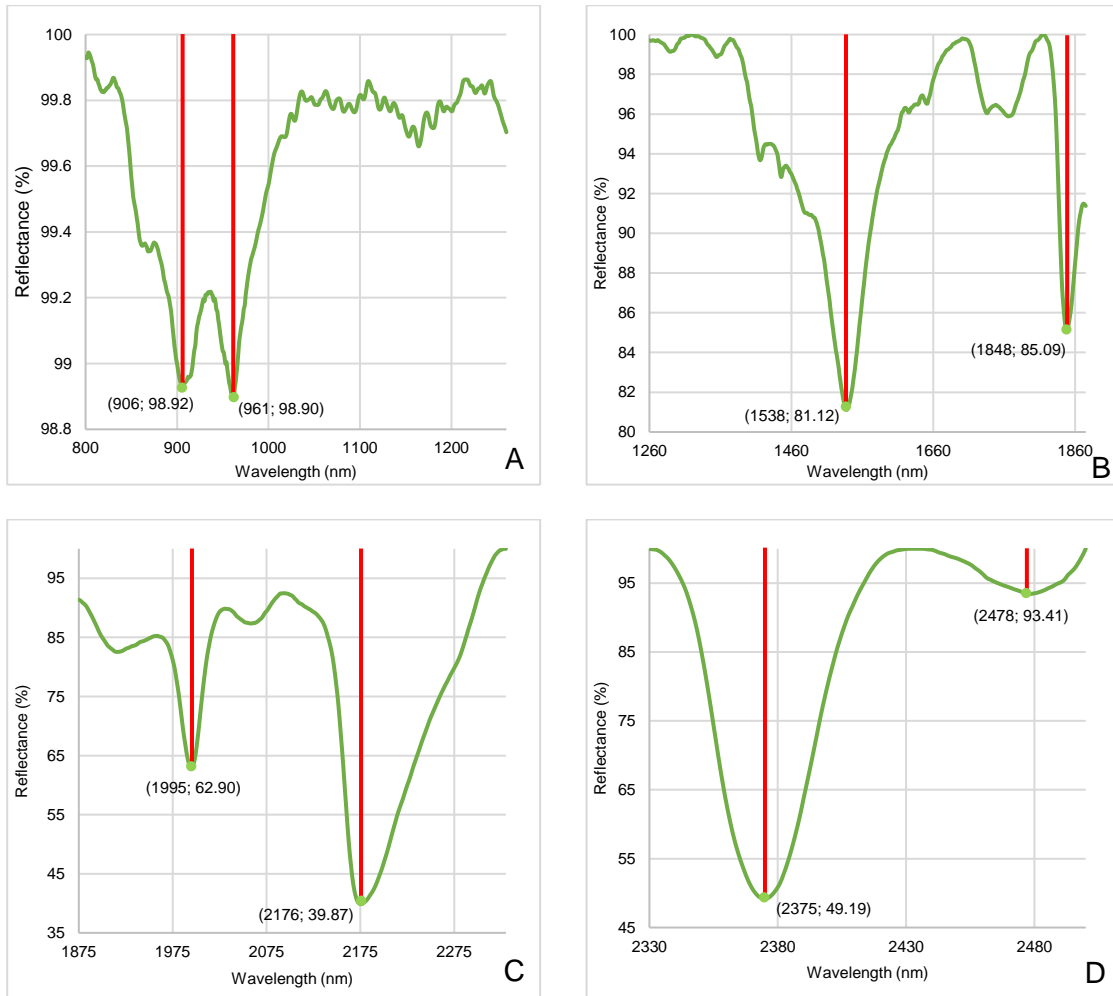


Figure 38 - The four portions (A, B, C, D) sliced from the spectral signature of montebrasite spectrum with continuum removed. The red vertical lines represent the depth caused by the effect of absorption. The length of the red line is the percentage of absorption.

## 4.2 Comparison Between Lithium Minerals

### 4.2.1 Petalite VS Spodumene

The comparison of petalite and spodumene spectral signatures (Figure 39), evidences an identical reflectance trend throughout the spectra. The reflectance starts by rapidly increase, getting to the maximum percentages in the first part of the spectrum (350 nm to ~800 nm), for then initiate a decrease in the remaining wavelengths. Although they might seem to have the same trend, spodumene has a slightly more continuous trend after the initial increase, prolonging the maximum reflectance percentages, showing only decrease in the second half of the spectrum.

In the spectra with continuum removed (Figure 40) is possible to notice that the main absorption features are coincident for both minerals. Presented at, ~1410 nm, ~1910 nm, and ~2200 nm, and relate to OH<sup>+</sup>+H<sub>2</sub>O, H<sub>2</sub>O, and Al–OH features, respectively, which are diagnostic characteristics of the presence of clay minerals from the smectite group (Clark, 1999; Clark et al., 1990). Once clay minerals are one of the several minerals of supergenic alteration of these Li minerals (Costa et al., 2016), the presence of its typical features may indicate that alteration is interfering with the spectral signature of these minerals. Also, the absorption peaks of fewer expression seem to be identical in both spectra.

The only main difference is related to the absorption peaks depth, as is possible to observe in Figure 40. Where spodumene presents longer peaks than petalite, which can be caused by various reasons, like the chemical composition of the mineral. Once spodumene presents a higher percentage of Li and Al, which may mean longer absorption peaks if the chemical element is the one responsible for the absorption. Also, the alteration state may influence the obtained peaks, due to the loss of the original's features and chemical composition of the mineral in the study. Besides that, the existence of small Al–OH secondary absorption features at 2346 nm and 2437 nm, in spodumene signature, is a diagnostic characteristic of the presence of illite features (Hunt and Salisbury, 1970; Scott and Yang, 1997; Naleto et al., 2019), and can be used to distinguish it from petalite, since this last presents these features with very shallow expression.

Considering what was analyzed, is possible to understand that the signatures of petalite and spodumene are dominated by spectral features of alteration minerals. In both signatures is noticeable a bigger depth at the H<sub>2</sub>O when compared to the Al–OH

feature, which can define a predominance of montmorillonite, since this is the only minerals from the smectite group that is known to absorb water from the air (Clark et al., 1990, Hunt and Ashley, 1979). Once spodumene also presents diagnostic features of illite, is understand that this signature is dominated by features of montmorillonite, and illite. Contrary, petalite spectral signature is only dominated by montmorillonite.

#### 4.2.2 (Petalite and Spodumene) VS Lepidolite

The comparison of the signatures produced by the minerals of petalite and spodumene to the spectrum of lepidolite spectral signature, does not evidence a distinctive spectrum, yet some disparities are detected. The evolution of reflectance (Figure 41), results in a trend slightly different, lepidolite spectrum present a curvier tendency, with the highest registered percentages of reflectance happening in the wavelengths of the middle (~1610 nm), while petalite and spodumene presented their highest values in the first third of the spectrum.

When analyzing the most evident absorption peaks (Figure 42), is possible to notice that lepidolite presents, also, the OH+H<sub>2</sub>O, H<sub>2</sub>O, and Al-OH features, yet the symmetric absorption features at 1410 nm and 2196 nm are narrow when in comparison with the broader asymmetric features at ~1413 nm and ~2007 nm, presented by petalite and spodumene. Moreover, the location of the main Al-OH feature at 2196 nm instead of around ~2007 nm, shows a distinctive difference.

Contrary to petalite and spodumene, which presented the free molecular water feature around ~1910 nm as the deepest absorption peak (Hunt and Ashley, 1979), in lepidolite, the OH+H<sub>2</sub>O and Al-OH (1410 nm and 2196 nm) features are the most pronounced. Moreover, the Al-OH secondary absorption features at 2346 nm and 2432 nm in the lepidolite spectrum, are much more accentuated, presenting deeper absorption peaks than in spodumene. These features presented by lepidolite, seem to be diagnostic for white mica, according to Scott and Yang, (1997).

#### 4.2.3 Lepidolite VS Zinnwaldite

The comparison between lepidolite and zinnwaldite continuum removed spectra, presented in Figure 43, shows in the first half of the spectrum (350 nm to ~1350 nm) two different tendencies. Zinnwaldite presents a wavier trend, marked by two broad absorptions zones, from ~800 to 1250 nm, which summing with the crescent ramp visible

from ~1250 to ~1800 nm, are probably features related to the presence of ferrous iron ( $\text{Fe}^{2+}$ ) spectral features (Hunt and Ashley, 1979). In lepidolite spectrum, such features are not possible to evidence. On the other hand, the second half of the spectra of these minerals, are very correlated presenting identical absorption features.

The most representative absorption peaks are correlated for both minerals, with similar  $\text{OH}+\text{H}_2\text{O}$ ,  $\text{H}_2\text{O}$ , and  $\text{Al}-\text{OH}$  features, having also, similar features around 2351 nm and 2439 nm, demonstrating both the diagnostic features characteristic of white mica.

All of these resemblances might be explained with the fact that lepidolite and zinnwaldite phyllosilicates from the mica group, justifying, in this way, the white mica characteristic features in both minerals spectral signatures.

#### **4.2.4 Montebbrasite VS (Petalite, Spodumene, Lepidolite, and Zinnwaldite)**

When comparing montebbrasite to the other studied Li minerals (petalite, spodumene, lepidolite, and zinnwaldite), it is noticeable some differences in the spectrum, where, especially in the second half part (~1350 nm to 2500 nm) the spectrum is intensely affected by absorption. Although some absorption peaks might be correlated to the ones identified in the other minerals, the differences between them are just too many for correlation.

The reasons behind these differences might be related to the fact that this is not a silicate like the other Li minerals studied, this is a phosphate mineral, resulting in a different chemical formula, which may translate to the differences obtained in the signature of montebbrasite. Even so, the presence of Li and Al might justify the slight correlations of the absorption peaks. The presence of a different crystal system may contribute to the contrasting results, once this is a triclinic mineral and the others are monoclinic.

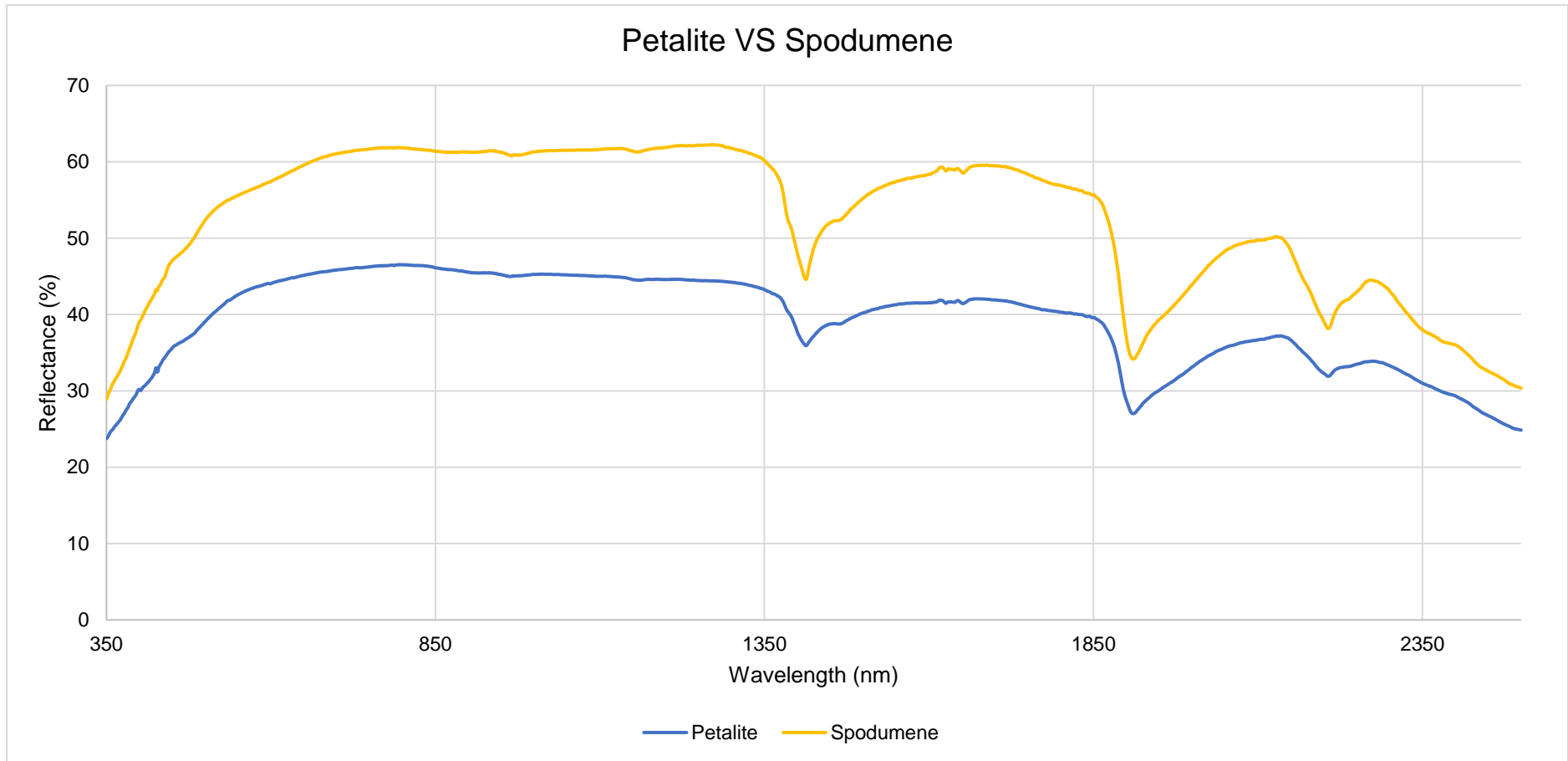


Figure 39 - Petalite VS Spodumene.

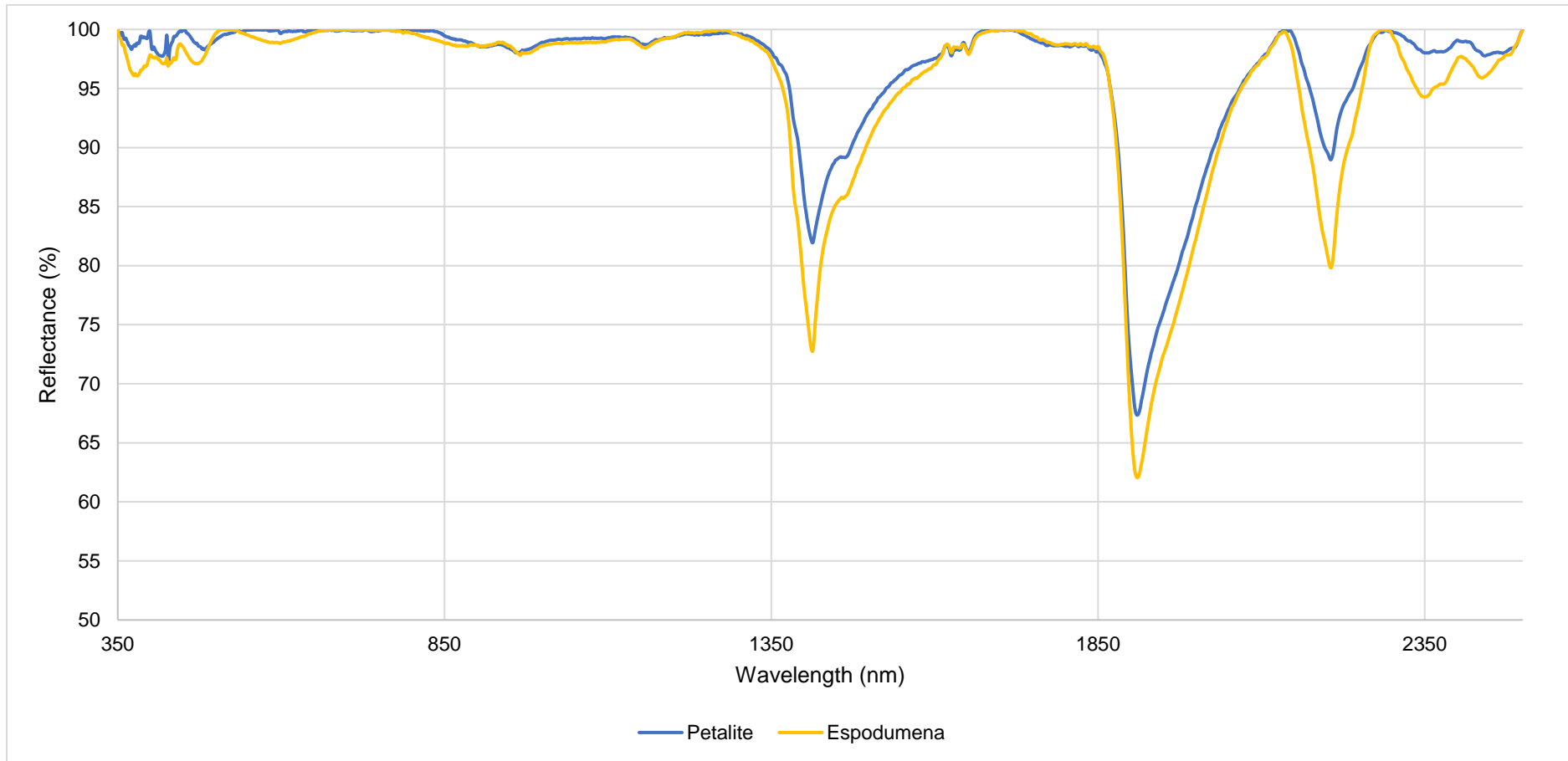


Figure 40 - Petalite and spodumene spectral signatures with the continuum removed.

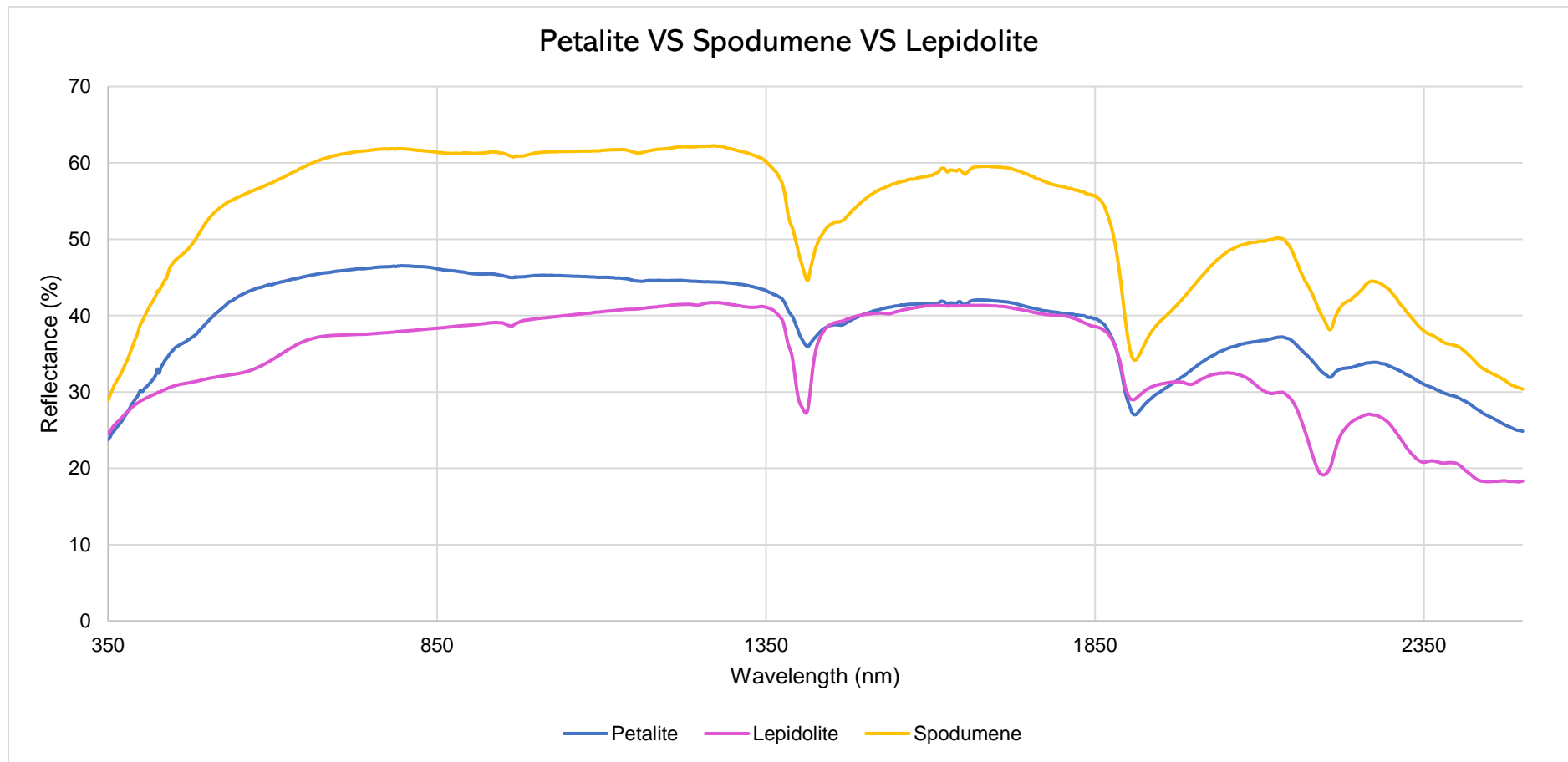


Figure 41 - Petalite VS Spodumene VS Lepidolite. Comparison between the three main lithium minerals from the Fregeneda-Almendra aphte-pegmatite field.

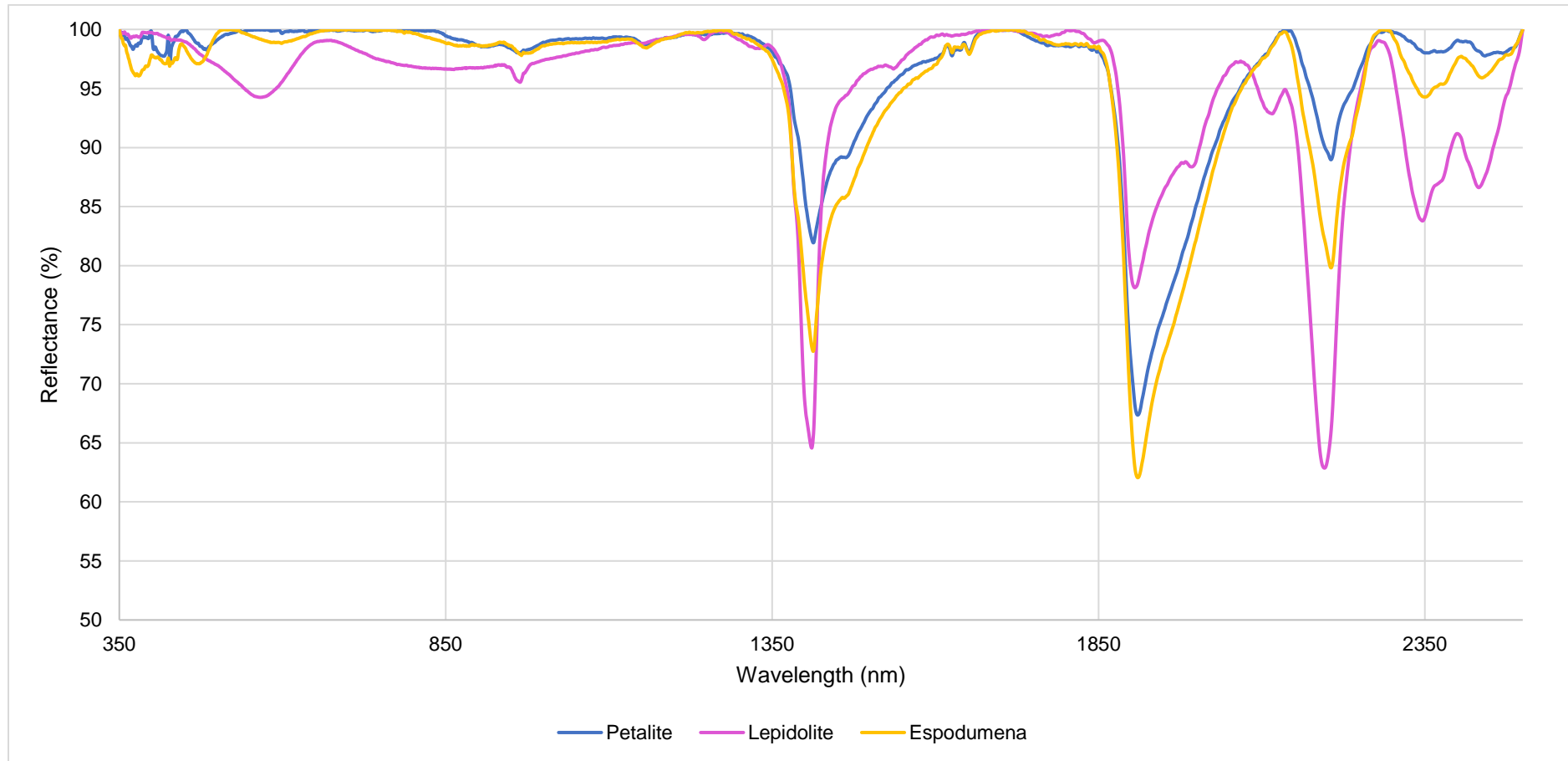


Figure 42 - Petalite VS Spodumene VS Lepidolite. Comparison with the continuum removed spectra.

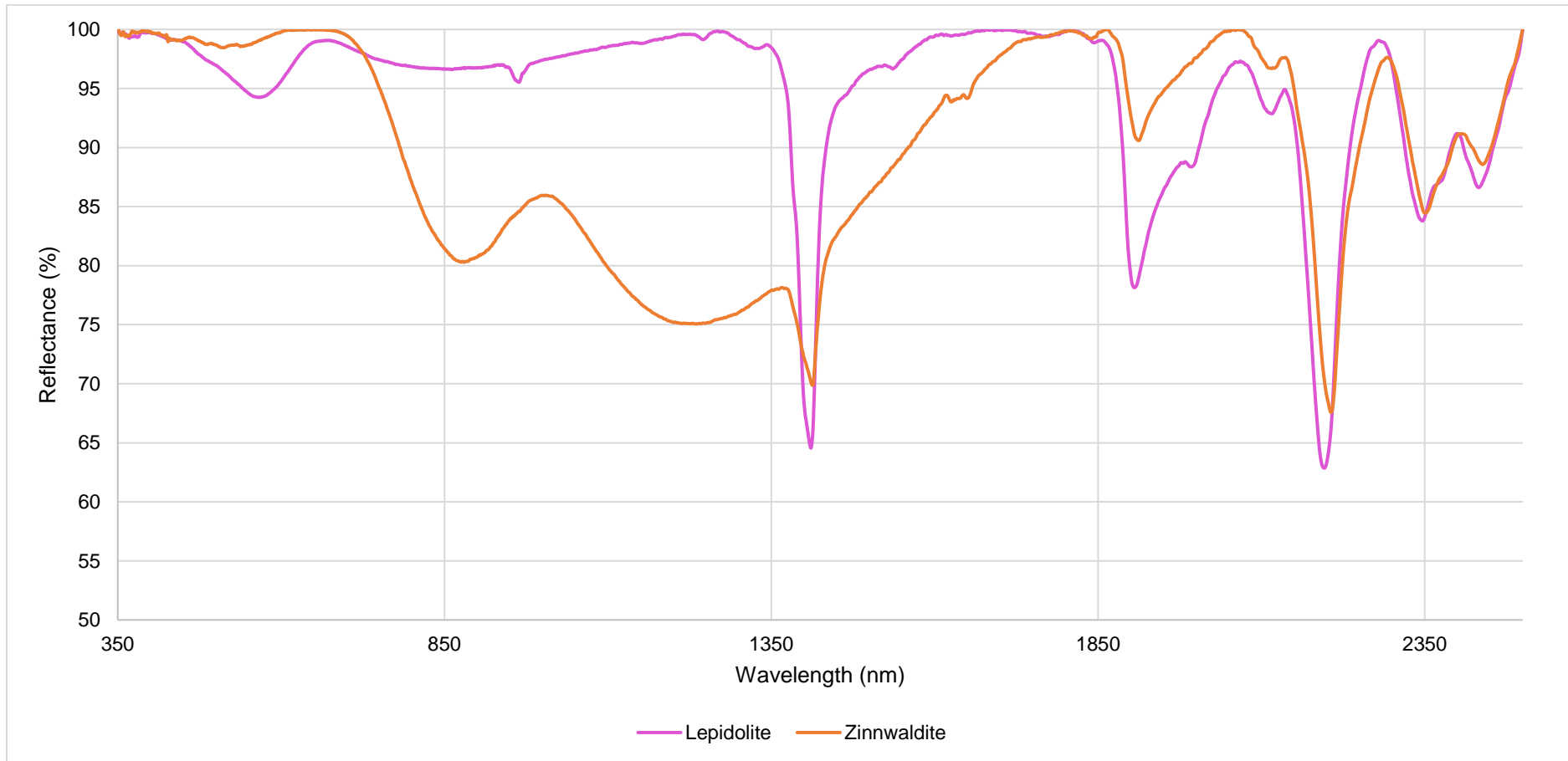


Figure 43 - Lepidolite VS Zinnwaldite. Comparison with the continuum removed spectra.

## 4.3 Spectral Signatures of the Host Lithologies

In this sub-chapter, three lithologies present at the study area are analyzed by its spectral signature, allowing, not only to have a better spectral knowledge of the area in study but also, to understand the principal differentiator features from the Li minerals.

### 4.3.1 T7 Aplite-Pegmatite and T5 Aplite-Pegmatite

The type 7 aplite-pegmatite spectrum was accomplished based on all the pegmatite samples collected in the Bajoca mine, during the field trip of February 2020. As mentioned before, this type is a Li-bearing aplite-pegmatite, having in its constitution petalite minerals (Viera, 2010), although, for the elaboration of the spectrum, was only used the measurement points where no Li minerals have been identified, having also used samples of pegmatites where was never identified any Li minerals, however belonging to these same aplite-pegmatite type. Figure 44 and Figure 45 show the aspect of the samples used, where is possible to identify a small presence of iron oxides.

The type 5 aplite-pegmatite is barren for Li, being mainly constituted by potassic feldspar and quartz (Vieira, 2010). The spectrum obtained was accomplished based on a single sample of small dimension and with an orangish-to-reddish aspect, showing the intense presence of iron oxides, as it is possible to observe in Figure 46.

Once petalite is the Li mineral present at T7 aplite-pegmatite veins, its spectral signature was used for the analysis and comparison of these two aplite-pegmatite types, due to this direct relation, being all graphicly represented in Figure 47.

Analyzing Figure 47 it is easily understandable that both aplite-pegmatites present the same main absorption peaks of petalite, at ~1413 nm (OH<sup>-</sup>+H<sub>2</sub>O), ~1910 (H<sub>2</sub>O) nm, and ~2206 nm (Al-OH), diagnostic for the presence of clay minerals from smectite group (Clark, 1999; Clark et al., 1990). When compared T7 pegmatite and petalite, it is difficult to find any differences, once both present an identical reflectance evolution and similar levels of reflectance, throughout the spectrum. The only particular difference detected, it is only noticeable in the observation of the spectra with the continuum removed (Figure 48) being related with the depths of the absorption peaks, where the ~1412 nm and ~2200 nm peaks are more accentuated, in the T7 pegmatite spectrum, as well as the peaks of fewer expression, at ~2348 nm and ~2436 nm. For the rest of the absorption peaks, especially for the VNIR zone (350-1300 nm), they are very

well correlated, excepting for a very small trough visible in T7, at ~683 nm, which is not found in the petalite signature.

The T5 aplite-pegmatite and petalite present very identical spectra in the SWIR zone (1300-2500 nm) (Figure 47), with absorption peaks very well correlated and with similar depths, as it is noticeable at the continuum removed graphic (Figure 48). The observation of the VNIR zone shows two quite different spectra, where T5 initiates with a high depth peak at ~488 nm, followed by a smaller expression peak at ~668 nm and a bigger peak at ~960 nm. The features found in the spectra between 400 nm and 1000 nm are associated with minerals containing iron oxides. So, the absorption feature found at ~668 nm is indicative of the presence of ferrous iron ( $Fe^{2+}$ ), as well as the feature present at ~960 nm is indicative of ferric iron ( $Fe^{3+}$ ) presence (Hunt and Ashley, 1979). These features are probably related to the iron oxides visible on the surface of the study sample, and for this reason, these features would probably be not existent if the sample was free of these oxides, having possibly an identical spectrum to petalite, throughout. For these same reasons, the small trough found in T7 pegmatite, at ~683 nm, might be also related to the small iron oxides present in the surface of the sample.



Figure 44 - Sample of a T7 pegmatite, collected in Bajoca mine, at 448 location. Orangish-to-reddish tones, indicative of the presence of iron oxides.



Figure 45 - Sample of a T7 pegmatite, from the stockpile of Bajoca mine. Presence of iron oxides.



Figure 46 - Sample of a T5 pegmatite, where is noticeable the intense presence of iron oxides.

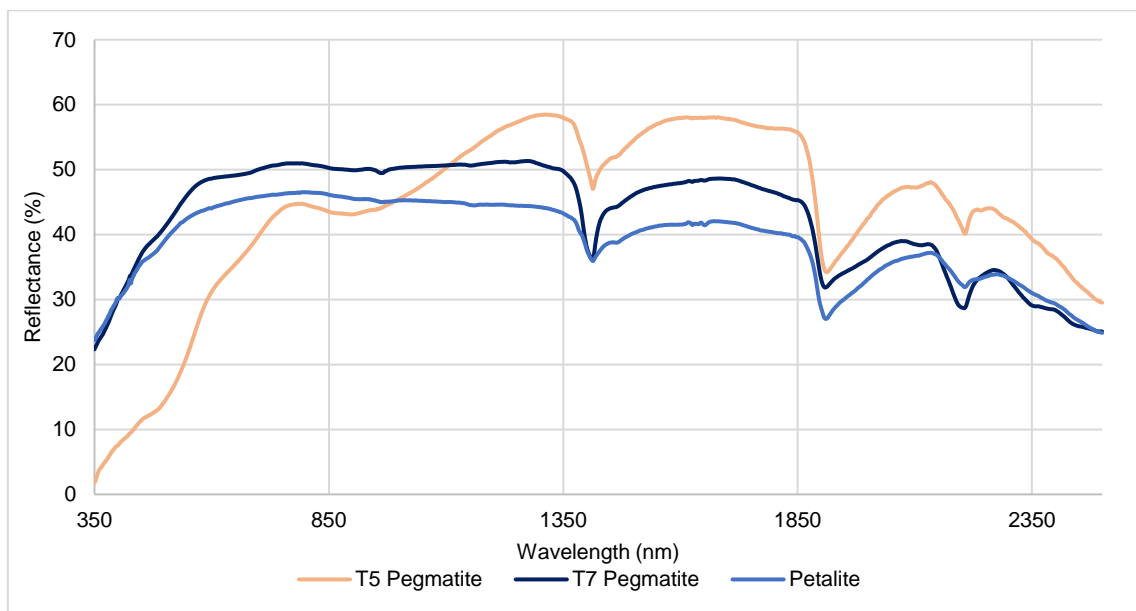


Figure 47 - Graphic comparison of the spectra presented by the T5 pegmatite, T7 pegmatite and petalite.

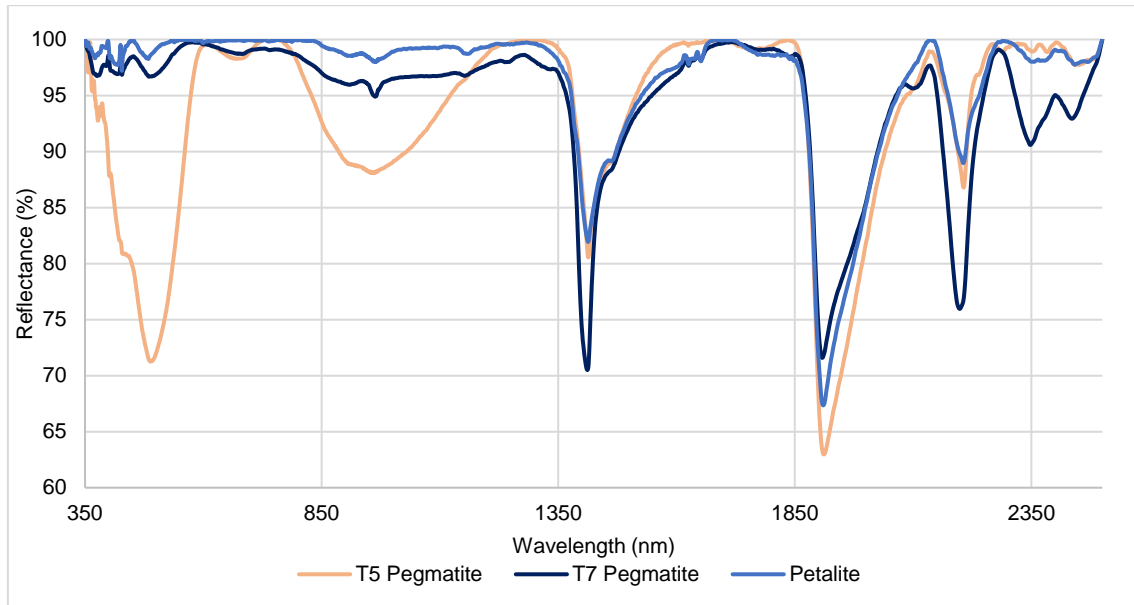


Figure 48 - Graphic comparison of the spectra with the continuum removed presented by the T5 pegmatite, T7 pegmatite and petalite.

#### 4.3.2 Complexo Xisto-Grauváquico

The study of the CXG spectra was accomplished with all the metasedimentary samples available, being sorted into five categories, Desejosa Formation, CXG T5, CXG T6, CXG T7, and CXG T8. For the elaboration of the spectra, all the measurement points done in the samples were used, despising only the ones which showed some kind of error, either because of the measurement instrument failure or due to the interference of superficial vegetation of the sample.

The Desejosa Formation spectrum was elaborated considering an average of the values from the measurement points obtained in the samples collected during the field trip of February 2020 (Figure 49), being from locations where no aplite-pegmatite veins were identified, and for that reason, are samples without a known aplite-pegmatite connection. On the other hand, the remaining defined categories were obtained with samples from the Departamento de Geociências, Ambiente e Ordenamento do Território, da Faculdade de Ciências da Universidade do Porto, being collected in the surroundings of an aplite-pegmatite vein. In this way, CXG T5, represented in Figure 50, was accomplished with metasedimentary samples collected near a type 5 aplite-pegmatite vein, and in the same way CXG T6, CXG T7, and CXG T8 (Figure 51, Figure

52, and Figure 53, respectively) were accomplished with samples collected in the surroundings of type 6, type 7, and type 8 aplite-pegmatite vein, respectively.

The study of the graphic representation of these CXG spectra, presented in Figure 54, allows considering that the aplite-pegmatite vein type does not affect the host lithology, since these different categories do not show any particular difference, being presented with similar reflectance evolution and the same absolute absorption peaks. If the aplite-pegmatite vein type would have affected the metasediments, these should have a different spectral response, at least, the Desejosa Formation spectrum, which does not have a connection to an aplite-pegmatite vein.

The analysis of Figure 54 also allows concluding the reasons why the previous applications of remote sensing techniques had so many difficulties in distinguishing these metasediments from the Li minerals. These CXG spectra present the same characteristic features of Li minerals, from this region of study, with the presence of the absorption peaks typical of clay minerals from the smectite group (~1414 nm; ~1914 nm; ~2209 nm) (Clark, 1999; Clark et al., 1990). When analyzing the reflectance, this presents a different evolution throughout the spectrum, initiating from lower reflectance percentages, comparing to Li minerals spectra, and having a longer increase until the maximum reflectance, even though generally, this maximum is lower than the maximum of the Li minerals reflectance.

Similar to what was analyzed for T5 pegmatite, the VNIR zone is also clearly affected by the presence of iron oxides. The CXG spectra present absorption features at ~490 nm, ~684 nm ( $\text{Fe}^{2+}$ ), and ~965 nm ( $\text{Fe}^{3+}$ ) (Hunt and Ashley, 1979) (Figure 55), something that is a clear difference from the Li minerals. In the case of CXG T7, the  $\text{Fe}^{2+}$  feature (~684 nm) was not possible to identify. The SWIR part of the spectra is very identical to the Li minerals spectra, presenting even correlation with the absorption peaks of fewer expression, as ~2350 nm and ~2447 nm. In opposition to the other CXG defined categories, in CXG T7 and CXG T8, was not possible to find an absorption feature at ~2254 nm, associated with a Fe-OH bond (Sun et al., 2001). This is a feature which was not possible to identify in Li minerals signatures once these minerals seem to not present iron related features.

The continuum removed spectrum of CXG T5 (Figure 55), presents more accentuated absorption depths when compared to the remaining spectra. These and the other small disparities found in the CXG spectra are probably related to differences in the mineralogy and proprieties of the sample studied, like alteration and iron oxides presence.



Figure 49 - Metasedimentary sample from CXG, Desejosa formation (445).



Figure 50 - Metasedimentary sample from CXG, collected near a T5 aplite-pegmatite vein (T5-19).



Figure 51 - Metasedimentary sample from CXG, collected near a T6 aplite-pegmatite vein (TC-19).



Figure 52 - Metasedimentary sample from CXG, collected near a T7 aplite-pegmatite vein (T7-19).



Figure 53 - Metasedimentary sample from CXG, collected near a T8 aplite-pegmatite vein (ALB-19).

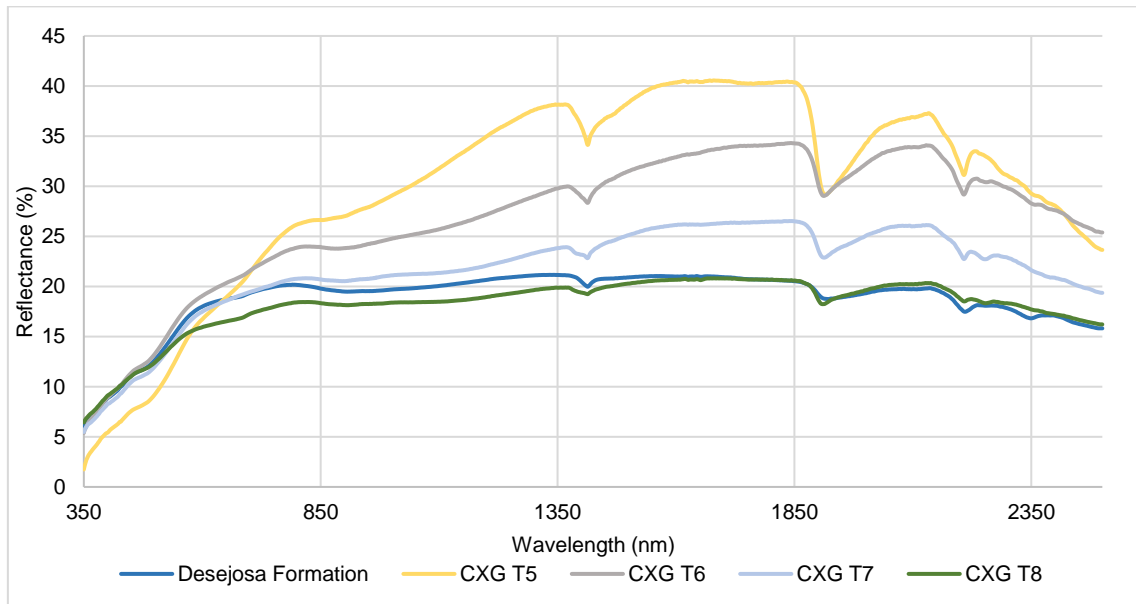


Figure 54 - Graphic comparison of the CXG spectra.

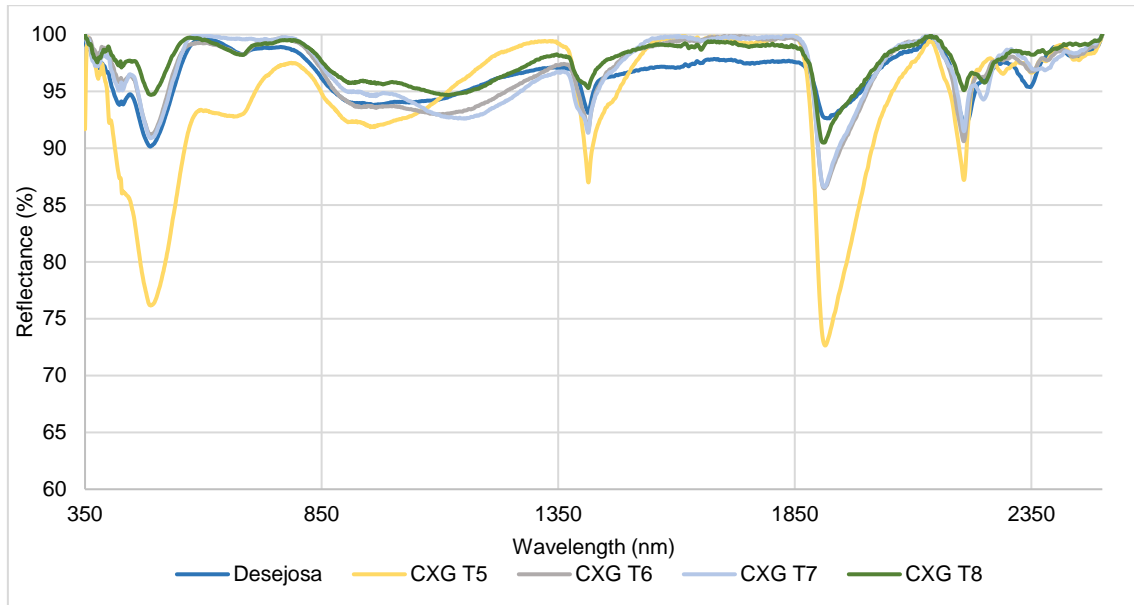


Figure 55 - CXG spectra with continuum removed.

### 4.3.3 Granite

The samples of granite used for the elaboration of its spectral signature were collected during the field trip of February 2020, in a quarry near Chãs, a village in Vila Nova de Foz-Côa, being these samples of a syn-D3 lithofacies from the MPLGC. These samples include fresh and altered granite, represented in Figure 56 and Figure 57, respectively. Figure 58 shows the obtained signatures for this granite.

The granite spectra shown in Figure 58, in a general way, presents identical spectral features to those found in CXG spectra, with similar reflectance values and evolution. However, these values in granite are slightly higher than the values in CXG, when compared to the ones presented by Li minerals these are lower. The main absorption peaks are identical to those found on Li minerals spectral signatures (~1413 nm; ~1922 nm; ~2206 nm), typical of the presence of clay minerals from the smectite group (Clark, 1999; Clark et al., 1990).

A more precise study of the absorption features and peaks was accomplished with the continuum removed spectra, presented in Figure 59. Where is possible to visualize that both granites are intensely affected by a broad  $\text{Fe}^{2+}$  absorption, from ~750 to ~1850 nm, which is much more pronounced in the fresh granite spectrum. Altered granite signature starts with spectral features at ~419 nm, ~495 nm, and ~685 nm, related with the presence of iron oxides, something that is not possible to find in the fresh

samples spectrum. In the remaining spectrum, both granites seem to produce identical spectral features at ~2255 nm, ~2339 nm, and ~2439 nm. The absorption pair, ~2255 /~2339 nm, are related to the Fe–OH and Mg–OH bonds, respectively (Sun et al., 2001), which together with the broad Fe<sup>2+</sup> absorption, define the presence of biotite features in these spectra. Also, a sharp and symmetrical feature at ~2206 nm, and a shallow ~1413 nm feature, when compared to the smectite spectrum, might indicate the presence of white mica. Once the H<sub>2</sub>O feature (~1922 nm) is presented more roundish and less symmetrical, can show the presence of quartz with water inclusions. This way is possible to consider that these granite samples are being represented by a mixture of biotite, quartz, and white mica spectral features.



Figure 56 - Fresh granite sample from the Mêda-Penedono-Lumbrales Granitic Complex (452).



Figure 57 - Altered granite sample from the Mêda-Penedono-Lumbrales Granitic Complex (453).

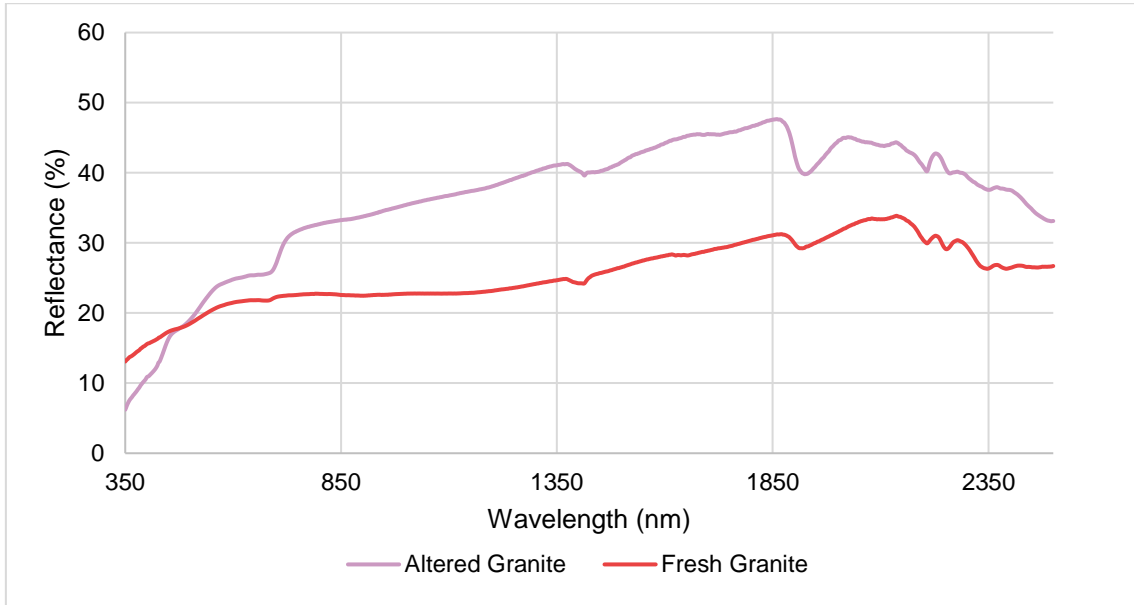


Figure 58 - Altered and fresh granite spectral signatures.

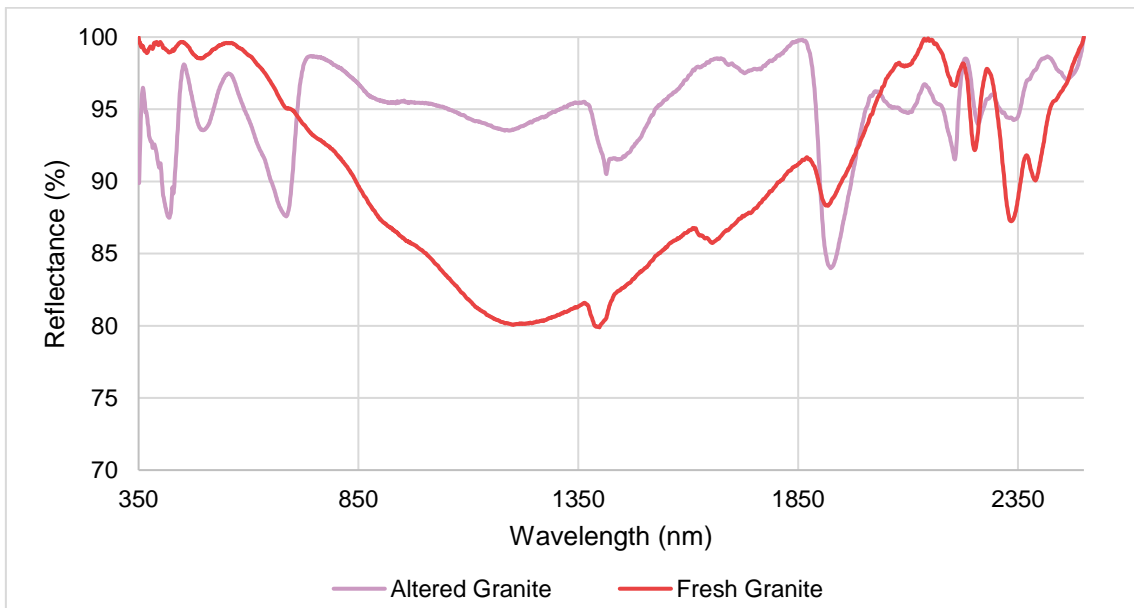


Figure 59 - Altered and fresh granite spectral signatures with the continuum removed.

## 4.4 Comparison with Spectral Libraries

In this part of the work, the previous spectral signatures of Li minerals obtained are compared to the reference spectra of minerals from the public access spectral libraries of USGS (Kokaly et al., 2017) and ECOSTRESS (Baldrige et al, 2009). To accomplish an easier correlation between the signatures obtained and the reference spectra, a tool, *Identify*, on Spectragryph software (The Spectroscopy Ninja) (Menges, 2020) was used. This tool uses the “Spectral Similarity” algorithm (Menges, 2019) to find the highest rating match, based on the spectral features, through the calculation of Pearson correlation in the full-spectrum. For the present study, the top five matched reference spectra of minerals were analyzed.

### 4.4.1 USGS Spectral Library

When compared with the reference spectra of the USGS Spectral Library, the petalite spectral signature shows a high correlation with the reference spectra of montmorillonite, a phyllosilicate, clay mineral, from the smectite group. Montmorillonite appears four times in the top five results, occupying the three first positions, with a correlation rate of over 96.50%. Comparison of petalite spectral signature to the matched spectra of montmorillonite (Figure 60) is possible to notice that the main absorption peaks are identical, arising at the same wavelengths, yet with different depths, which, however, seem to be in proportion to the depths of petalite. Also, the reflectance evolution is very similar, even when affected by absorption, have an identical increase, and a decrease in the peaks.

The software used has also matched the petalite signature with a reference spectrum of sanidine, a potassic feldspar, which by analyzing might be difficult to find any resemblances, since these two spectra are only overlapped from 2100 nm to 2500 nm, and because has a very continuous spectrum. Although, the presence of sanidine may not be completely wrong, since the aplite-pegmatite veins where the samples of petalite were taken has potassic feldspar as one of the main mineralogies, and for this reason, the sanidine features can be interfering with the signature presented by petalite.

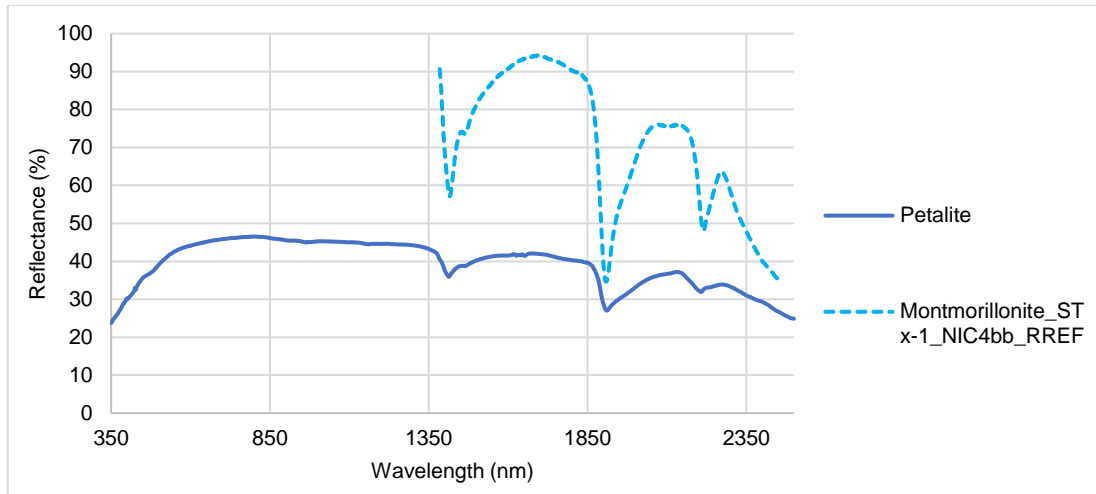


Figure 60 - Graphic comparison between petalite spectral signature and the highest rated matched reference spectrum with 97% of correlation (Montmorillonite\_STx-1\_NIC4bb\_RREF (USGS Spectral Library (Kokaly et al., 2017))).

Similar to petalite, spodumene has also presented montmorillonite as the main result of the correlation search on the USGS database. Due to the great similarities of these two Li minerals spectra, with the same reflectance evolution and absorption peaks, as studied before, these identical results were already expected. However, it is possible to notice that for spodumene the correlation rating is slightly higher, being the three first positions over 97.59%, which may be related with the bigger depths of the absorption peaks presented by spodumene, being closer to the depths presented by the reference spectra of montmorillonite (Figure 61). Marialite, a tectosilicate from the scapolite group, has presented a great correlation with the spodumene spectral signature.

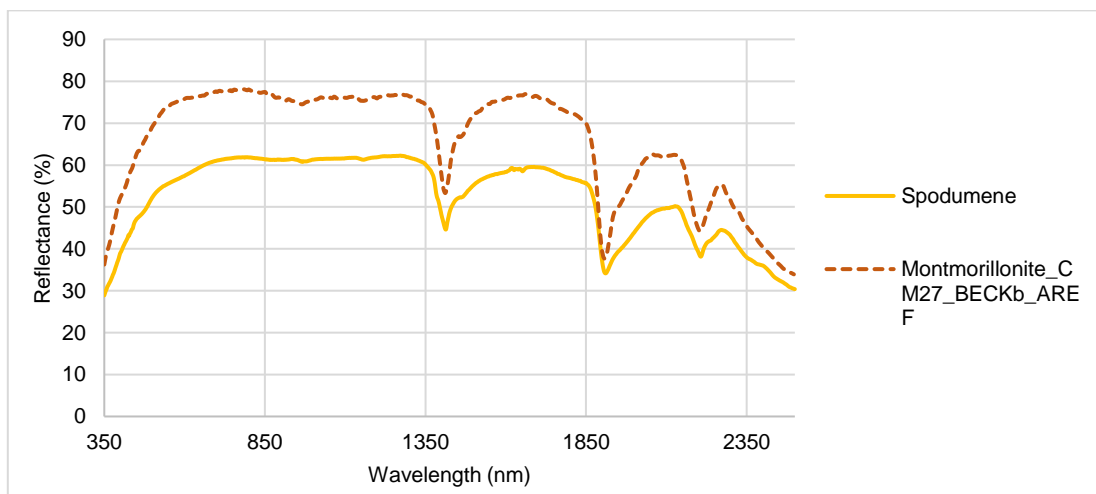


Figure 61 - Graphic comparison between spodumene spectral signature and the highest rated matched reference spectrum with 98.4% of correlation (Montmorillonite\_CM27\_BECKb\_AREF (USGS Spectral Library (Kokaly et al., 2017))).

As expected, due to the identical signature spectrum of SQUI to the spectra of spodumene and for a consequence of petalite, when searching against the reference spectra of USGS Spectral Library, the results are also very similar being matched with montmorillonite spectra (Figure 62), for the same reasons mentioned for spodumene and petalite. Within the top five results for SQUI, montmorillonite only appears three times, although, in the second position appears beidellite, which is also a clay mineral from the smectite group, as montmorillonite is. Although, beidellite on the last absolute absorption peak is slightly different, where this peak is presented at 2175 nm instead of 2207 nm, as in the SQUI signature. In opposition to the results of petalite and spodumene, the reference spectra matched for SQUI allows, not only to understand the correlation of the main absorption peaks, but also, of the ones of smaller expression, detected at 960 nm and 1150 nm, correspondent to the smaller expression peaks identified not only in the SQUI signature but also, in spodumene and petalite signatures. The correlation rating is identical to the one observed for the match between spodumene and the reference montmorillonite spectra, being over 97.21% for all top five results. Opal is also a presented result, however, is not possible to find any relation to the signature of SQUI or to the aplite-pegmatite veins, where the samples were taken.

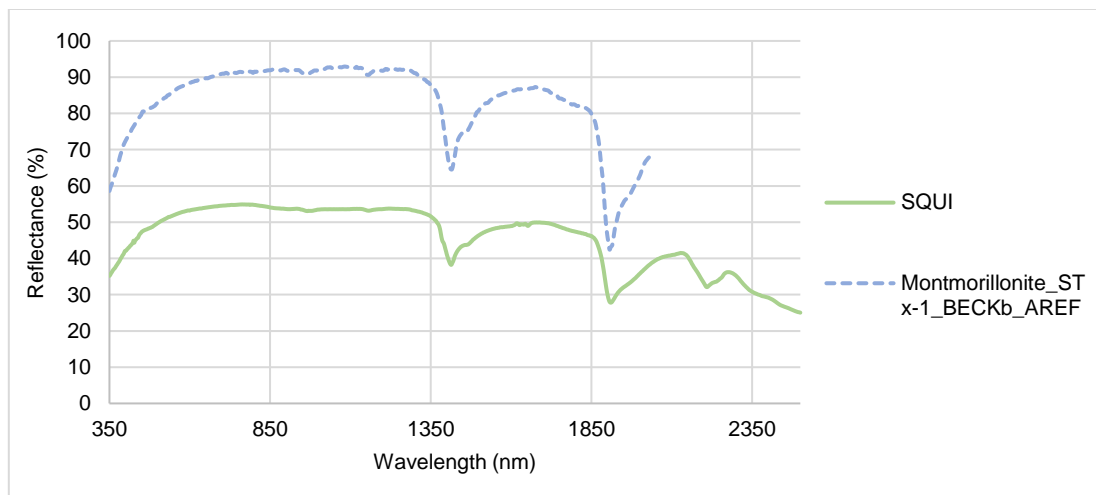


Figure 62 - Graphic comparison between SQUI spectral signature and the highest rated matched reference spectrum with 98.9% of correlation (Montmorillonite\_STx-1\_BECKb\_AREF (USGS Spectral Library (Kokaly et al., 2017))).

The search against the reference spectra of USGS Spectral Library of the spectral signature of lepidolite brings various results presenting endellite, halloysite, dickite, and illite, at a correlation rating from 95.84% to 96.57%. However, analyzing the results they are not much different from the previously obtained for the other Li minerals.

Endellite (Figure 63) is the hydrated form of halloysite and together with dickite and illite, they are all clay minerals and aluminosilicates, like montmorillonite that showed up in the previous results. The presence of illite in the results is justified by the fact that this is an aluminosilicate from the mica group, as lepidolite, and so they present similarities that justify the identical features observed in the spectra, as the diagnostic features of white mica, already mentioned.

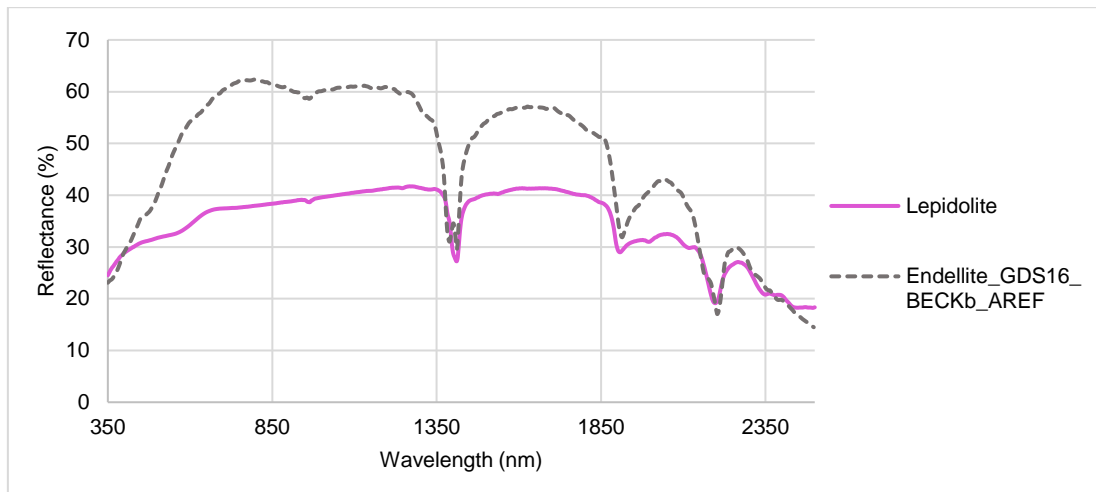


Figure 63 - Graphic comparison between lepidolite spectral signature and the highest rated matched reference spectrum with 96.6% of correlation (Endellite\_GDS16\_BECKb\_AREF (USGS Spectral Library (Kokaly et al., 2017))).

Montebrasite spectral signature when searched against the USGS database, presents results of low correlation, visible during the analyzes of the graphic representation. Pectolite is an inosilicate, which does not present visible absorption peaks, for that reason the evolution of the reflectance is the only thing that is a little similar to the montebrasite spectrum. Halloysite presents two absorption peaks that can be correlated to montebrasite peaks, however, the first peak of halloysite does not have an evident correlation, and besides montebrasite has a more complex spectrum, with various absorption peaks. Ammonio, a synthetic mineral, constituted by illite and smectite, which despite also having three absorption peaks similar to the halloysite ones, the more complex and wavy shape make be more correlated to the spectrum of montebrasite. USGS spectral library does not present reference spectra for montebrasite, what add to the fact that these montebrasite signature has a complex spectrum in the second part, might justify the lack of results with a higher correlation. Thus, is shown how much is important to have the most complete spectral library possible.

For the zinnwaldite spectral signature, all five results obtained are presented with high correlation rates, over 96.50%, with each referring to reference spectra of muscovite. The analysis reveals that the reference spectra of muscovite do not only have an identical reflectance evolution but also, can follow well the absorption peaks presented by the zinnwaldite signature (Figure 64). Muscovite, identically to zinnwaldite, is a phyllosilicate from the mica group, which might explain the intense correlation observable in the SWIR zone of the spectrum. These results are in concordance with the diagnostic features of white mica, defined previously for zinnwaldite. The same way as montebrasite, also for zinnwaldite USGS spectral library does not present reference spectra.

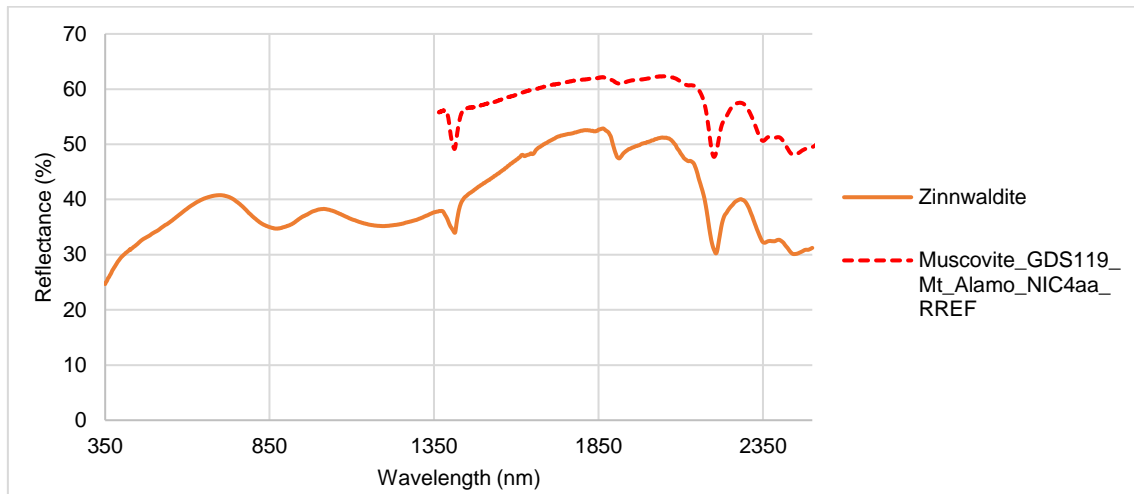


Figure 64 - Graphic comparison between zinnwaldite spectral signature and the highest rated matched reference spectrum with 97.7% of correlation (Muscovite\_GDS119\_Mt\_Alamo\_NIC4aa\_RREF (USGS Spectral Library (Kokaly et al., 2017))).

#### 4.4.2 ECOSTRESS Spectral Library

The analysis of the ECOSTRESS Spectral Library for the reference spectra with correlation to the petalite spectral signature, brought results not so expected, despite the great rate correlation, over 98.52% when compared with the results from USGS Spectral Library. The presence of scheelite, a calcium tungstate, and hemimorphite, a sorosilicate, does not present a direct relationship with petalite, either as an association mineral or as an alteration mineral, even the chemical composition of these minerals are quite divergent from the composition of petalite. However, the presence in the results of montmorillonite (Figure 65), as in USGS, may indicate some evidence of alteration in petalite, with this showing spectral features of alteration minerals.

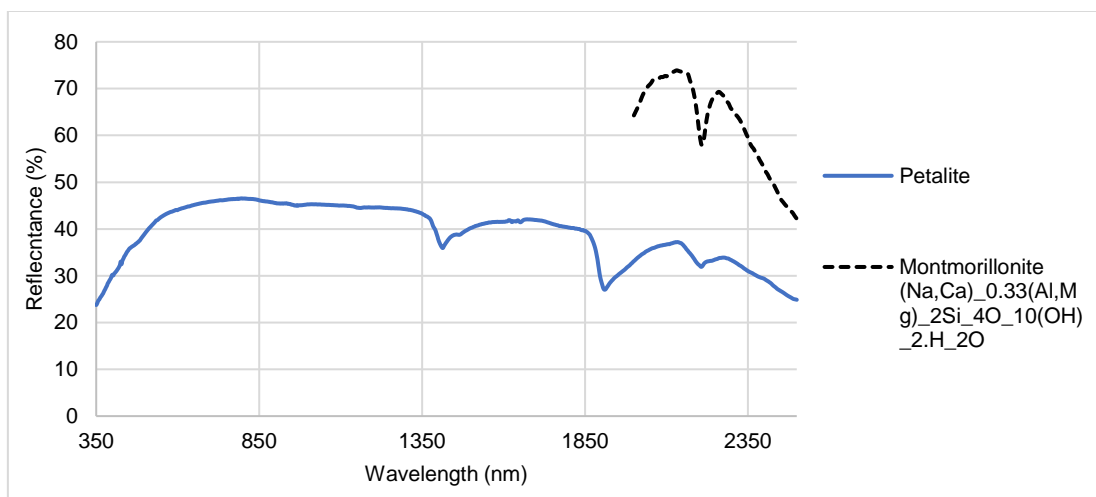


Figure 65 - Graphic comparison between petalite spectral signature and the reference spectrum of montmorillonite matched with 98.9% of correlation rate (ECOSTRESS Spectral Library (Baldrige et al, 2009)).

For the spodumene signature, the correlation rate is present over 97.91%, being scheelite the least correlated, having no direct relation with spodumene, as did not have with petalite. The high correlation with the reference spectra of montmorillonite is relatable with the results from the USGS database (Figure 66), showing similarities between the spectral features of this mineral to the spodumene signature spectrum. The presence of the mineral association of illite and smectite might demonstrate that not only the features of the smectite group is present, through montmorillonite, but also features of illite. However, with these results is possible to understand that even with the presence of illite, the montmorillonite features are dominant.

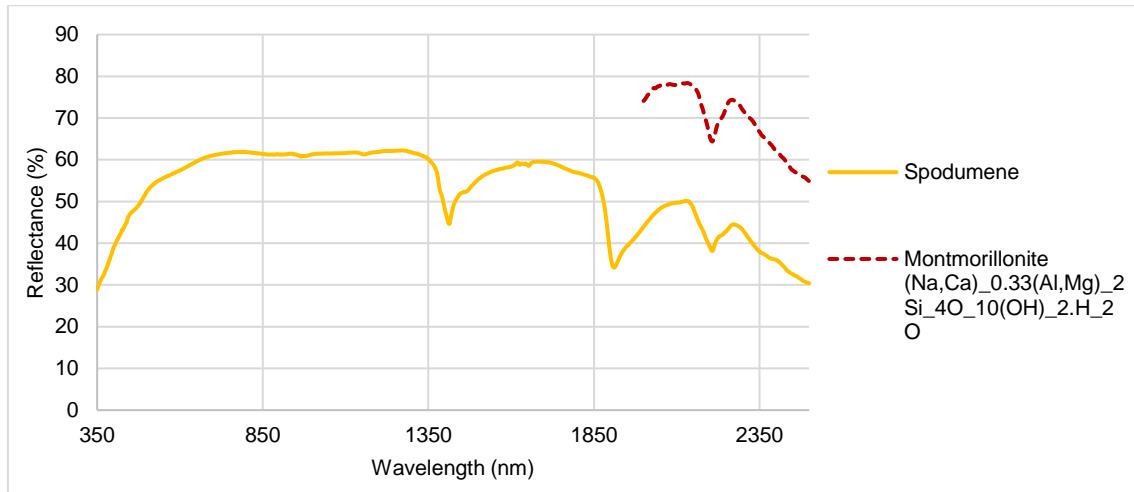


Figure 66 - Graphic comparison between spodumene spectral signature and the reference spectrum of montmorillonite matched with 99.2% of correlation rate (ECOSTRESS Spectral Library (Baldrige et al, 2009)).

Considering spodumene, for SQUI signature, the reference spectra of the mineral association of illite and smectite and the montmorillonite dominate the top five results, with a correlation rate of over 98.64%. These identical results show, once more, the equality of the spodumene and SQUI spectral signatures.

The search against the reference spectra of ECOSTRESS Spectral Library of the spectral signature of lepidolite has revealed a high correlation rate, being all the five over 98.70%, although these reference spectra are only overlapping lepidolite signature in the last 500 nm of the wavelength, therefore from 2000 nm to 2500 nm. According to the algorithm used, muscovite, is the best match (Figure 67), which might be related to the intense similarity on the depths of the absorption peaks, and probably for the same reasons, microcline, a potassic feldspar, produces also results of great correlation. The last two results are reference spectra of lepidolite, which is understandable the presence of the absorption peaks mentioned for lepidolite signature, within this range of wavelength, with similarities on the evolution of these peaks. However, the depths presented by the reference spectra are very different, more accentuated, which may be the reason why this spectrum does not have the best correlation. As the minerals of lepidolite measured are of small dimension, is possible that other minerals to interfere with the measurement, so the presence of microcline, in these results, maybe justified, once potassic feldspar is one of the main components of the aplite-pegmatite veins where lepidolite can be found, as was seen previously. For this reason, the low depths of the absorption peaks of microcline at the same wavelengths of lepidolite peaks might be reducing the total depth of the peaks on lepidolite signature, resulting in absorption

peaks with smaller expression than the ones from the lepidolite reference spectra. Also, the presence of muscovite can justify this, once is possible to observe the presence of small muscovite minerals mixed with the minerals of lepidolite, in the sample tested.

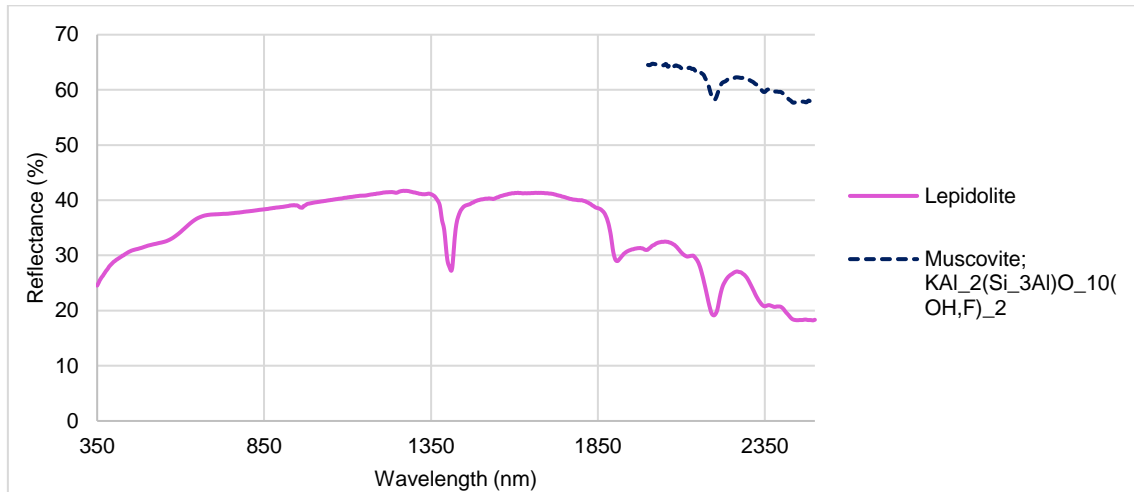


Figure 67 - Graphic comparison between lepidolite spectral signature and the highest rated reference spectrum, muscovite, matched with 99.1% of correlation rate (ECOSTRESS Spectral Library (Baldrige et al, 2009)).

In opposition of what happened with the results of USGS, when searching against ECOSTRESS, montebrasite presents more linear results, simply by the presence of amblygonite reference spectra in the ECOSTRESS database, a mineral that is not present in the USGS database, the reason why it was so difficult to find a good correlation in this library. When analyzing the graphic representation of the results of montebrasite, it is easily noticeable that all the five reference spectra of amblygonite matched, are accurate with the spectral signature of montebrasite (Figure 68), where the reflectance follows the same evolution, and the absorption zones and peaks are the same. Amblygonite is a phosphate which together with montebrasite forms an F-OH series (Kings and Foord, 1994), being the fluorine analogue of montebrasite. Because these two minerals constitute a series and have little differences, it is perfectly normal these obtained results with identical spectra.

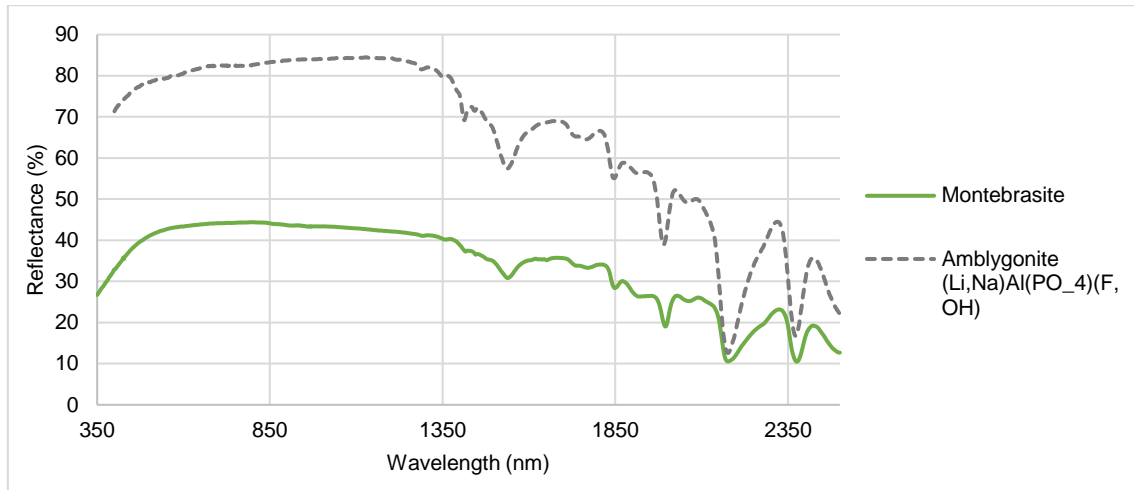


Figure 68 - Graphic comparison between montebbrasite spectral signature and the highest rated reference spectrum of amblygonite, matched with 98.8% of correlation rate (ECOSTRESS Spectral Library (Baldrige et al, 2009)).

For zinnwaldite, the obtained results when searched the spectral signature against the ECOSTRESS reference mineral spectra database, are very identical to the ones from the USGS database, where the reference spectra of muscovite dominate the top five results, however, in ECOSTRESS there is a result for microcline, a potassic feldspar. The correlation rate is 96.77%, being a little lower than the other studied minerals. The correlation with muscovite (Figure 69) happens for the reasons already explained in the description of the results of zinnwaldite from the USGS database, being the correlation with microcline also already explained before, for other studied minerals, when the appearance of a potassic feldspar in the results. As potassic feldspar is one of the main constituents of aplite-pegmatite veins, and because the minerals of zinnwaldite are very small, is possible that microcline interferes with the measurements resulting in an overall spectrum with some spectral features of this mineral.

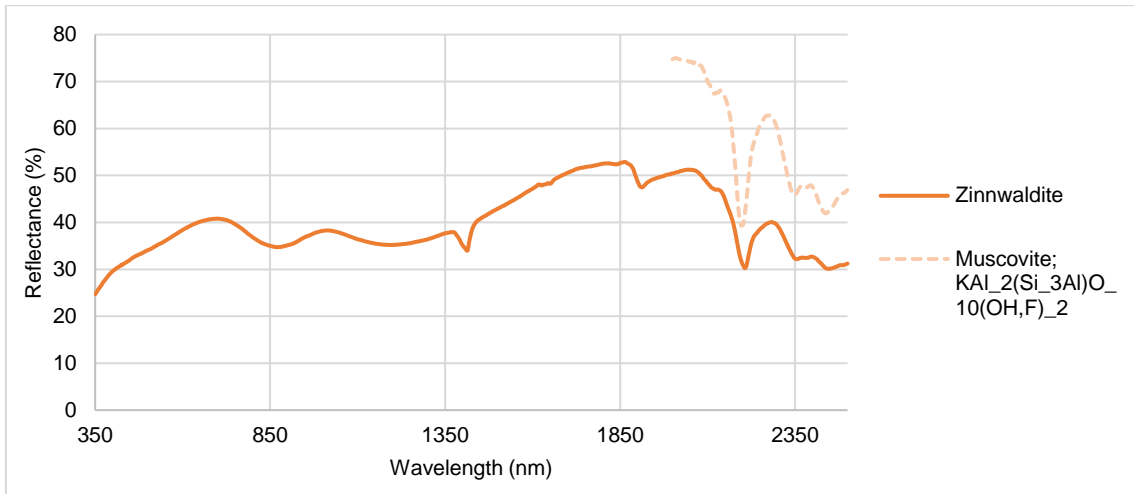


Figure 69 - Graphic comparison between zinnwaldite spectral signature and the highest rated reference spectrum of muscovite, matched with 98.9% of correlation rate (ECOSTRESS Spectral Library (Baldrige et al, 2009)).

#### 4.4.3 Discussion

As mentioned, petalite, spodumene, and for consequence SQUI spectral signatures, have diagnostic features of the smectite group, where due to the high absorption verified in the free molecular water, around ~1910 nm, it is possible to identify montmorillonite as the dominant mineral from this group (Clark et al., 1990; Hunt and Ashley, 1979). The constant presence of montmorillonite, in the results, when searching against these free-public access spectral libraries, is a justification for what has been said. The secondary absorption features of Al-OH verified for spodumene and SQUI spectral signatures justify also the illite/smectite mineral association responses obtained through the ECOSTRESS database.

For the same reasons of petalite and spodumene, the clay minerals are also present in the results of lepidolite, when searched against the USGS database. Although, it is noticeable that none of them is montmorillonite, which can be explained by the deepness of the absorption peaks, where a deep free molecular water feature is capable of identifying montmorillonite. However, in lepidolite, the free molecular water feature is the one of lower expression, which with the high deepness of the Al-OH feature and the associated Al-OH secondary features is diagnostic for white mica (Hunt and Salisbury, 1970; Scott and Yang, 1997). This presence of white mica characteristics justifies the obstinance of muscovite, illite, and lepidolite in the results, all minerals from the mica group.

For montebrasite, in the USGS database, the results have also pointed towards clay minerals, as halloysite, as probably a response to similar features of the ones presented by this type of minerals. On the other hand, ECOSTRESS results showed a high correlation with amblygonite, a mineral from the same series of montebrasite. Zinnwaldite due to the white mica features presented, produces identical results in both spectral libraries with muscovite, also a mica as zinnwaldite.

#### 4.4.4 CPRM Spectral Library

Contrary to the method utilized for comparison with the previous spectral libraries mentioned, in CPRM Spectral Library, the Li minerals spectral signatures were visually compared with the correspondent spectra of the CPRM spectral library.

Petalite and spodumene spectral reference from the CPRM database presents the same diagnostic features of clay minerals of the Fregeneda-Almendra samples. Comparing the spectra of spodumene is noticeable that the signature from CPRM presents iron absorption features, in the first half of the spectrum (400 nm to ~1350 nm), which cannot be identified in the spodumene spectrum from Fregeneda-Almendra. Furthermore, the absorption peaks of Fregeneda-Almendra spodumene are much more accentuated, presenting also, two features at ~2350 and ~2440 nm, where the first is possible to detect in these reference spectra, being similar, however, the second is not in the reference spectra. As the samples of CPRM used for the obtention of the petalite signature were samples with alteration evidence, the results demonstrate different signatures possible, being influenced by several alteration minerals. However, one of these (LB-R-024-B\_LIT.618 (Costa et al., 2016)) has an identical reflectance evolution to the presented by petalite spectral signature from Fregeneda-Almendra, although, the ~1410 nm feature in CPRM petalite seems to be slightly deeper.

The spectral signature obtained for lepidolite when compared to the CPRM lepidolite (LB-R-003-F\_LIT.138 (Costa et al., 2016)), demonstrates an identical reflectance evolution, presenting the same diagnostic features of white mica (Hunt and Salisbury, 1970; Scott and Yang, 1997). Also, in both, is possible to understand two absorption features, at around ~550 and ~950 nm, that might be connected to the presence of iron. The only particular difference noticeable is the H<sub>2</sub>O feature, which seems to be more accentuated in this reference spectrum of CPRM.

The comparison of zinnwaldite spectra demonstrates the presence of the diagnostic features of white mica, where the reflectance evolution is slightly different due to the intense absorption affecting the spectral signature of zinnwaldite obtained in this study, between ~700 nm and ~1800 nm. Comparing the montebrasite spectrum from this library to the signature obtained is practically impossible to find any differences, since this two show a very high correlation, presenting identical absorption peaks, with similar depths.



## 5. Conclusions

In this study, it was possible to analyze and characterize the spectral signatures of the Li minerals present at the Fregeneda-Almendra aplite-pegmatite field, through laboratory spectral measurements. Petalite and spodumene presented very identical spectral signatures, where the interpretation of the results showed that both minerals presented absorption features diagnostic of clay minerals from the smectite group, being characteristically montmorillonite due to the great peak deepness found on the free molecular water feature (~1910 nm). The presence of the Al-OH secondary features, especially in spodumene, demonstrate that are also present typical characteristics of illite. The comparison to the reference spectral libraries, corroborates these results and interpretations, showing the correlation to montmorillonite and to illite/smectite mineral association. Thus, the observed spectral signatures can be the combination of these two alteration minerals, where it is possible to understand that montmorillonite is dominant, presenting its typical features better marked in the signatures. Considering these results is noticeable how difficult it is to discriminate spectrally petalite and spodumene, since the presence of alteration influences its spectral signatures, erasing the characteristic features of these Li minerals. SQUI (spodumene + quartz) spectral signature presented the same spectral characteristics of spodumene, meaning that the presence of quartz has no influence in the signature. This can be explained due to the lack of characteristic absorption features of quartz, in this wavelength range.

The interpretation of the spectral signatures of lepidolite and zinnwaldite demonstrate the presence of diagnostic features of white mica, corroborated by the results of correlation with the spectral libraries, matching micas, such as muscovite, illite, and lepidolite. For the lepidolite signature, it was also possible to understand the presence of clay minerals diagnostic characteristics, but not from montmorillonite, since in this the free molecular water feature was the one with the lowest expression. Montebrasite showed a spectral signature very distinctive from the remaining, producing great results with high correlation rates when in comparison to the ECOSTRESS library, matching amblygonite, a mineral from the same series of montebrasite. In conclusion, the fact of these three minerals had preserved its main spectral features, without acquiring features of alteration minerals, allowed a better and easier spectrally discrimination, contrary to petalite and spodumene.

The Spectral signatures obtained for the T5 and T7 aplite-pegmatite veins showed the same clay minerals typical features, present in the signature of petalite and spodumene, being the indications of the presence of iron oxides the main differences between these aplite-pegmatite veins and these Li minerals.

The study of the various categories defined for CXG lithologies have demonstrated that the presence of an aplite-pegmatite vein nearby, does not influence in the final spectrum, since it was not found any particular difference between the CXG nearby a vein to the CXG without relation to this type of veins.

Identically to the Li minerals studied, both CXG and granite spectra produced the same clay minerals spectral characteristics, which is probably the reason why it was so difficult, in the previous studies, for the algorithms used to delimit the Li-bearing veins. With the present study, it was possible to define the presence of iron-related features, as the main differentiators from the Li minerals.

## 5.1 Further Work

As a result of the pandemic crisis caused by the new coronavirus (COVID-19), a few techniques, such as LIBS (Laser-induced breakdown spectroscopy) and X-ray fluorescence (XRF), initially planned for this study had to be canceled. Therefore, in further works, these techniques, along with chemical analyses should be employed.

The application of such techniques is important for a greater understanding of the reasons behind the observed spectral characteristics and features. Recognizing the correlations between the chemical composition of the minerals and the features described and searching for the chemical elements or chemical bonds responsible for the absorptions. Also, a deep knowledge of the alteration minerals related to these Li minerals and present in this study region is needed, since its spectral signatures seem to contribute or even substitute the original signature.



## 6. References

- Bachri, I.; Hakdaoui, M.; Raji, M.; Teodoro, A.C.; Benbouziane, A., 2019. Machine Learning Algorithms for Automatic Lithological Mapping Using Remote Sensing Data: A Case Study from Souk Arbaa Sahel, Sidi Ifni Inlier, Western Anti-Atlas, Morocco. *ISPRS Int. J. Geo-Inf.*, 8.
- Baldrige, A. M., S.J. Hook, C.I. Grove and G. Rivera, 2009. The ASTER Spectral Library Version 2.0. *Remote Sensing of Environment*, vol 113, pp. 711-715.
- Binotto, R. B., Saldanha, D. L., Dias, A. R. A., Perrotta, M., 2015. Identificação dos padrões espectrais da alteração hidrotermal da Mina Uruguai, Caçapava do Sul (RS), utilizando espectros de refletância experimental. *Pesquisas em Geociências*, 42, pp. 89-101.
- Cardoso-Fernandes, J., Lima A., and Teodoro A. C., 2018. Potential of Sentinel-2 data in the detection of lithium (Li)-bearing pegmatites: a study case. *Proc. SPIE 10790, Earth Resources and Environmental Remote Sensing/GIS Applications IX*, 107900T.
- Cardoso-Fernandes, J.; Teodoro, A.C.; Lima, A., 2019a. Remote sensing data in lithium (Li) exploration: A new approach for the detection of Li-bearing pegmatites. *Int. J. Appl. Earth Obs. Geoinf.*, 76, pp. 10–25.
- Cardoso-Fernandes, J., Teodoro, A., Lima, A., Roda-Robles, E., 2019b. Evaluating the performance of support vector machines (SVMs) and random forest (RF) in Li-pegmatite mapping: preliminary results, *Proc. SPIE 11156, Earth Resources and Environmental Remote Sensing/GIS Applications X*, 111560Q.
- Černý, P., 1994. Evolution of feldspars in granitic pegmatites. In: Parsons (Ed.), *Feldspars and their reactions*, NATO ASI series, Kluwer Academic Publishers, Holanda, série C, Vol. 421, pp. 501-540.
- Černý, P., Ferguson, R. B., 1972. The Tanco Pegmatite at Bernic Lake, Manitoba. *Petalite and Spodumene relations*. *Can. Mineral.*, 11, pp. 660-678.
- Černý, P., Meintzer, R. E., Anderson, A. J., 1985. Extreme fractionation in rare-element granitic pegmatites: selected examples of data and mechanisms. *Can. Mineral.*, 23, pp. 381-421.
- Černý, P.; Ercit, T.S., 2005. The classification of granitic pegmatites revisited. *Can. Mineral.* 43, pp. 2005–2026.

- Černý, P.; London, D.; Novak, M., 2012. Granitic pegmatites as reflections of their sources. *Elements*, 8, pp. 289–294.
- Chaminé, H., 2000. *Estratigrafia e Estrutura da Faixa Metamórfica de Espinho-Albergaria-a-Velha (Zona de Ossa-Morena): Implicações Geodinâmicas*. Departamento de Geologia, Faculdade de Ciências, Universidade do Porto. (Tese de Doutoramento).
- Clark, R. M., King T. V. V., Klejwa M., Swayze G. A., and Vergo N., 1990. High spectral resolution reflectance spectroscopy of minerals. *Journal of Geophysical Research: Solid Earth*, 95(B8).
- Clark, R. N., 1999. Spectroscopy of rocks and minerals and principles of spectroscopy: Chapter 1. Remote Sensing for the Earth Sciences: Manual of Remote Sensing. R. A. Ryerson, Ed., John Wiley & Sons, Inc.
- Costa, J.C.S., 1950. Notícia sobre uma carta geológica do Buçaco, de Nery Delgado. *Serviços Geológicos de Portugal*, Lisboa.
- Costa, M., Perrotta M., Melo T., Turra B., 2016. Avaliação do potencial do lítio no Brasil: área do Médio Rio Jequitinhonha, Nordeste de Minas Gerais. *Companhia de Pesquisa de Recursos Minerais – CPRM Serviço Geológico do Brasil*, pp. 99-113.
- Dallmeyer, R. & García, E., 1990. *Pre-Mesozoic Geology of Iberia*. Berlin, Springer-Verlag, 416 pp.
- Dias, G., Noronha, F., Ferreira, N., 2000. Variscan Plutonism in the Central Iberian Zone, Northern Portugal. *Eurogranites 2000, Field Meeting, Guide Book*. pp. 1–15.
- Dias, R., 2010. Evolução geodinâmica de Portugal no contexto do ciclo Varisco. VIII Congresso Nacional de Geologia. *GEOTIC – Sociedade Geológica de Portugal. e -Terra*. Volume 8–nº 3
- Dias, R., Ribeiro, A., 2013. O Varisco do sector norte de Portugal. In: Dias, R., Araújo, A., Terrinha, P., Kullberg, J.C., (Eds), *Geologia de Portugal*, vol. 1, Escolar Editora, 59 p.
- Dias, R., Ribeiro, A., Coke, C., Moreira, N., Romão, J. 2014. Arco Ibero-Americano: indentação versus auto-subducção. *Comunicações Geológicas*, v. 101, Especial I, 261-264p. Laboratório Nacional de Energia e Geologia.
- Díez Balda, M.A., Vegas, R., Lodeiro, G., 1990. Central iberian zone: structure. In: Dallmeyer, R.D., Martinez Garcia, E. (Eds.), *Pre-Mesozoic Geology of the Iberian Peninsula*. Springer Verlag, Berlim, pp. 172–188.

Dill, H.G., 2015. Pegmatites and aplites: Their genetic and applied ore geology. *Ore Geol. Rev.*, 69, pp. 417–561.

Farias, P., Gallastegui, G., Gonzalez Lodeiro, F., Marquinez, J., Martin Parra, L.M., Martinez Catalan, J.R., Pablo Maciá, J.G. De & Rodriguez Fernandez, L.R., 1987. Aportaciones al conocimiento de la litoestratigrafia y estructura de Galicia Central. In: IX Reunião de Geologia do Oeste Peninsular, Porto, 1985. *Mem. Mus. Labor. Miner. Geol. Fac. Ciênc. Univ. Porto*, 1: pp. 411-431.

Ferreira, N., Iglésias, M., Noronha, F., Pereira, E., Ribeiro, A. & Ribeiro, M.L., 1987. Granitóides da Zona Centro Ibérica e seu enquadramento geodinâmico. In: Bea, F. et al., (eds) *Geologia de los granitoides y rocas asociadas del Macizo hesperico*, Editorial Rueda, Madrid, pp. 37-51.

Frutuoso, R., 2015. Mapping hydrothermal gold mineralization using Landsat 8 data. A case of study in Chaves license, Portugal. Tese de Mestrado. Faculdade de Ciências da Universidade do Porto, Porto.

Gaffey, S.J., McFadden, L.A., Nash, D., Pieters, C.M., 1993. Ultraviolet, visible, and near-infrared reflectance spectroscopy: laboratory spectra of geologic materials. In: Pieters, C.M., Englert, P.A.J. (Eds.), *Remote Geochemical Analysis: Elemental and Mineralogical Composition*. Cambridge University Press, NY, USA, pp. 43–77.

García Garzón, J. e Locutura, J., 1981. Datación por el método Rb-Sr de los granitos de Lumbrales-Sobradillo y Villar de Ciervo-Puerto Seguro. *Bol. Geol. Min.* 92-1, pp. 68-72.

Gaspar, L., 1997. Contribuição para o estudo das mineralizações de volfrâmio (W), estanho (Sn) e lítio (Li) do sector Barca de Alva – Escalhão. Tese de Mestrado. Fac. Ciências, Univ. de Lisboa, Portugal.

Gemusse, U., Lima A., and Teodoro A., 2018. Pegmatite spectral behavior considering ASTER and Landsat 8 OLI data in Naipa and Muiane mines (Alto Ligonha, Mozambique). *Proc. SPIE 10790, Earth Resources and Environmental Remote Sensing/GIS Applications IX*, 107901L.

Gemusse, U., Lima A., and Teodoro A., 2019. Comparing different techniques of satellite imagery classification to mineral mapping pegmatite of Muiane and Naipa: Mozambique. *Proc. SPIE 11156, Earth Resources and Environmental Remote Sensing/GIS Applications X*, 111561E.

Google Earth Pro, (June 8<sup>th</sup> of 2020). available in: [https://www.google.com/intl/en\\_uk/earth/versions/](https://www.google.com/intl/en_uk/earth/versions/)

- Gourvenec, R., Piçarra, J. M., Plusquellec, Y., Pereira, Z., Oliveira, J. T., Robardet, M., 2010. Lower Devonian faunas and palynomorphs from the Dornes Syncline (Central Iberian Zone, Portugal): stratigraphical and paleogeographical implications. *Carnets de Géologie*, A09.
- Greim, P., Solomon, A. A., Breyer, C., 2020. Assessment of lithium criticality in the global energy transition and addressing policy gaps in transportation. *Nature Communications* 11, 4570.
- Hunt, G. R., 1977. Spectral signatures of particulate minerals in the visible and near-infrared. *Geophysics* 42, 501–513.
- Hunt, G. R., and Ashley R. P., 1979. Spectra of altered rocks in the visible and near infrared. *Economic Geology*, 74(7), pp. 1613-1629.
- Hunt, G. R., and Salisbury, J.W., 1970. Visible and near-infrared spectra of minerals and rocks: I Silicate minerals. *Modern Geology*. 1, pp. 283–300.
- Julivert, M., 1972. Mapa tectónico de la Península Ibérica y Baleares Escala 1:1.000.000. Ministerio de Industria y Energía, Servicio de Publicaciones, Madrid p 1 mapa.
- Julivert, M., Fontboté, J.M., Ribeiro, A., & Conde, L.E.N., 1974. Mapa Tectónico de la Península Ibérica y Baleares, Escala 1:1000.000. Memoria Explicativa. Instituto Geologico y Minero de España, Madrid.
- Kesler, S.E., Gruber, P.W., Medina, P.A., Keoleian, G.A., Everson, M.P., & Wallington, T.J., 2012. Global lithium resources: Relative importance of pegmatite, brine and other deposits. *Ore Geology Reviews* 48, 55–69.
- King, V., Foord, E., 1994. The Amblygonite/Montebbrasite Controversy. *Mineralogy of Maine: v1: p. 15-17, pp. 240-244.*
- Kokaly, R.F., Clark, R.N., Swayze, G.A., Livo, K.E., Hoefen, T.M., Pearson, N.C., Wise, R.A., Benzel, W.M., Lowers, H.A., Driscoll, R.L., and Klein, A.J., 2017. USGS Spectral Library Version 7 Data: U.S. Geological Survey data release.
- London, D., 2005. Granitic pegmatites: An assessment of current concepts and directions for the future. *Lithos*, 80, pp. 281–303.
- London, D., 2008. Pegmatites. *Can. Mineral*, 10.
- López-Plaza, M, and Carnicero, M.A., 1988. El plutonismo Hercínico de la penillanura salmantino-zamorana (centro-oeste de España): Visión de conjunto en el contexto geológico

regional. In *Geologia de los granitoides y rocas asociadas del macizo Hespérico*. Rueda, Madrid, 53-68.

- Lotze, F., 1945. Zur gliederung der Varisziden der Iberischen Meseta. s.n. Berlin. pp. 15.
- Marques, M., Noronha, F., Flores, D. & Rodrigues, B., 2000. *Geologia da faixa costeira Lavadores-Porto*. In: Livro-guia da excursão geológica do XX Curso de Atualização de Professores de Geociências, Departamento de Geologia, Faculdade de Ciências, Universidade do Porto/Associação Portuguesa de Geólogos, Porto.
- Martínez Catalán, J.R., Aller, J., Alonso, J. L., Bastida, F., 2009. Chapter 1: The Iberian Variscan Orogen. *Instituto Geológico y Minero de España*, pp. 13-30.
- Martínez Catalán, J.R., Fernández-Suárez, J., Jenner, G.A., Belousova, E. and Díez Montes, A. 2004. Provenance constraints from detrital zircon U-Pb ages in the NW Iberian Massif: implications for Paleozoic plate configuration and Variscan evolution. *Journal of the Geological Society, London*, 161, pp. 461-473.
- Mendes, D., Perrotta, M.M., Costa, M.A.C., Paes, V.J.C., 2017. Mapeamento espectral para identificação de assinaturas espectrais de minerais de lítio em imagens ASTER (NE/MG). *Anais Do XVIII Simpósio Brasileiro De Sensoriamento Remoto* 5273–5280.
- Menges, F., 2019. Functions of the Identify ribbon. [https://www.effemm2.de/spectragryph/about\\_help\\_manual\\_identify.html](https://www.effemm2.de/spectragryph/about_help_manual_identify.html) (15 July 2020).
- Menges, F., 2020. "Spectragryph - optical spectroscopy software, Version 1.2.14", <http://www.effemm2.de/spectragryph>
- Moradi, M., Basiri, S., Kananian, A., Kabiri, K., 2014. Fuzzy logic modeling for hydrothermal gold mineralization mapping using geochemical, geological, ASTER imageries and other geo-data, a case study in Central Alborz, Iran. *Earth Sci. Inform.* 8 (1), pp. 197–205.
- Müller, A.; Romer, R.L.; Pedersen, R.-B., 2017. The Sveconorwegian Pegmatite Province—Thousands of Pegmatites Without Parental Granites. *Can. Mineral*, 55, pp. 283–315.
- Naleto, J. L. C., Perrotta M. M., Costa F. G. and Souza Filho C. R., 2019. Point and imaging spectroscopy investigations on the Pedra Branca orogenic gold deposit, Troia Massif, Northeast Brazil: Implications for mineral exploration in amphibolite metamorphic-grade terrains. *Ore Geology Reviews*, 107, pp. 283-309.
- Neiva, A.M.R., 1995. Distribution of trace elements in feldspars of granitic aplites and pegmatites from Alijó-Sanfins, northern Portugal. *Mineral. Mag.*, 59, pp. 35-45.

- Noronha, F., Ramos, J.M.F., Rebelo, J.A., Ribeiro, A., Ribeiro, M.L., 1979. Essai de corrélation des phases de déformation hercynienne dans le Nord-Ouest Péninsulaire. *Bol. Soc. Geol. Portugal* 21 (2-3), pp. 227–237.
- Noronha, F., Ribeiro, M.A., Almeida, A., Doria, A., Guedes, A., Lima, A., Martins, H. C., Sant’Ovaia, H., Nogueira, P., Martins, T., Ramos, R., Vieira, R. 2006. Jazigos filonianos hidrotermais e aplitopegmatíticos especialmente associados a granitos (norte de Portugal). In: *Geologia de Portugal no contexto da Iberia* (Dias, R. Araujo, A., Terrinha, P. e Kulberg, Editores). Univ.Evora, Evora, pp. 123-138.
- Oliveira, J. M. S., 1982. Orientação geoquímica com vista à escolha da metodologia a seguir na prospeção de mineralizações de estanho e volfrâmio. *Comum. Serv. Geol. Portugal*. 68(2), pp. 171-178.
- Pereira, E., Ribeiro, A., Meireles, C., 1993. Cisalhamentos Hercínicos e controlo das mineralizações de Sn-W, Au e U na Zona Centro Ibérica, em Portugal. *Cuaderno Lab. Xeolóxico de Laxe. Coruña*. Vol. 18, pp. 89-119.
- Perrotta, M.M., Souza Filho, C.R., Leite, C.A.S., 2005. Mapeamento Espetral De Intrusões Pegmatíticas Relacionadas a Mineralizações De Lítio, Gemas E Minerais Industriais Na Região Do Vale Do Jequitinhonha (MG) a Partir De Imagens ASTER. *Anais Do XII Simpósio Brasileiro De Sensoriamento Remoto*.
- Quesada, C., 1992. Evolución Tectónica del Macizo Ibérico (una historia de crecimiento por acreencia sucesiva de terrenos durante el Proterozoico superior y el Paleozoico). In *Gutiérrez-Marco, J. C., Saavedra, J. & Rábano, I. (Eds.). Paleozoico Inferior de Ibero-América*. Universidad de Extremadura, pp. 174-190.
- Ray, T. W., 1994. A FAQ on Vegetation in Remote Sensing. Accessed in 25<sup>th</sup> of May 2020.
- Ribeiro, A., Antunes, M. T., Ferreira, M. P., Rocha, R. B., Soares, A. F., Zbyszewski, G., Almeida, F. M., Carvalho, D., Monteiro, J. H., 1979. Introduction à la géologie générale du Portugal, *Serviços Geológicos de Portugal, Lisboa*. (XXVI Congr. Internat. Géol., Paris, 1980).
- Ribeiro, M.L., Silva, A.Fd., 1994. Notícia Explicativa da folha 15-B Freixo de Espada à Cinta. Instituto Geológico e Mineiro. Departamento de Geologia, Lisboa, pp. 48.
- Roda, E., 1993. Distribución, Características y Petrogenesis de las Pegmatitas de La Fregeneda (Salamanca). Tese de Doctoramento. UPV, Bilbao.

- Roda, E., Pesquera, A., Velasco, F., Fontan, F., 1999. The granitic pegmatites of the Fregeneda area (Salamanca, Spain): characteristics and petrogenesis. *Mineral. Mag.* 63 (4), pp. 535–558.
- Rodríguez Alonso, M.D., Díez Balda, M.A., Perejón, A., Pieren, A., Liñán, E., López Díaz, F., Moreno, F., Gámez Vintaned, J.A., González Lodeiro, F., Martínez Poyatos, D., Vegas, R., 2004. Domínio del Complejo Esquisto-Grauváquico: Estratigrafía. La secuencia litoestratigráfica del Neoproterozóico-Câmbrico Inferior. In: Vera, J.A. (Ed.), *Geología de España*. Geol. España/Inst. Geol. Min. España (SGE-IGME), Madrid, pp. 78–81.
- Romão, J., Coke, C., Dias, R., Ribeiro, A., 2005. Transient inversion during the opening stage of the Wilson cycle «Sardic phase» in the Iberian Variscides –Stratigraphic and tectonic record. *Geodinamica Acta*. V.18:2, pp. 115–129.
- Romer, R.L.; Kroner, U., 2016. Phanerozoic tin and tungsten mineralization—Tectonic controls on the distribution of enriched protoliths and heat sources for crustal melting. *Gondwana Res.*, 31, pp. 60–95.
- Sabins, F. F., 1999. Remote sensing for mineral exploration. *Ore Geology Reviews* 14, 157–183.
- Sabins, F.F., 1997. *Remote Sensing—Principles and Interpretation*. 3rd Edition, W.H. Freeman, New York City, New York.
- Santos, D., Teodoro, A., Lima, A., Cardoso-Fernandes, J., 2019. Remote sensing techniques to detect areas with potential for lithium exploration in Minas Gerais, Brazil. *Proc. SPIE* 11156, *Earth Resources and Environmental Remote Sensing/GIS Applications X*, 111561F.
- Scott, K.M., Yang, K., 1997. Spectral reflectance studies of white micas. *Exploration and Mining Report 439R*. CSIRO Division of Exploration and Mining, pp. 41.
- Selway, J.B.; Breaks, F.W.; Tindle, A.G., 2005. A Review of Rare-Element (Li–Cs–Ta) Pegmatite Exploration Techniques for the Superior Province, Canada, and Large Worldwide Tantalum Deposits. *Explor. Min. Geol.*, 14, pp. 1–30.
- Shearer, C. K., Papike, J. J., Laul, J. C., 1985. Chemistry of potassium feldspars from three zoned pegmatites, Black Hills, South Dakota: implications concerning pegmatite evolution. *Geochim. Cosmochim. Acta.*, 49, pp. 663-673.
- Silva, A., 2005. A Litoestratigrafia e Estrutura do Supergrupo Dúrico – Beirão (Complexo Xisto-Grauváquico), em Portugal, e a sua correlação com as correspondentes sucessões em Espanha. *Instituto Nacional de Engenharia, Tecnologias e Inovação*, pp. 2-26.

- Silva, A., 2014. Mineralogia, petrologia e geoquímica de granitos e filões aplito-pegmatíticos da região de Guarda – Sabugal. Tese de doutoramento. Universidade de Trás-os-Montes e Alto Douro. Vila Real.
- Silva, A., Ribeiro, A., 1985. Thrust Tectonics of Sardinian Age in the Alto Douro Region (Northeastern Portugal). *Comun. Serv. Geol. Portugal*. 71(2), pp. 151-157.
- Silva, A., Ribeiro, M.L., 1991. Notícia Explicativa da folha 15-B – Freixo de Espada à Cinta. *Serviços Geológicos de Portugal, Lisboa*, pp. 52.
- Silva, A., Ribeiro, M.L., 1994. Notícia Explicativa da folha 15-A Vila Nova de Foz Côa – da carta Geológica de Portugal na escala 1/50.000. Instituto Geológico e Mineiro. pp. 48.
- Sousa, M. B., 1982. Litostratigrafia e estrutura do Complexo-Xisto-Grauváquico – Grupo do Douro (NE Portugal). Tese de Doutoramento. Univ. Coimbra, Coimbra. pp. 222.
- Sousa, M. B., Sequeira, A.J.D. 1989. Notícia explicativa da Folha 10-D – Alijó – na escala de 1/50.000. 1a. ed. *Serviços Geológicos de Portugal, Lisboa*.
- Sousa, M.B. 1983. Litoestratigrafia do CXG - Grupo do Douro (NE de Portugal). *Memórias e Notícias. Universidade de Coimbra*. 95, pp. 3-63.
- Sousa, M.B., 1981. Complexo Xisto-Grauváquico do Douro: - Os xistos cloríticos com magnetite e seu valor estratigráfico. *Com. dos Serv. Geol. de Portugal*. 67(1), pp. 53-55.
- Steiner, B.M., 2019. Tools and workflows for grassroots Li-Cs-Ta (LCT) pegmatite exploration. *Minerals*, 9 (8), art. no. 499.
- Sun, Y., Seccombe P. K., and Yang K., 2001. Application of short-wave infrared spectroscopy to define alteration zones associated with the Elura zinc–lead–silver deposit, NSW, Australia. *Journal of Geochemical Exploration*, 73(1), pp. 11-26.
- Teixeira, C., 1955. Notas sobre geologia de Portugal o complexo xisto-grauváquico anteordoviciano. Lisboa. pp. 48.
- Therien, C., "Welcome to the PySptools Documentation" (22 July 2020) <https://pysptools.sourceforge.io>
- Vieira, R. and Lima, A., 2005a. The Rare Element (Li-Rich) Pegmatite-Aplite Veins of the Almendra – Souto Region. (V. N. de Foz-Côa and Penedono - NE Portugal). Abstracts of the International Meeting, Crystallization Processes in Granitic Pegmatites: Petrologic, mineralogic and geochemical aspects, Elba, Itália, pp. 48-49.

Vieira, R. and Lima, A., 2005b. Relação Geoquímica entre os Aplitopegmatitos da Região de Almendra – Souto e os Granitos Envolventes (NE de Portugal). Abstract Book of the XIV Semana de Geoquímica & VIII Congresso de Geoquímica dos Países de Língua Portuguesa. Universidade de Aveiro, I, pp. 189-193.

Vieira, R., 2010. Aplitopegmatitos com elementos raros da região entre Almendra (V.N. de Foz Côa) e Barca d'Alva (Figueira de Castelo Rodrigo). Campo aplitopegmatítico da Fregeneda- Almendra. Tese de Doutoramento. Faculdade de Ciências da Universidade do Porto, Porto.

Zagorsky, V.Y.; Vladimirov, A.G.; Makagon, V.M.; Kuznetsova, L.G.; Smirnov, S.Z.; D'yachkov, B.A.; Annikova, I.Y.; Shokalsky, S.P.; Uvarov, A.N., 2014. Large fields of spodumene pegmatites in the settings of rifting and postcollisional shear–pull-apart dislocations of continental lithosphere. *Russ. Geol. Geophys.*, 55, pp. 237–251.